Theoretical Modeling of Interactions Between Electrolytes and Surfaces

Thesis by
Dorian Bruch

In Partial Fulfillment of the Requirements for the
Degree of
Doctor of Philosophy in Chemical Engineering

CALIFORNIA INSTITUTE OF TECHNOLOGY
Pasadena, California

2025
Defended August 12, 2024

Dorian Bruch
ORCID: 0000-0002-3983-4841

ACKNOWLEDGEMENTS

I am grateful for the help and support I received from my friends, family, and colleagues during my arduous but rewarding academic journey. I am thankful to my PhD advisor Zhen-Gang Wang for guiding me throughout the years and for fostering my analytical abilities. All of the Wang group members helped me in some way—from countless home gatherings, to nights out in old-town Pasadena, to several restaurants tried, the members of the Wang group made my time at Caltech truly memorable. Specifically, I would like to thank Alexandros Tsamopoulos and Sriteja Mantha for our intriguing scientific and non-scientific discussions, Sam Varner and Benjamin Ye for our game time, and Chris Balzer and Alejandro Gallegos for help with my research.

I am privileged to have had support from my undergraduate friends Ryan, Daniel, and Josue during my entire PhD. I am grateful for my two cats, Sampson and Twinkles, whose endless love and attention kept me lively during hard times. I am indebted to my father and step mother who saved me from a young age, allowing me to pursue education to my fullest ambition, as well as my entire extended family for their unwavering support. I am thankful to my partner's mother and father for treating me as one of their own, as well as her entire family for all of their support during my graduate education. To my wonderful partner, Elizabeth, I can never repay you for your patience and sacrifices made during my PhD. You always believed in me even when I did not believe in myself, and for that I am eternally grateful.

To my late mother, thank you for making me curious about the world as well as teaching me to perform my best, not to impress others but to impress myself. These characteristics have taken me to where I am today. I wish you could have seen me finish my PhD. Lastly, to my little siblings from my late mother, I hope that I have shown you that you can make something of yourself no matter your circumstances in life.

ABSTRACT

Electrolytes are ubiquitous in science and engineering and are of active interest, owing to their applications biology, energy storage, colloidal suspensions, and even climate. Near a surface, electrolyte solutions exhibit a plethora of rich thermodynamic and structural phenomena, owing to the interplay of long-ranged electrostatics and nonelectrostatic interactions between ionic species, solvent, and the surface. In this thesis, we present a pedagogical formulation for the thermodynamics of electrolyte solutions near charged surfaces, followed by an examination of interactions and structure of different types of electrolytes near surfaces. Specifically, we investigate the difference between constant surface charge and constant surface potential boundaries in electrolyte solutions, the capacitance applications, double-layer structure, and screening behavior of a zwitterionic polymers, as well as the effect of image charge on structure, capacitance, and forces in simple electrolytes near metal, dielectric, and dielectrically-saturated metal surfaces. We conclude with a Gaussian-fluctuation model for ions with soft-core excluded volume interactions.

PUBLISHED CONTENT AND CONTRIBUTIONS

(1) Zhou, T.; Bruch, D.; Wang, Z.-G. Image charge effects under metal and dielectric boundary conditions, en, arXiv:2405.13261 [cond-mat], 2024,
T.Z. participated in the conception of the project, wrote the original code, gathered and analyzed data, and wrote the original manuscript for the pure metal/dielectric boundary analysis before D.B. joined the project. D.B. conducted calculations, analyzed data, and participated in the writing of the manuscript concerning the dielectrically-saturated metal surface case, as well as further calculations and revisions for the entire paper.

(2) Bruch, D.; Balzer, C.; Wang, Z.-G. *J. Chem. Phys.* **2022**, *156*, 174704, DOI: 10.1063/5.0089260,
D.B. participated in the conception of the project, conducted calculations, analyzed data, and participated in the writing of the manuscript.

CONTENTS

LIST OF FIGURES

Chapter 1

INTRODUCTION

This chapter gives a high-level description on electrolytes, their applications, and open problems in understanding their interactions with surfaces. Later chapters will delve into their thermodynamics, capacitance applications of zwitterionic electrolytes, image-charge correlation effects in simple electrolytes, and a fluctuating model for ions with soft-core excluded volume.

This chapter includes content from our previously published article:

(1) Bruch, D.; Balzer, C.; Wang, Z.-G. *J. Chem. Phys.* **2022**, *156*, 174704, DOI: 10.1063/5.0089260,

1.1 Preliminaries

An electrolyte is a medium, such as water, containing charged species that can be conducted by an electric field. These charges interact with the solvent, other ions, and surfaces through long-ranged electrostatic forces such as charge-charge and charge-dipole interactions, as well as nonelectrostatic contributions such as excluded volume effects. Some common types of charged species used in electrolytes are salts, ionic liquids [1], polyelectrolytes [2], and large charged particles such as colloidal suspensions [3]. The presence of charged bodies in a solution leads to rich thermodynamic and structural phenomenon. For example, when an electrolyte solution is exposed to a low-dielectric surface, such as air, ions will (in general) deplete at the interface due to repulsive electrostatic interactions between the surface and the ions, leading to the well-known increase in surface tension of water with added salt [4, 5] and the Hofmeister series [6]. The depletion originates from air having a lower dielectric constant than the solution medium, generating a repulsive image charge as ions approach the surface. On the contrary, when an electrolyte solution is placed next to a surface with a higher dielectric constant or a surface possessing charge, ions will adsorb to the interface, forming an "electric double layer" [7] (Fig. 1.1). The term "electric double layer" refers to the "layer" of polarization or fixed charges on the inside of the surface, followed by a second layer of counterions from the solution that adsorb to the surface to neutralize the charge. The neutralization of surface charge dampens the penetration of the electrostatic force into the solution, known as *screening*.

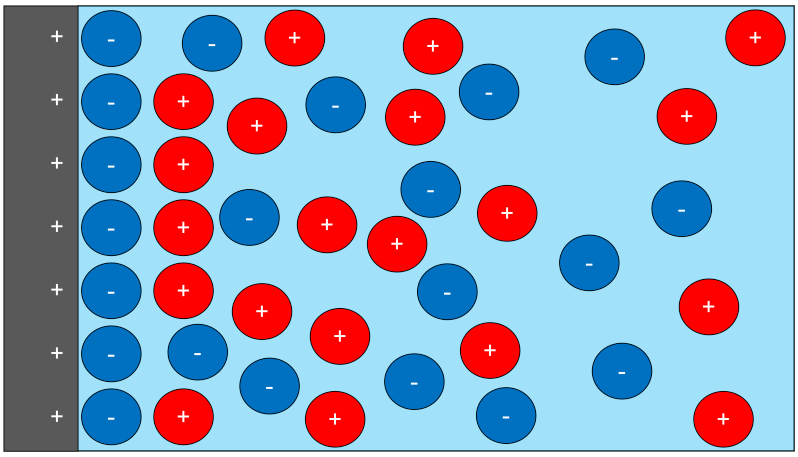

Figure 1.1: Diagram of the electric double layer formed at a charged plate in contact with an electrolyte solution.

1.2 Applications

Electrolytes are ubiquitous in science and engineering [3, 7–18] and are of active interest, owing to their applications in biology, energy storage, colloidal suspensions, and even climate. In biology, electrolytes serve essential purposes in cell function, and different types of electrolytes are required to carry out these functions. For example, simple ions like sodium and potassium are used in cellular ion pumps to carry out nerve conduction [19]. More complex electrolytes like polyelectrolytes are involved in liquid-liquid phase separation to compartmentalize a cell [20], and proteins, a type of polyampholyte, rely on particular sequences of charge to bind a particular substrate [21].

In energy storage, capacitors can store large amounts of energy through the adsorption of counterions from an electrolyte solution to the capacitor surface, referred to as a supercapacitor [22]. Batteries depend on the conduction of electrolytes through a medium to carry out electrochemical reactions at the electrode to store or release energy [23]. One vast area of research is on the improvement, or potential replacement, of lithium-ion battery, for Li-ion battery technology is plagued by safety concerns from the flammability of polar organic additives [24–27]. Several electrolyte material alternatives have been studied for their energy density, mechanical strength, and ionic conductivity, such as polymer electrolytes [28], polyelectrolytes [29], room-temperature ionic liquids [1], and zwitterions [30–32]. These materials have yet to surpass the performance of Li-ion technology though, and thus this remains a booming area of research.

Other areas include climate and environmental sciences, such as sea foaming [33], halogen release from the ocean [34], and heterogeneous reactions in seawater aerosols, where surface active halide precursors (i.e., sea salt) form halogen compounds that are harmful to the ozone layer [35]. Electrolytes are also relevant in water purification, where textile runoffs release toxic, charged organic dyes into the publicly-used waters [36]. Considering the surface propensity of ions is greatly affected by the solvation structure near an interface [37], understanding the solvation structure of bulky molecular ions like organic dyes near surfaces like filtration membranes is a relevant problem for water purification.

1.3 Open Problems

In this thesis, we are interested in theoretically modeling the interactions of electrolytes with macroscopically-large charged surfaces, specifically in electric double-

layer formation or depletion. Copious theories to describe EDL structure and forces have been developed, starting with the original work by Helmholtz [38] in 1879, followed by revisions from Gouy [39] and Chapman [40] to account for ion mobility in a solvent. Later, Stern [41] united the Helmholtz and Gouy and Chapman models to account for both bound ions at the electrode interface (the Stern layer) and the diffuse electric double layer. This Gouy–Chapman–Stern model has been used extensively in the study of EDLs. While these simpler models explain a broad spectrum of electrolyte behavior, EDLs can exhibit anomalous behaviors such as charge inversion and like-charge attraction [42]. Such behaviors occur for low molecular weight electrolytes in the strong-coupling limit where electrostatic correlations dominate, or for polyelectrolytes even well below the strong-coupling limit [7]. Even in the weak-coupling limit, boundary layer effects from image charge dominate electric double-layer structure close to the surface depending on the dielectric discontinuity [5, 43–45] and these singular boundary layers elude simple perturbative treatments [46]. Correlations in electrolytes near surfaces and their effects on electric double-layer properties are still not fully understood.

Additionally, there is a drive to improve energy storage devices through novel, high-dielectric material additives. These materials improve devices such as batteries and capacitors by increasing the dielectric constant of the ionic medium, enhancing ion conductivity and stored energy density [30–32, 47–51]. One promising class of high-dielectric materials are a type of polyelectrolyte: zwitterions. Zwitterions are molecules with an anionic and cationic group separated by covalent bonds. This structure gives zwitterions an enormous molecular dipole moment, making them versatile, nonvolatile additives that enhance the dielectric constant and ion conductivity of ionic media. We will develop a model for zwitterions and explore their capacitance applications later.

As stated above, there are an innumerable amount of problems to be addressed in electrolytes, each involving a delicate interplay of length scales of surface, electrostatic, and nonelectrostatic interactions, as well as the development of new materials for energy storage. Sometimes, even the fundamentals of electrolyte solutions are misunderstood [52]. In this thesis, we will address some of these issues using a theoretical approach, all under the general theme of interactions of electrolytes near surfaces. We start with a pedagogical formulation of thermodynamics of electrolyte solutions in Chapter 2, for it is imperative to understand this before tackling more complex problems. We then explore a particular electrolyte in Chapter 3, the zwit-

terionic polymer, its capacitance applications, double-layer structure, and screening behavior. We then turn to understanding the image-charge correlation in electrolyte solutions in Chapter 4 and systematically compare its effect on double-layer structure, capacitance, and surface forces for different surface types. Lastly, we develop a Gaussian-renormalized fluctuating theory to describe charged particles in solution with a Gaussian excluded volume interaction in Chapter 5. This theory provides a length-scale for ions that captures packing effects, unlike the incompressibility condition, and we analyze bulk correlation effects. We use field theories for all models, where discrete particles are represented as fields through a particle-to-field transformation. Although the discreteness of matter is lost with this transformation, we are mostly interested in the larger length scales of electrostatic interactions, and field theories provide us with insightful predictions on electrolyte behavior, either analytically or with little numerical cost relative to molecular dynamics simulations or Monte Carlo. An excellent text to learn field theory is *The Equilibrium Theory of Inhomogeneous Polymers* by Glenn Fredrickson [53].

We believe the content of this thesis contributes to our understanding of interactions between electrolytes and different types of surfaces as well as the design of energy storage devices with zwitterionic additives.

References

(1) Zhou, T.; Gui, C.; Sun, L., et al. *Chem. Rev.* **2023**, *123*, 12170–12253, DOI: 10.1021/acs.chemrev.3c00391.

(2) Muthukumar, M. *Macromolecules* **2017**, *50*, 9528–9560, DOI: 10.1021/acs.macromol.7b01929.

(3) Israelachvili, J., *Intermolecular and Surface Forces*, 2nd ed.; Academic Press: 1992.

(4) Wagner, C. *Phys. Z.* **1924**, *25*, 474–477.

(5) Onsager, L.; Samaras, N. N. T. *J. Chem. Phys.* **1934**, *2*, 528–536, DOI: 10.1063/1.1749522.

(6) Hofmeister, F. *Pathol. Pharmakol.* **1888**, *24*, 247–260.

(7) Åkesson, T.; Woodward, C.; Jönsson, B. *J. Chem. Phys.* **1989**, *91*, 2461–2469, DOI: 10.1063/1.457006.

(8) Honig, B.; Nicholls, A. *Science* **1995**, *268*, 1144–1149, DOI: 10.1126/science.7761829.

(9) Knipping, E. M. *Science* **2000**, *288*, 301–306, DOI: 10.1126/science.288.5464.301.

(10) Attard, P. *Curr. Opin. Colloid Interface Sci.* **2001**, *6*, 366–371, DOI: 10.1016/S1359-0294(01)00102-9.

(11) Levin, Y. *Rep. Prog. Phys.* **2002**, *65*, 1577–1632, DOI: 10.1088/0034-4885/65/11/201.

(12) Pericet-Camara, R.; Papastavrou, G.; Behrens, S. H.; Borkovec, M. *J. Phys. Chem. B* **2004**, *108*, 19467–19475, DOI: 10.1021/jp0473063.

(13) Luo, G. *Science* **2006**, *311*, 216–218, DOI: 10.1126/science.1120392.

(14) Dahirel, V.; Jardat, M. *Curr. Opin. Colloid Interface Sci.* **2010**, *15*, 2–7, DOI: 10.1016/j.cocis.2009.05.006.

(15) Moazzami-Gudarzi, M.; Maroni, P.; Borkovec, M.; Trefalt, G. *Soft Matter* **2017**, *13*, 3284–3295, DOI: 10.1039/C7SM00314E.

(16) Lee, A. A.; Perez-Martinez, C. S.; Smith, A. M.; Perkin, S. *Phys. Rev. Lett.* **2017**, *119*, 026002, DOI: 10.1103/PhysRevLett.119.026002.

(17) Groß, A.; Sakong, S. *Curr. Opin. Electrochem.* **2019**, *14*, 1–6, DOI: 10.1016/j.coelec.2018.09.005.

(18) Budkov, Y. A.; Sergeev, A. V.; Zavarzin, S. V.; Kolesnikov, A. L. *J. Phys. Chem. C* **2020**, *124*, 16308–16314, DOI: 10.1021/acs.jpcc.0c03623.

(19) Morth, J. P.; Pedersen, B. P.; Toustrup-Jensen, M. S., et al. *Nature* **2007**, *450*, 1043–1049, DOI: 10.1038/nature06419.

(20) Alberti, S.; Gladfelter, A.; Mittag, T. *Cell* **2019**, *176*, 419–434, DOI: 10.1016/j.cell.2018.12.035.

(21) Wells, J. A.; Powers, D. B.; Bott, R. R.; Graycar, T. P.; Estell, D. A. *Proc. Natl. Acad. Sci. U.S.A.* **1987**, *84*, 1219–1223, DOI: 10.1073/pnas.84.5.1219.

(22) González, A.; Goikolea, E.; Barrena, J. A.; Mysyk, R. *Renew. Sustain. Energy Rev.* **2016**, *58*, 1189–1206, DOI: 10.1016/j.rser.2015.12.249.

(23) Etacheri, V.; Marom, R.; Elazari, R.; Salitra, G.; Aurbach, D. *Energy Environ. Sci.* **2011**, *4*, 3243, DOI: 10.1039/c1ee01598b.

(24) Hammami, A.; Raymond, N.; Armand, M. *Nature* **2003**, *424*, 635–636, DOI: 10.1038/424635b.

(25) Mandal, B. K.; Padhi, A. K.; Shi, Z.; Chakraborty, S.; Filler, R. *J. Power Sources* **2006**, *161*, 1341–1345, DOI: 10.1016/j.jpowsour.2006.06.008.

(26) Bandhauer, T. M.; Garimella, S.; Fuller, T. F. *J. Electrochem. Soc.* **2011**, *158*, R1, DOI: 10.1149/1.3515880.

(27) Bouchet, R.; Phan, T. N. T.; Beaudoin, E., et al. *Macromolecules* **2014**, *47*, 2659–2665, DOI: 10.1021/ma500420w.

(28) Hallinan, D. T.; Balsara, N. P. *Annu. Rev. Mater. Res.* **2013**, *43*, 503–525, DOI: 10.1146/annurev-matsci-071312-121705.

(29) Fong, K. D.; Self, J.; Diederichsen, K. M., et al. **2019**, *5*, 1250–1260, DOI: 10.1021/acscentsci.9b00406.

(30) Tiyapiboonchaiya, C.; Pringle, J. M.; Sun, J., et al. *Nat. Mater.* **2004**, *3*, 29–32, DOI: 10.1038/nmat1044.

(31) Kim, O.; Kim, H.; Choi, U. H.; Park, M. J. *Nat. Commun.* **2016**, *7*, 13576, DOI: 10.1038/ncomms13576.

(32) Xu, H.; Li, W.; Huang, L., et al. *Sci. China Mater.* **2023**, *66*, 3799–3809, DOI: 10.1007/s40843-023-2547-y.

(33) Björneholm, O.; Hansen, M. H.; Hodgson, A., et al. *Chem. Rev.* **2016**, *116*, 7698–7726, DOI: 10.1021/acs.chemrev.6b00045.

(34) Sun, L.; Li, X.; Hede, T., et al. *J. Phys. Chem. B* **2012**, *116*, 3198–3204, DOI: 10.1021/jp209178s.

(35) Jungwirth, P.; Tobias, D. J. *Chem. Rev.* **2006**, *106*, 1259–1281, DOI: 10.1021/cr0403741.

(36) Choi, W. S.; Lee, H.-J. *Polymers* **2022**, *14*, 2183, DOI: 10.3390/polym14112183.

(37) Son, C. Y.; Wang, Z.-G. *Proc. Natl. Acad. Sci. U.S.A* **2021**, *118*, 8.

(38) Helmholtz, H. *Ann. Phys.* **1879**, *243*, 337–382, DOI: 10.1002/andp.18792430702.

(39) Gouy, M. *J. Phys. Theor. Appl.* **1910**, *9*, 457–468, DOI: 10.1051/jphystap:019100090045700.

(40) Chapman, D. L. *Philos. Mag* **1913**, *25*, 475–481, DOI: 10.1080/14786440408634187.

(41) Stern, O. *Z. Elektrochem. Angew. Phys. Chem.* **1924**, *30*, 508–516, DOI: 10.1002/bbpc.192400182.

(42) Naji, A.; Kanduč, M.; Forsman, J.; Podgornik, R. *J. Chem. Phys.* **2013**, *139*, 150901, DOI: 10.1063/1.4824681.

(43) Kjellander, R.; Marčelja, S. *Chem. Phys. Lett.* **1984**, *112*, 49–53, DOI: 10.1016/0009-2614(84)87039-6.

(44) Levin, Y. *Phys. Rev. Lett.* **2009**, *102*, 147803, DOI: 10.1103/PhysRevLett.102.147803.

(45) Wang, R.; Wang, Z.-G. *J. Chem. Phys.* **2013**, *139*, 124702, DOI: 10.1063/1.4821636.

(46) Netz, R. R.; Orland, H. *Eur. Phys. J. E* **2000**, *1*, 203–214.

(47) Zhu, L. *J. Phys. Chem. Lett.* **2014**, *5*, 3677–3687, DOI: 10.1021/jz501831q.

(48) Chen, Q.; Shen, Y.; Zhang, S.; Zhang, Q. *Annu. Rev. Mater. Res.* **2015**, *45*, 433–458, DOI: 10.1146/annurev-matsci-070214-021017.

(49) Zhao, Q.; Stalin, S.; Zhao, C.-Z.; Archer, L. A. *Nat. Rev. Mater.* **2020**, *5*, 229–252, DOI: 10.1038/s41578-019-0165-5.

(50) Mei, W.; Rothenberger, A. J.; Bostwick, J. E., et al. *Phys. Rev. Lett.* **2021**, *127*, 228001, DOI: 10.1103/PhysRevLett.127.228001.

(51) Mei, W.; Han, A.; Hickey, R. J.; Colby, R. H. *J. Chem. Phys.* **2021**, *155*, 244505, DOI: 10.1063/5.0074100.

(52) Bruch, D.; Balzer, C.; Wang, Z.-G. *J. Chem. Phys.* **2022**, *156*, 174704, DOI: 10.1063/5.0089260,

(53) Fredrickson, G. H., *The Equilibrium Theory of Inhomogenous Polymers*; Clarendon Press: 2005.

Chapter 2

THERMODYNAMICS OF ELECTROLYTE SOLUTIONS NEAR CHARGED SURFACES: CONSTANT SURFACE CHARGE VERSUS CONSTANT SURFACE POTENTIAL

Electric double layers are ubiquitous in science and engineering and are of current interest, owing to their applications in the stabilization of colloidal suspensions and as supercapacitors. While the structure and properties of electric double layers in electrolyte solutions near a charged surface are well characterized, there are subtleties in calculating thermodynamic properties from the free energy of a system with charged surfaces. These subtleties arise from the difference in the free energy between systems with constant surface charge and constant surface potential. In this chapter, we present a systematic, pedagogical framework to properly account for the different specifications on charged bodies in electrolyte solutions. Our approach is fully variational—that is, all free energies, boundary conditions, relevant electrostatic equations, and thermodynamic quantities are systematically derived using variational principles of thermodynamics. We illustrate our approach by considering a simple electrolyte solution between two charged surfaces using the Poisson–Boltzmann theory. Our results highlight the importance of using the proper thermodynamic potential and provide a general framework for calculating thermodynamic properties of electrolyte solutions near charged surfaces. Specifically, we present the calculation of the pressure and the surface tension between two charged surfaces for different boundary conditions, including mixed boundary conditions.

This chapter includes content from our previously published article:

(1) Bruch, D.; Balzer, C.; Wang, Z.-G. *J. Chem. Phys.* **2022**, *156*, 174704, DOI: 10.1063/5.0089260,

I am thankful to Dr. Chris Balzer for his insight on the thermodynamics of charged systems, especially on the topic of surface tension.

2.1 Introduction

Electric double layers (EDLs) in electrolyte solutions near a charged surface have a rich history, owing to their relevance in several fields of science and engineering [1–13]. Copious theories to describe EDL structure and forces have been developed, starting with the original work by Helmholtz [14] in 1879, followed by revisions from Gouy [15] and Chapman [16] to account for ion mobility in a solvent. Later, Stern [17] united the Helmholtz and Gouy and Chapman models to account for both bound ions at the electrode interface (the Stern layer) and the diffuse electric double layer. This Gouy–Chapman–Stern model has been used extensively in the study of EDLs. For strongly charged surfaces, EDLs can exhibit anomalous behaviors such as charge inversion and like-charge attraction [18]. Such behaviors occur for low molecular weight electrolytes in the strong-coupling limit where electrostatic correlations dominate, or for polyelectrolytes even well below the strong-coupling limit [1]. Other electrostatic correlation effects include image charge [19–22], where ions are either attracted or repelled from a surface depending on the nature of the dielectric discontinuity. EDLs remain a subject of great interest owing to their importance in applications such as energy storage in supercapacitors [23] and stabilization of colloidal suspensions [2, 24–27].

Most theoretical formulations rely on constructing a free energy of the system. Various thermodynamic properties can be calculated from derivatives of this free energy. One notable property in EDLs is the pressure (or force) between charged surfaces. For example, in colloidal systems, according to Derjaguin–Landau–Verwey–Overbeek (DLVO) theory [24], the interplay between EDL repulsion and van der Waals interactions determines the stability of a colloidal suspension. The pressure can be calculated by differentiating a free energy for the system; however, the relevant free energy at equilibrium is different for surfaces with constant surface charge versus constant surface potential. Consequently, the proper free energy must be used to correctly obtain the pressure, and other thermodynamic properties.

The difference between the free energies for constant surface charge and surface potential conditions is the energy to charge/discharge bodies at constant surface potential. As other thermodynamic variables vary, energy is required to supply or remove charge from the surfaces to maintain constant surface potential. This was recognized and rigorously accounted for over 50 years ago in the works of Verwey and Overbeek [28], Landau and Lifshitz [29], and Feynman [30] for isolated charged bodies. Likewise, many authors over the last several decades extended this

to charged bodies in the presence of electrolyte solutions in a rigorous, consistent manner, through the Legendre transform or a Lagrange multiplier [31–39]. In recent decades, however, the difference between these free energies has often not been explicitly discussed [40–45]. As we will explore, the difference in thermodynamic potential amounts to whether surface terms are included in the free energy. Of central importance, some authors do not include surface terms in their free energies and instead absorb these terms into boundary conditions. Other authors explicitly include surface terms in the free energy. Presently, there is no accepted convention on whether surface terms should be included. As we will show later, omitting the surface terms amounts to using a Legendre transformed free energy, relevant only for specified surface potential. While not including surface terms is valid and correct, without an explicit explanation, the role of surface terms in the free energy can cause confusion for the readers.

Gupta et al. recently published a study that proposed a framework to treat the thermodynamics of EDLs near charged bodies [46]. A central point in their work was invoking a term they called U_{charge} to be added to the internal energy for the system, whose form depends on different specifications of the boundary condition: $U_{\text{charge}} = 0$ for constant surface charge, and $\int_{\mathscr{B}} \sum_j q_j \psi_j d^2\mathbf{r}$ for constant surface potential, where ψ and q are respectively the surface potential and charge in their notation. They applied their framework to both a mean-field model of an electrolyte in the Poisson–Boltzmann approximation and to an electrolyte model with strong electrostatic correlations described by a modified Gauss's law. A motivation for their work is their view that the U_{charge} term was overlooked in several previously published works [47–56] (Refs. 30–32, 36, 44–49 in Gupta et al.). Their approach yields correct equations for properties such as the ion-density profile and pressure between charged surfaces; however, some aspects of the thermodynamics presented in Ref. [46] could be derived in a more pedagogical and thermodynamically consistent manner. For example, allowing internal energy to have different form (and value) depending on whether surface charge or surface potential is specified, contradicts the fact that the internal energy is a state function whose value is uniquely specified for a given state no matter what state variable is used to specify that state. Instead, under conditions of specified surface potential, the relevant energy is an enthalpy-like new energy given by the Legendre transform $H = U - \int_{\mathscr{B}} \sum_j q_j \psi_j d^2\mathbf{r}$, where the last term is the work associated with charging/discharging the externally charged body at constant potential; the different specifications of the boundary condition correspond to different thermodynamic ensembles. The constant surface

charge and constant surface potential boundary conditions are associated with different thermodynamic potentials (free energies) that are related to each other through the Legendre transform. If one does not use the free energy to calculate thermodynamic quantities, the issue of the Legendre transform does not arise, as is the case in Refs. [47–56]. Furthermore, by writing the differential form of U_{charge} as $\delta U_{\text{charge}} = \int_{\mathscr{B}} \sum_j \psi_j \delta q_j d^2\mathbf{r}$ (Eq. (4) of Ref. [46]) instead of the total differential $\delta U_{\text{charge}} = \int_{\mathscr{B}} \sum_j \left(\psi_j \delta q_j + q_j \delta \psi_j\right) d^2\mathbf{r}$, one would not be able to produce the correct differential form of the Legendre transformed thermodynamic potential, from which many useful relations (e.g., Maxwell relations) follow.

In this chapter, we seek to present a concise, systematic, and pedagogical framework to properly account for different specified conditions on charged bodies in electrolyte solutions. Starting from a system with specified surface charge, we construct the appropriate free energy, and then perform a Legendre transform to obtain a new free energy for a system with specified surface potential. All governing equations, including the Poisson–Boltzmann equation, boundary conditions, interplate pressure, etc., are systematically derived from the appropriate free energy through variational conditions and by taking the appropriate thermodynamic derivatives. We note that the work by Reiner and Radke [31] also uses a variational approach to derive Poisson–Boltzmann and other governing equations and does so rigorously. However, our work seeks to serve as a pedagogical introduction to the most relevant information regarding the different specifications of the charged surfaces, whereas the work of Reiner and Radke [31] is more fitting for the advanced reader. The fact that confusions still persist despite the existence of their work justifies the need for further clarification. Additionally, our analysis shows that the boundary conditions are a natural consequence of variation of the relevant free energy, and emphasizes that surface potential and surface charge are not only boundary conditions, but are also important thermodynamic variables for charged systems.

The rest of this article is organized as follows. First, we construct the variational grand free energy, then systematically derive the ion densities and the Poisson–Boltzmann equation for an electrolyte solution in the presence of a general external charge distribution. We then discuss the subtleties of fixed surface charge and fixed surface potential boundary conditions for parallel plates in an electrolyte solution, and relate the relevant thermodynamic potentials for each case using the Legendre transform. We further show that the U_{charge} term introduced by Gupta et al. [46] naturally arises from the Legendre transform. Additionally, we verify

the thermodynamic consistency of our approach by showing that constant surface potential and constant surface charge boundary conditions are a natural consequence of variation of the relevant thermodynamic potential. To emphasize the importance of properly treating the free energy, we discuss two thermodynamic properties—pressure between the surfaces and surface tension. We show that using the incorrect thermodynamic potential leads to a qualitatively incorrect pressure between the plates at constant surface potential. For the surface tension, we show that it is associated with a natural thermodynamic potential, regardless of the boundary condition. Our work concludes with an example of mixed boundary conditions—one plate at constant surface charge and the other at constant surface potential—to demonstrate the simplicity of treating the energetics with such specifications using our approach. We show that mixed boundary conditions predict "unlike-charge repulsion" even at the mean-field Poisson–Boltzmann level, which would not have been captured without using the proper free energy. We emphasize that although variational approaches have been previously used [31], and the Legendre transform has been implemented in the literature [31–39], here we present them in a unified, pedagogical framework to clarify the energetics of electrolyte solutions in the presence of charged bodies.

2.2 Variational Free Energy

We begin our pedagogical framework by constructing the variational grand free energy for an electrolyte solution near a general external charge distribution, from which we will later show that the Poisson–Boltzmann equation (PBE) and boundary conditions naturally follow by variation of the grand free energy [31, 57]. We start with a general free energy functional and later take the Poisson–Boltzmann limit; however, taking this limit does not compromise the generality of the approach.

Consider a general system of an external charge distribution with charge density ρ_{ex} submerged in a bath of a symmetric (ion valencies $Z_+ = Z_- = Z$), binary electrolyte solution. The bulk ion concentration is c_{B}. Since our focus is on developing a framework, we will take the ion valencies to be $Z = 1$ for simplicity. The solvating medium is assumed to be a dielectric continuum with uniform electric permittivity ϵ. The Helmholtz free energy of our system is written as a sum of ideal, excess, and mean-field electrostatic contributions

$$F = F_{\text{id}} + F_{\text{ele}} + F_{\text{ex}}. \tag{2.1}$$

The ideal portion is given by the free energy of an inhomogeneous mixture of an ideal gas of ions

$$\beta F_{\text{id}} = \int \mathrm{d}\mathbf{r}\, c_+(\mathbf{r})\left\{ \ln\left[c_+(\mathbf{r})v_0^+\right] - 1\right\} + \int \mathrm{d}\mathbf{r}\, c_-(\mathbf{r})\left\{ \ln\left[c_-(\mathbf{r})v_0^-\right] - 1\right\} \tag{2.2}$$

where $\beta = 1/kT$, k is the Boltzmann constant, $c_\pm$ are the number densities of the ions, and $v_0^\pm$ are the characteristic volumes of the ions. We note that some authors use the thermal wavelength cubed as the volume scale [58]. The choice of volume scale is inconsequential—it merely results in a concentration-independent shift in the chemical potential.

The excess term is a general contribution arising from electrostatic correlations and other non-electrostatic interactions between charged particles and depends only on the ion number densities $F_{\text{ex}} = F_{\text{ex}}[c_+, c_-]$. The mean-field electrostatic contribution is simply the Coulomb energy of the system

$$\beta F_{\text{ele}} = \frac{\beta e^2}{2} \int \mathrm{d}\mathbf{r} \int \mathrm{d}\mathbf{r}' \rho(\mathbf{r}) C(\mathbf{r}, \mathbf{r}') \rho(\mathbf{r}') \tag{2.3a}$$

$$C(\mathbf{r}, \mathbf{r}') = \frac{1}{4\pi\epsilon|\mathbf{r} - \mathbf{r}'|} \tag{2.3b}$$

where ρ is the net mean charge density in the system

$$e\rho = e(\rho_{\text{ex}} + c_+ - c_-) \tag{2.4}$$

with e being the elementary charge and ρ_{ex} being the charge density of the external charged body, which includes any surface charge terms. Here, ρ and ρ_{ex} are in units of length^{-3} and charge units have been explicitly written as the elementary charge e. As discussed earlier, several authors [40, 41, 43–45] do not include surface charge terms. This convention amounts to using a Legendre transformed free energy corresponding to specified surface potential conditions, which we will discuss later. Technically, both conventions are valid; however, for clarity and consistency, we believe it is best practice to directly include surface terms in the free energy and Legendre transform thereafter.

Noting an identity for the quadratic form in Eq. (2.3a), the quadratic interactions can be decoupled at the expense of a new coupling to the variable ψ [59], the

mean-electrostatic potential. Applying this identity and integrating by parts, the electrostatic contribution can be written as

$$\beta F_{\text{ele}} = \beta \int \mathrm{d}\mathbf{r} \left\{ e\rho(\mathbf{r})\psi(\mathbf{r}) - \frac{\epsilon}{2} \left[\nabla\psi(\mathbf{r})\right]^2 \right\}. \tag{2.5}$$

We note that, in order to recover Eq. (2.3), ψ satisfies the following variational condition

$$\frac{\delta\beta F_{\text{ele}}}{\delta\psi} = 0. \tag{2.6}$$

Upon defining the Bjerrum length $l_{\text{B}} = e^2/4\pi\epsilon kT$ and redefining $\psi = \beta e\psi$ for notational simplicity, we obtain the full variational Helmholtz free energy

$$\begin{aligned}\beta F = \int \mathrm{d}\mathbf{r} \Big\{ &(\rho_{\text{ex}} + c_+ - c_-)\psi - \frac{1}{8\pi l_{\text{B}}} (\nabla\psi)^2 \\ &+ c_+ \left[\ln\left(c_+ v_0^+\right) - 1\right] + c_- \left[\ln\left(c_- v_0^-\right) - 1\right] \Big\} + \beta F_{\text{ex}}[c_+, c_-]. \end{aligned} \tag{2.7}$$

Since our system is submerged in an electrolyte solution bath, the relevant thermodynamic potential at equilibrium is the grand free energy. The grand free energy is obtained from a Legendre transform

$$W = F - \int \mathrm{d}\mathbf{r}(\mu_+ c_+ + \mu_- c_-). \tag{2.8}$$

Thus

$$\begin{aligned}\beta W = \int \mathrm{d}\mathbf{r} \Big\{ &(\rho_{\text{ex}} + c_+ - c_-)\psi - \frac{1}{8\pi l_{\text{B}}} (\nabla\psi)^2 \\ &+ c_+ \left[\ln\left(c_+ v_0^+\right) - 1\right] + c_- \left[\ln\left(c_- v_0^-\right) - 1\right] \\ &- (\beta\mu_+ c_+ + \beta\mu_- c_-) \Big\} + \beta F_{\text{ex}}[c_+, c_-]. \end{aligned} \tag{2.9}$$

We note that W also satisfies the variational condition in ψ

$$\frac{\delta\beta W}{\delta\psi} = 0. \tag{2.10}$$

Additionally, by the variational principle of thermodynamic potentials [60], equilibrium is obtained from the variational condition of W with respect to the unconstrained internal variables $c_\pm$

$$\frac{\delta\beta W}{\delta c_\pm} = 0. \tag{2.11}$$

The variational conditions in ψ and $c_\pm$ yield

$$\nabla^2\psi = -4\pi l_\mathrm{B}(\rho_\mathrm{ex} + c_+ - c_-) \tag{2.12}$$

$$c_\pm = \frac{e^{\beta\mu_\pm}}{\nu_0^\pm} e^{\mp\psi} \exp\left[-\frac{\delta\beta F_\mathrm{ex}}{\delta c_\pm}\right]. \tag{2.13}$$

Taking $F_\mathrm{ex} = 0$ recovers the Poisson–Boltzmann limit $c_\pm = \frac{e^{\beta\mu_\pm}}{\nu_0^\pm} e^{\mp\psi}$. Setting the reference potential such that $\psi = 0$ in the bulk solution, we obtain

$$c_\pm = c_\mathrm{B} e^{\mp\psi}. \tag{2.14}$$

Lastly, after substituting Eq. (2.14) into (2.12) we have

$$\nabla^2\psi = -4\pi l_\mathrm{B}\left[\rho_\mathrm{ex} - 2c_\mathrm{B}\sinh(\psi)\right] \tag{2.15}$$

which is the Poisson–Boltzmann equation. The grand free energy becomes

$$\beta W = \int \mathrm{d}\mathbf{r}\left[-\frac{1}{8\pi l_\mathrm{B}}(\nabla\psi)^2 + \rho_\mathrm{ex}\psi - 2c_\mathrm{B}\cosh(\psi)\right]. \tag{2.16}$$

2.3 Specified Surface Charge

We now examine the subtleties between fixed surface charge and surface potential conditions, beginning with the case of fixed surface charge. Consider a system composed of two parallel plates submerged in an electrolyte solution bath depicted in Fig. 2.1. The solution contains a symmetric, binary, monovalent electrolyte with bulk ion concentration c_B. The left and right plates have specified surface charge Q_1 and Q_2, respectively, and corresponding *unknown* surface potentials $\mathscr{V}_1$ and $\mathscr{V}_2$. The plates have surface area A and are separated by a distance L. The surface charge densities are then $\sigma_1 = Q_1/A$ and $\sigma_2 = Q_2/A$. Making use of the equations derived

in the last section, the Poisson–Boltzmann equation (PBE) and resulting grand free energy for our system becomes

$$\frac{\mathrm{d}^2\psi}{\mathrm{d}z^2} = -4\pi l_\mathrm{B}\left[\sigma_1\delta(z) + \sigma_2\delta(z-L) - 2c_\mathrm{B}\sinh(\psi)\right] \tag{2.17}$$

$$\beta W = A\int_0^L \mathrm{d}z\left[-\frac{1}{8\pi l_\mathrm{B}}\left(\frac{\mathrm{d}\psi}{\mathrm{d}z}\right)^2 - 2c_\mathrm{B}\cosh(\psi)\right] + \psi(0)Q_1 + \psi(L)Q_2 \tag{2.18}$$

where we have invoked $\rho_\mathrm{ex} = \sigma_1\delta(z) + \sigma_2\delta(z-L)$ to explicitly include the surface charge for parallel plates and $\delta(z)$ is the Dirac delta function.

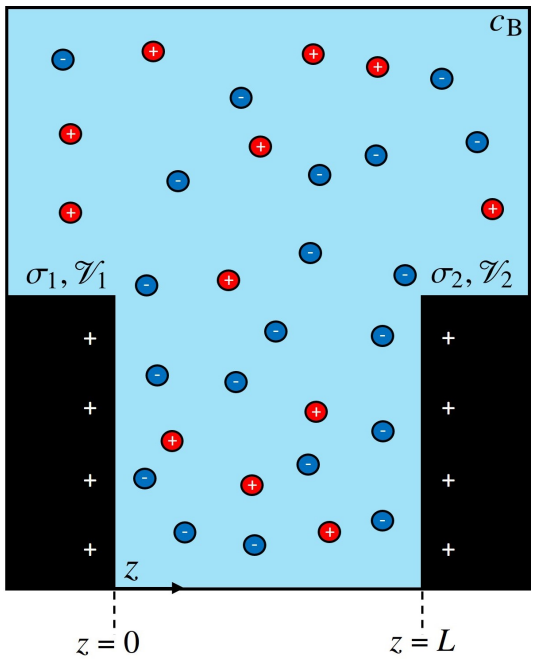

Figure 2.1: A symmetric binary electrolyte solution containing two fully submerged parallel plates in contact with an infinitely large reservoir. The bulk solution has ion concentration c_B, and the ions have valency $Z = 1$. The left and right plates have surface charge density and surface potential σ_1, $\mathscr{V}_1$ and σ_2, $\mathscr{V}_2$, respectively, and are located at $z = 0$ and $z = L$. Here, the surface charge densities and surface potentials are in units of length^{-2} and energy/charge, respectively. The plates have area A and are separated by a distance L. The system volume is $V = AL$.

Since we specify the plates in Fig. 2.1 to have fixed surface charge, namely Q_1 on the left plate and Q_2 on the right, the system is described by a T, V, A, $\mu_\pm$, Q_1, Q_2

ensemble. We emphasize that Q_1 and Q_2 are treated as thermodynamic variables that define the system. Accordingly, the relevant free energy at equilibrium is the grand free energy, $W(T, V, A, \mu_\pm, Q_1, Q_2)$. The differential form of W is

$$dW = -SdT - PdV + \gamma dA - N_+ d\mu_+ - N_- d\mu_- + e\mathscr{V}_1 dQ_1 + e\mathscr{V}_2 dQ_2 \tag{2.19}$$

where S is the system entropy, P is the pressure in the film (region of electrolyte solution between the parallel plates), γ is the surface tension, and N_+ and N_- are the number of positive and negative ions given by $N_\pm = \int_V \mathrm{d}\mathbf{r}\, c_\pm$. Because the solvent is treated implicitly, P is actually the osmotic pressure while γ is the excess surface tension with respect to the surface tension between the solid surface and the pure solvent. Henceforth we will use the simpler terms pressure and surface tension, respectively, to refer to these quantities. The $\mathscr{V}\, dQ$ terms correspond to the electrostatic work required to add dQ charges to the surface at a potential $\mathscr{V}$. Note that we have explicitly included the elementary charge, e, to remain consistent with our definition of the charge density in the preceding section. For conciseness, the surface tension refers to the surface tension of the two surfaces ($\gamma = \gamma_1 + \gamma_2$) since we do not separately consider each solid-liquid interface. Finally, we note that a differential change in volume is clearly coupled to the differential change in area ($dV = AdL + LdA$) for the confined system. We will revisit the pressure and surface tension later on.

As discussed earlier, W satisfies the variational conditions Eq. (2.10) and Eq. (2.11) with respect to ψ and the internal unconstrained variables $c_\pm$, and these conditions yield the PBE given by Eq. (2.17). Thus, the PBE determines ψ and $c_\pm$ and is a natural consequence of variation of W. Moreover, the PBE naturally admits fixed surface charge boundary conditions, obtained by integrating the PBE from $z = 0^-$ to $z = 0^+$ for the left plate and $z = L^-$ to $z = L^+$ for the right plate

$$\left.\frac{\mathrm{d}\psi}{\mathrm{d}z}\right|_{z=0^+} - \left.\frac{\mathrm{d}\psi}{\mathrm{d}z}\right|_{z=0^-} = -4\pi l_\mathrm{B}\sigma_1 \tag{2.20}$$

$$\left.\frac{\mathrm{d}\psi}{\mathrm{d}z}\right|_{z=L^+} - \left.\frac{\mathrm{d}\psi}{\mathrm{d}z}\right|_{z=L^-} = -4\pi l_\mathrm{B}\sigma_2 \tag{2.21}$$

where the $2c_\mathrm{B}\cosh(\psi)$ term dropped out by continuity of ψ. Noting the electric field vanishes inside each plate by Gauss's law and charge neutrality, we obtain fixed surface charge boundary conditions

$$\sigma_1 = -\frac{1}{4\pi l_B}\left.\frac{d\psi}{dz}\right|_{z=0} \tag{2.22}$$

$$\sigma_2 = \frac{1}{4\pi l_B}\left.\frac{d\psi}{dz}\right|_{z=L}. \tag{2.23}$$

Furthermore, we take advantage of the differential form of W in Eq. (2.19) to obtain expressions for the thermodynamic conjugates of the surface charges, the surface potentials $\mathscr{V}_1$ and $\mathscr{V}_2$

$$e\mathscr{V}_1 = \left(\frac{\partial W}{\partial Q_1}\right)_{T,V,A,\mu_\pm,Q_2}; \quad e\mathscr{V}_2 = \left(\frac{\partial W}{\partial Q_2}\right)_{T,V,A,\mu_\pm,Q_1}. \tag{2.24}$$

To perform these derivatives, we invoke functional chain rule

$$\left(\frac{\partial W}{\partial Q_1}\right)_{T,V,A,\mu_\pm,Q_2} = \left(\frac{\partial W}{\partial Q_1}\right)_{T,V,A,\mu_\pm,Q_2,\psi,c_\pm} + \int_0^L \frac{\delta W}{\delta \psi}\frac{\partial \psi}{\partial Q_1}dz + \int_0^L \frac{\delta W}{\delta c_\pm}\frac{\partial c_\pm}{\partial Q_1}dz \tag{2.25}$$

and similarly for the Q_2 derivative. In principle, ψ and $c_\pm$ are functions of Q_1 and Q_2. However, we see the importance of the variational conditions Eqs. (2.10) and (2.11), which remove the last two terms of Eq. (2.25). Accordingly, the Q_i derivatives can be taken without regard to the dependence of ψ and $c_\pm$ on Q_i. Evaluating these derivatives in Eq. (2.24) yields

$$\beta e\mathscr{V}_1 = \psi(0; Q_1, Q_2); \quad \beta e\mathscr{V}_2 = \psi(L; Q_1, Q_2). \tag{2.26}$$

The function dependence on other state variables (T, V, A, $\mu_\pm$) is omitted for notational brevity, and this convention will be adopted for the remainder of the article. Thus, variation of W in Q_1 and Q_2 reveals that the conjugate variables to Q_1 and Q_2, $\mathscr{V}_1$ and $\mathscr{V}_2$, respectively, are naturally determined from the electrostatic potential evaluated at the surface of each plate. Therefore, under fixed surface charge conditions, variation of the proper free energy, W, naturally admits fixed surface charge boundary conditions and relationships for the conjugate surface potentials.

2.4 Specified Surface Potential

If the plates have specified surface potentials, namely $\mathscr{V}_1$ and $\mathscr{V}_2$, then the system is described by a T, V, A, $\mu_\pm, \mathscr{V}_1$, $\mathscr{V}_2$ ensemble, and the relevant free energy at equilibrium is now different from W. The new, relevant thermodynamic potential, denoted Y, is given by the Legendre transform of the grand free energy with respect to the surface charge of each plate fixed at constant surface potential [29, 32–38].

$$Y[\psi; \mathscr{V}_1, \mathscr{V}_2] = W[\psi; Q_1, Q_2] - e\mathscr{V}_1 Q_1 - e\mathscr{V}_2 Q_2 \tag{2.27}$$

and, using Eq. (2.19), the differential of this potential is

$$dY = -SdT - PdV + \gamma dA - N_+ d\mu_+ - N_- d\mu_- - eQ_1 d\mathscr{V}_1 - eQ_2 d\mathscr{V}_2 \tag{2.28}$$

where Q_1 and Q_2 are now unconstrained internal variables of Y *to be determined* by minimization of Y at specified surface potentials $\mathscr{V}_1$ and $\mathscr{V}_2$. This new potential Y can be interpreted as a "grand-like" free energy, where the surface potentials are fixed and the surface charges can fluctuate. Physically, the Legendre transform subtracts the electrostatic work associated with charging/discharging the plates at constant surface potential. Thus, the change in Y bounds the non-electrostatic work for a constant surface potential process taking place at isothermal conditions with fixed reservoir chemical potentials. Furthermore, note that $eQ_1\mathscr{V}_1 + eQ_2\mathscr{V}_2$ is equivalent to U_{charge} from Ref. [46] for the case of parallel plates. Thus, our analysis provides the thermodynamic foundation for this term that was introduced phenomenologically in Ref. [46]. Lastly, our analysis shows that U_{charge} should only be included for thermodynamic potentials that correspond to specified surface potential.

To verify the thermodynamic consistency of free energy Y, we note that Y also satisfies the variational conditions in ψ and $c_\pm$

$$\frac{\delta Y}{\delta \psi} = 0 \tag{2.29a}$$

$$\frac{\delta Y}{\delta c_\pm} = 0. \tag{2.29b}$$

Applying these conditions to Y returns the Poisson–Boltzmann equation as expected. As mentioned before, Q_1 and Q_2 are now internal unconstrained variables. Therefore, at equilibrium, Y satisfies the variational conditions

$$\left(\frac{\partial Y}{\partial Q_1}\right)_{T,V,A,\mu_\pm,\mathscr{V}_1,\mathscr{V}_2;Q_2,\psi,c_\pm} = 0 \tag{2.30}$$

$$\left(\frac{\partial Y}{\partial Q_2}\right)_{T,V,A,\mu_\pm,\mathscr{V}_1,\mathscr{V}_2;Q_1,\psi,c_\pm} = 0. \tag{2.31}$$

In the subscripts of Eqs. (2.30) and (2.31), we use a semicolon to separate system-specifying variables $T, V, A, \mu_\pm, \mathscr{V}_1$, and $\mathscr{V}_2$ from the unconstrained variational variables Q_1, Q_2, ψ, and $c_\pm$. These derivatives are taken at constant Q_2 and Q_1, respectively, because they are partial derivatives. Additionally, Eqs. (2.30) and (2.31) are taken at constant ψ and $c_\pm$ due to variational conditions on ψ and $c_\pm$ as discussed in the previous section. Applying the variational conditions on Q_i to the Legendre transform given in Eq. (2.27) yields

$$\left(\frac{\partial W}{\partial Q_1}\right)_{T,V,A,\mu_\pm,\mathscr{V}_1,\mathscr{V}_2;Q_2,\psi,c_\pm} = e\mathscr{V}_1 \tag{2.32}$$

$$\left(\frac{\partial W}{\partial Q_2}\right)_{T,V,A,\mu_\pm,\mathscr{V}_1,\mathscr{V}_2;Q_1,\psi,c_\pm} = e\mathscr{V}_2. \tag{2.33}$$

Evaluating these derivatives gives

$$\psi(0;Q_1,Q_2) = \beta e\mathscr{V}_1; \quad \psi(L;Q_1,Q_2) = \beta e\mathscr{V}_2. \tag{2.34}$$

Therefore, at specified surface potential, constant surface potential boundary conditions are a natural consequence of variation of the proper free energy Y and are given by setting the electrostatic potential at the surface of the plate to be the specified surface potential. These boundary conditions also serve as an implicit equation to determine the unknown surface charges, Q_1 and Q_2—equations of state of the form $Q_1 = f(\mathscr{V}_1, \mathscr{V}_2)$ and $Q_2 = f(\mathscr{V}_1, \mathscr{V}_2)$. We emphasize that both W and Y naturally produce the same $Q_1 = f(\mathscr{V}_1, \mathscr{V}_2)$ and $Q_2 = f(\mathscr{V}_1, \mathscr{V}_2)$ equations of state, Eqs. (2.26) and (2.34), as expected by thermodynamic consistency. The only subtlety to highlight is that Eq. (2.26) expresses $\mathscr{V}_1$ and $\mathscr{V}_2$ as functions of Q_1 and Q_2, and Eq. (2.34) expresses Q_1 and Q_2 as functions of $\mathscr{V}_1$ and $\mathscr{V}_2$, but are still equivalent equations of state. This is analogous to the equation of state of a gas, where one can either obtain the pressure by specifying the density in a canonical ensemble, or determine the density by specifying the pressure in an isobaric ensemble. Noting

the boundary conditions in Eq. (2.34), we can now apply the Legendre transform in Eq. (2.27) to W and obtain an expression for Y

$$\beta Y = A \int_0^L \mathrm{d}z \left[-\frac{1}{8\pi l_\mathrm{B}} \left(\frac{\mathrm{d}\psi}{\mathrm{d}z} \right)^2 - 2c_\mathrm{B} \cosh(\psi) \right]. \tag{2.35}$$

Compared to W in Eq. (2.18), Y does not explicitly contain the boundary terms. Therefore, we see that omitting the surface charge terms in W would give Y, amounting to a Legendre transformed free energy.

2.5 Interplate Force

We now provide a brief analytical calculation of the interplate force. The pressure in the film P is related to the pressure of bulk reservoir P_bulk by the disjoining pressure $\Pi_D \equiv P - P_\mathrm{bulk}$. At constant surface charge, the pressure between the plates is obtained from a derivative of W

$$PA = -\left(\frac{\partial W}{\partial L} \right)_{T,A,\mu_\pm,Q_1,Q_2}. \tag{2.36}$$

The partial derivative is taken at constant A so the differential volume is proportional to the differential in the plate separation L. Similarly, at constant surface potential, the pressure is obtained from a derivative of Y

$$PA = -\left(\frac{\partial Y}{\partial L} \right)_{T,A,\mu_\pm,\mathscr{V}_1,\mathscr{V}_2}. \tag{2.37}$$

It can be shown that, upon applying Eqs. (2.36) and (2.37) to Eqs. (2.18) and (2.35), respectively, and making use of the Poisson–Boltzmann equation, Eq. (2.17), both derivatives result in the general expression

$$\beta P = -\frac{1}{8\pi l_\mathrm{B}} \left(\frac{d\psi}{dz} \right)^2 + 2c_\mathrm{B} \cosh(\psi) \tag{2.38}$$

which can be evaluated at any position since the pressure is constant between the plates by mechanical equilibrium. Derivation of Eq. (2.38) requires careful manipulation of the free energy and is deferred to the Appendix. The first term on the right-hand side of Eq. (2.38) is the isotropic part of the Maxwell stress tensor [61], and the second term is the entropic contribution from the ions in the presence

of a potential ψ. For the symmetric case ($Q_1 = Q_2 = Q$ or $\mathscr{V}_1 = \mathscr{V}_2 = \mathscr{V}$), the gradient of the potential at the midplane is zero so that

$$\beta P = 2c_{\mathrm{B}} \cosh\left(\psi|_{L/2}\right). \tag{2.39}$$

Eq. (2.39) is an equation of state known from the contact value theorem [2]. As expected, Eq. (2.36) and Eq. (2.37) yield equivalent expressions because a system's equilibrium state in a reversible process is independent of boundary conditions. In fact, Eq. (2.39), together with the $\mathscr{V}$–Q equation of state (either Eq. (2.26) or (2.34)), constitute the P–$\mathscr{V}$ or P–Q equation of state. Both are equivalent—one can simply interchange between P as a function of $\mathscr{V}$ and P as a function of Q using the $\mathscr{V}$–Q equation of state. Furthermore, specifying Q or specifying $\mathscr{V}$ in a reversible process simply corresponds to different paths taken on a $\mathscr{V}$–Q surface. Changing the path taken affects the work done and heat exchanged, but the same pressure equation of state is valid everywhere along any path. This is analogous to an ideal gas, where the ideal gas law is valid regardless of the process (e.g., adiabatic, isothermal). However, we stress that to obtain Eq. (2.39) from a thermodynamic derivative, it is necessary to use the correct thermodynamic potential for the specified conditions. A straightforward substitution of Eq. (2.27) into (2.37) for symmetric plate surface potentials gives the following identity

$$\begin{aligned} PA = -\left(\frac{\partial Y}{\partial L}\right)_{T,A,\mu_\pm,\mathscr{V}} &= -\left(\frac{\partial (W - 2e\mathscr{V}Q)}{\partial L}\right)_{T,A,\mu_\pm,\mathscr{V}} \\ &= -\left(\frac{\partial W}{\partial L}\right)_{T,A,\mu_\pm,\mathscr{V}} + 2e\mathscr{V}\left(\frac{\partial Q}{\partial L}\right)_{T,A,\mu_\pm,\mathscr{V}}. \end{aligned} \tag{2.40}$$

This identity can also be derived directly from Eq. (2.19) by dividing by dL and applying constant temperature, chemical potentials, and surface potential. From Eq. (2.40), attempting to obtain the pressure solely by differentiating W at constant surface potential neglects the last term in Eq. (2.40), which accounts for the charging/discharging of the plates as they move. We will explore the relative importance of the last two terms later.

2.6 Surface Tension

We close our discussion of thermodynamic consistency with a brief discussion of the surface tension of an electrolyte solution, an important quantity in studying

the wettability of surfaces, especially in electrowetting applications [62]. The thermodynamic definition of surface tension introduced by Gibbs [63] is commonly used to calculate surface tension. The basis of Gibbs's formulation is to divide the inhomogeneous system into homogeneous *bulk* phases separated by a *surface* region. The majority of discussion in the time since has been focused on the application of Gibbs's concept of dividing surfaces to curved surfaces and cases where the system is not macroscopic [64–72]. Here, we only wish to clarify the role of charged solid surfaces on the surface tension. To this end, we calculate surface tension in a confined system with charged, planar surfaces. We find that the natural thermodynamic potential to evaluate the surface tension is related to the Legendre transform between constant surface charge and surface potential. From the differential form of W and Y,

$$\gamma = \left(\frac{\partial W}{\partial A}\right)_{T,V,\mu_\pm,Q_1,Q_2} = \left(\frac{\partial Y}{\partial A}\right)_{T,V,\mu_\pm,\mathscr{V}_1,,\mathscr{V}_2}. \tag{2.41}$$

Writing $dV = AdL + LdA$ in Eqs. (2.19) and (2.28), we also have,

$$\begin{aligned} \gamma A \quad &= A\left(\frac{\partial W}{\partial A}\right)_{T,L,\mu_\pm,Q_1,Q_2} + PV \\ &= A\left(\frac{\partial Y}{\partial A}\right)_{T,L,\mu_\pm,\mathscr{V}_1,,\mathscr{V}_2} + PV. \end{aligned} \tag{2.42}$$

Since at fixed T,L,$\mu_\pm$,$\mathscr{V}_1$,$\mathscr{V}_2$, the potential Y is extensive in area A, the derivative in the second line of Eq. (2.42) is simply Y/A. Therefore,

$$\gamma A = Y + PV. \tag{2.43}$$

The last term on the right-hand side of Eq. (2.43) corresponds to the grand potential of a homogeneous system at film pressure P, i.e., $PV = (\Pi_D + P_{\text{bulk}})V = -W_0 = -Y_0$ where subscript 0 indicates a homogeneous system, and for such a system, $W_0 = Y_0$ since there are no surface charge or potential terms.

Equation (2.43) can be understood from another perspective. Since W is a first-order, homogeneous equation in its extensive variables (V, A, Q_1, Q_2), we have

$$W = V\left(\frac{\partial W}{\partial V}\right)_{T,A,\mu_\pm,Q_1,Q_2} + A\left(\frac{\partial W}{\partial A}\right)_{T,V,\mu_\pm,Q_1,Q_2} + Q_1\left(\frac{\partial W}{\partial Q_1}\right)_{T,V,A,\mu_\pm,Q_2} + Q_2\left(\frac{\partial W}{\partial Q_2}\right)_{T,V,A,\mu_\pm,Q_1}. \tag{2.44}$$

The partial derivatives on the right-hand side can be identified from the differential form of W in Eq. (2.19), leading to the following Euler equation

$$W - eQ_1\mathscr{V}_1 - eQ_2\mathscr{V}_2 = -PV + \gamma A. \tag{2.45}$$

The left-hand side is exactly the definition of Y from the Legendre transform of W.

The surface tension is commonly evaluated using the integral form of the free energy such that $\gamma A = \Omega - \Omega_{\text{bulk}} = \Omega + P_{\text{bulk}}V$, where Ω is a type of grand free energy. The *bulk* subscript indicates that the interface is in contact with a macroscopic, bulk phase. The confined system has an additional $\Pi_D V$ term due to the difference in the film pressure from the pressure of the bulk reservoir. For a charged system, the common expression for surface tension is only valid when Ω is the "grand-like" free energy Y, not the grand free energy W, regardless of whether the system is characterized by constant surface charge or constant surface potential.

Within PB theory, one can analytically obtain the result for the surface tension using the previous expressions for Y from Eq. (2.35) and P from Eq. (2.38) in Eq. (2.43).

$$\beta\gamma = -\frac{1}{4\pi l_{\text{B}}}\int_0^L \mathrm{d}z\left(\frac{\mathrm{d}\psi}{\mathrm{d}z}\right)^2. \tag{2.46}$$

We see that, like in the pressure expression Eq. (2.38), the electric field generates a negative contribution to surface tension, reflecting the effect of the Maxwell stress [61]. The usual definition is identical to the definition using Y when $P = P_{\text{bulk}}$, which strictly corresponds to the limit where $L \to \infty$. Using the PB equation, one can analytically evaluate this limit to obtain the surface tension when the two surfaces are infinitely separated

$$\beta\gamma_\infty = -\frac{2}{\pi\lambda_D l_{\text{B}}}\left\{\sinh^2\left[\frac{\psi(0)}{4}\right] + \sinh^2\left[\frac{\psi(L)}{4}\right]\right\} \tag{2.47}$$

where λ_D is the Debye screening length given by $\lambda_D = 1/\sqrt{8\pi l_B c_B}$. In the expression for γ_∞, the separate contributions from each surface are additive. Note that the above expression is valid even when the two surfaces are at different potentials. Both Eqs. (2.46) and (2.47) were derived by Reiner and Radke [31], who also presented analytical results in the Debye-Hückel limit. In the special case of symmetric plates at infinite separation, the total interfacial tension is twice that for a single surface. Substituting the exact relationship between ψ and σ for a single plate into Eq. (2.47), we obtain

$$\beta\gamma_\infty = \frac{-2\sigma^2\sqrt{2\pi\frac{l_B}{c_B}}}{1+\sqrt{\frac{\pi\sigma^2 l_B}{2c_B}+1}}. \tag{2.48}$$

The thermodynamic potential Y naturally leads to a useful Maxwell relation involving the surface tension. From the differential form of the free energy in Eq. (2.28), one has the following Maxwell relation,

$$\left(\frac{\partial\gamma}{\partial e\mathscr{V}_1}\right)_{T,V,\mu_\pm,\mathscr{V}_2} = -\left(\frac{\partial Q_1}{\partial A}\right)_{T,V,\mu_\pm,\mathscr{V}_2} = -\sigma_1 \tag{2.49}$$

with a similar equation in which indices 1 and 2 are switched. The equation above can be considered to be a general form of the Lippmann equation [73] for the confined system. In the limit of infinite surface separation or for a single surface, one can write the more common form, which has been noted by several authors [74–78],

$$\left(\frac{\partial\gamma}{\partial e\mathscr{V}}\right)_{T,V,\mu_\pm} = -\left(\frac{\partial Q}{\partial A}\right)_{T,V,\mu_\pm}. \tag{2.50}$$

2.7 Illustrative Examples

As we showed above, simple analytical expressions for the pressure and surface tension can be obtained at the Poisson–Boltzmann level. This is not always possible (e.g., complex free energy functionals), and one may need to numerically differentiate or use the integral form of the free energy to obtain the quantities. However, differentiating W under constant surface potential conditions yields an incorrect pressure. This can be seen analytically from the identity given by Eq. (2.40). Likewise, using $\gamma A = W + PV$ yields the incorrect surface tension, regardless of the

boundary condition. We first demonstrate the calculation of the pressure by numerically evaluating the pressure under constant surface charge density and constant surface potential conditions for the system depicted in Fig. 2.1.

Fig. 2.2a shows the disjoining pressure in the electrolyte solution as a function of plate separation for symmetric plates at constant surface charge density ($\sigma_1 = \sigma_2 = \sigma$). As the plates come together, the pressure diverges due to the repulsion of the positive charges on the plates. The initial decay with increasing distance is very rapid, stemming from nonlinearities at high surface potential. The rapid decay is followed by a long-range, exponential decay arising from electrostatic screening of the plates due to the electric double layer present at the plate surfaces, with a length scale dictated by the Debye length. This result agrees with other authors [36, 42].

Fig. 2.2b shows the disjoining pressure as a function of plate separation at constant surface potential ($\mathscr{V}_1 = \mathscr{V}_2 = \mathscr{V}$), calculated by numerically differentiating Y given by Eq. (2.35) (blue dots), and theoretically using Eq. (2.39) (blue line). The numerically correct and theoretical curves are in agreement and predict repulsion between the plates at all separation distances. Moreover, the repulsion is weaker at close separation for constant surface potential compared to constant surface charge density. At constant surface potential, the plates discharge to satisfy the boundary conditions (see Fig. 2.2c); however, for fixed surface charge density, the surface charge density remains constant and the surface potential and force diverge at close separation. Another important feature is that the curves saturate at zero separation for the case of constant surface potential. Interestingly enough, this saturation relates to a solvation energy for the plates. The area under the pressure curve is the negative of the free energy of separating the two surfaces at contact—when the surfaces are not exposed to the electrolyte solution—to infinity— when the two surfaces are fully solvated by the solution. Although the decay length of the pressure at constant surface potential appears to be larger than at constant surface charge density, the inset plots of Figs. 2.2a and 2.2b show that both decay lengths are the same and equal to the Debye screening length, $\lambda_D = 3.07$ nm for the given conditions. Lastly, from Fig. 2.2b, the red curve (given by the penultimate term of Eq. (2.40)) predicts attraction between the plates despite both being like-charged—a qualitatively incorrect result. The result is further invalidated by Fig. 2.2c, where we see the that plates are positively charged at all separation distances and, thus, are expected to always repel.

Now, we explore the relative importance of the last two terms in Eq. (2.40) for

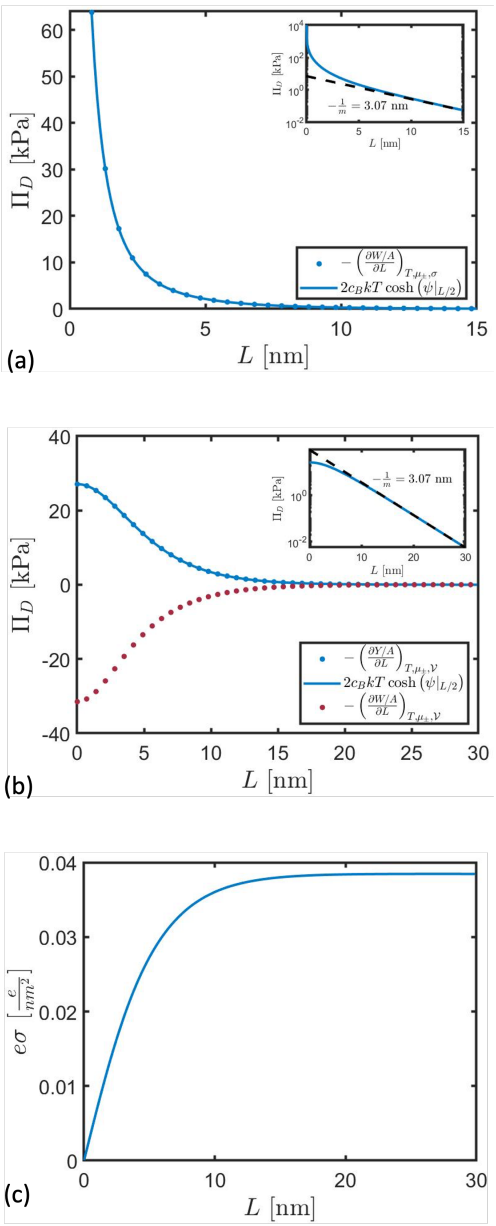

Figure 2.2: Disjoining pressure $\Pi_D \equiv P - P_{\text{bulk}}$ and surface charge density for an electrolyte solution at constant surface charge density and constant surface potential. The solution has bulk concentration $c_{\text{B}} = 0.01\ M$, temperature $T = 300$ K, and Bjerrum length $l_{\text{B}} = 0.7$ nm. (a) Pressure at constant surface charge density $e\sigma = 0.01\ e/\text{nm}^2$, calculated by numerically differentiating Eq. (2.18) (blue dots) and theoretically (blue line) with Eq. (2.39). (b) Pressure at constant surface potential $\mathcal{V} = 1\ kT/e$, calculated by numerically differentiating Eq. (2.35) (blue dots), theoretically (blue line) with Eq. (2.39), and incorrectly evaluated (red dots) by numerically differentiating W, the first term on the rightmost side of Eq. (2.40). (c) Surface charge density on the plates in (b). Insets: Semilog y plot of the theoretical pressure (Eq. (2.39)), where m is the slope of the curve in the linear regime.

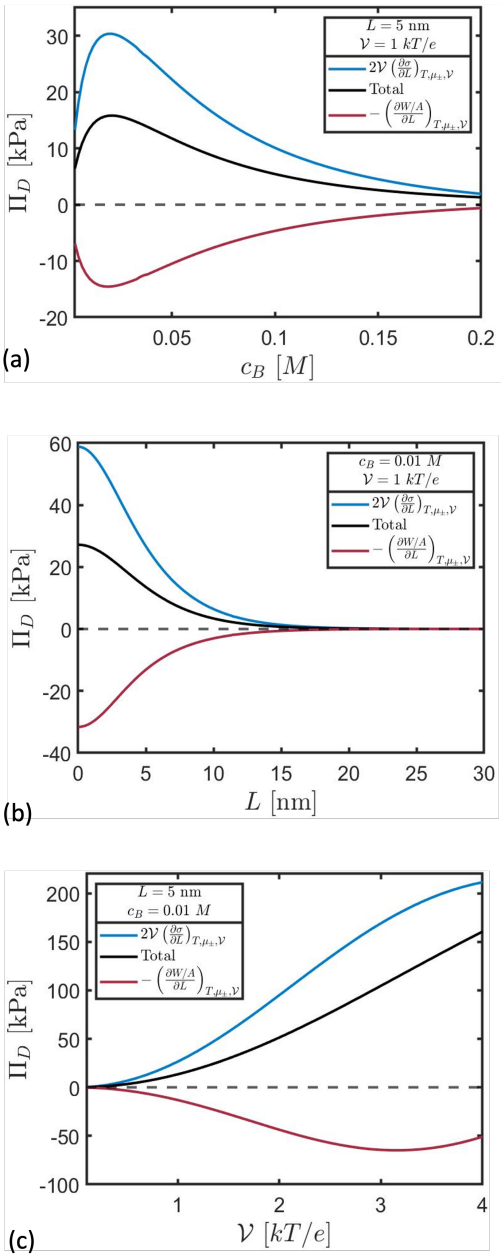

Figure 2.3: Relative contributions of the last two terms of Eq. (2.40) to Π_D as a function of c_B, L, and $\mathscr{V}$. The solution conditions are $T = 300\,K$ and $l_\mathrm{B} = 0.7$ nm. The dashed line shows the zero line for clarity. (a) Pressure contributions versus bulk concentration c_B at $L = 5$ nm and $\mathscr{V} = 1\,kT/e$. (b) Pressure contributions versus plate separation L at $c_\mathrm{B} = 0.01\,M$ and $\mathscr{V} = 1\,kT/e$. (c) Pressure contributions versus surface potential $\mathscr{V}$ at $c_\mathrm{B} = 0.01\,M$ and $L = 5$ nm.

various c_B, L, and $\mathscr{V}$. In Fig. 2.3, we see that the last two terms of Eq. (2.40) are nearly equally important for all conditions considered. Moreover, the contribution to the pressure from the charging/discharging of the plates (blue line, last term of Eq. (2.40)) is always repulsive, whereas the contribution from the grand free energy (red curve, penultimate term of Eq. (2.40)) is always attractive. As an aside, the total pressure in Fig. 2.3b was calculated by adding the individual terms on the right hand side of Eq. (2.40), $-\left(\frac{\partial W}{\partial L}\right)_{T,A,\mu_\pm,\mathscr{V}}$ and $2e\mathscr{V}\left(\frac{\partial Q}{\partial L}\right)_{T,A,\mu_\pm,\mathscr{V}}$. On the other hand, the total pressure in Fig. 2.2b was calculated by directly differentiating Y given by Eq. (2.35). Both curves match, thus proving the equality of Eq. (2.40) and further verifying the thermodynamic consistency of our approach. Lastly, we can perform a final check of thermodynamic consistency using a Maxwell relation. From the differential form of Y given by Eq. (2.28), we can write the following Maxwell relation for symmetric plates

$$\left(\frac{\partial P}{\partial e\mathscr{V}}\right)_{T,A,\mu_\pm} = 2\left(\frac{\partial Q}{\partial V}\right)_{T,A,\mu_\pm} = 2\left(\frac{\partial \sigma}{\partial L}\right)_{T,\mu_\pm}. \tag{2.51}$$

Evaluating the left and right derivatives from Figs. 2.3c and 2.2c, respectively, under the same conditions ($\mathscr{V} = 1\,kT/e$, $L = 5$ nm, and $c_\mathrm{B} = 0.01\,M$) gives $\partial P/\partial\mathscr{V} = 2e\partial\sigma/\partial L = 6.4\times10^{-3}\,e/\mathrm{nm}^3$, which confirms the thermodynamic consistency.

Turning to the surface tension, we first examine the scaling behavior of the surface tension at infinite plate separation γ_∞. The results are shown in Fig. 2.4, where γ_∞ is calculated using Eq. (2.48) as a function of surface charge density for various bulk concentrations. From Fig. 2.4, we see that the magnitude of the surface tension scales quadratically for low σ, but becomes linear for large σ. The surface tension also loses dependence on the bulk concentration at large σ (we note, however, that this regime may exceed the range of validity of the PB theory). At low surface charge density, the surface tension increases in magnitude with decreasing bulk concentration because the surface potential is linearly increasing in the Debye length. The crossover from the quadratic to the linear regimes occurs at a lower surface charge density for low concentrations.

Now, we move to the case of the surface tension at a finite separation length between the plates. We examine its variation with the plate separation; the results are shown in Fig. 2.5, where the blue line is the correct calculation of the surface tension by Eq. (2.43), the red line is calculated incorrectly from the grand potential $\gamma A = W + PV$,

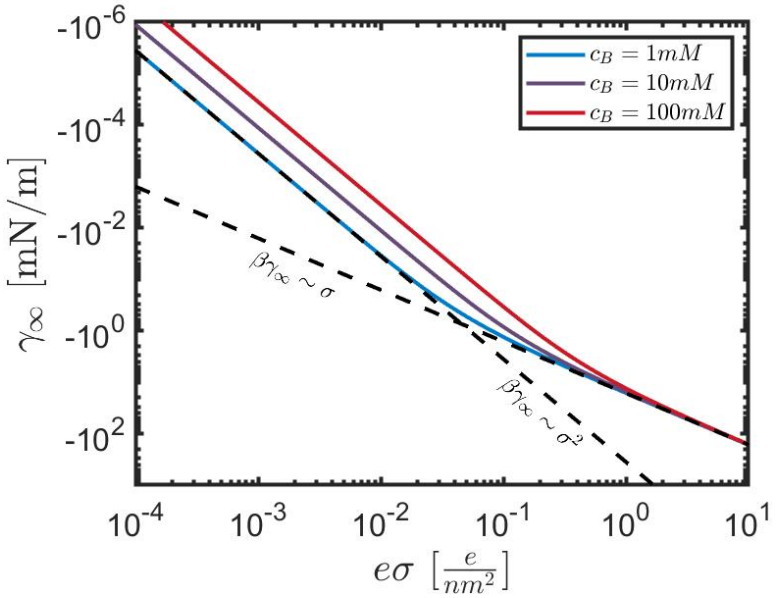

Figure 2.4: Surface tension at infinite plate separation of a confined electrolyte solution as a function of surface charge density for various bulk concentrations, calculated from Eq. (2.48). The solution conditions are $T = 300\,\mathrm{K}$ and $l_\mathrm{B} = 0.7\,\mathrm{nm}$.

and the black dotted line is the value of the surface tension at infinite separation. Clearly, the expression using Y captures the predicted behavior for large L by Eq. (2.47). For the particular conditions in Fig. 2.5, using W instead of Y would lead to qualitatively different conclusions with regard to both the sign and the trend. We highlight these results for using the wrong expression $\gamma A = W + PV$ to heed caution in calculating the surface tension. As discussed in the introduction, the literature is not always clear in what is meant by "grand potential," often using the same language for W and Y-type potentials; only the latter is the correct potential for computing the interfacial tension.

We end this section by examining mixed boundary conditions—the left plate at constant surface charge density and the right plate at constant surface potential. Taking advantage of the framework developed earlier, we obtain the corresponding thermodynamic potential by Legendre transforming W for the right plate with specified surface potential. The free energy and pressure are thus given by

$$X = W - e\mathscr{V}_2 Q_2 \tag{2.52}$$

$$PA = -\left(\frac{\partial X}{\partial L}\right)_{T,A,\mu_\pm,Q_1,\mathscr{V}_2}. \tag{2.53}$$

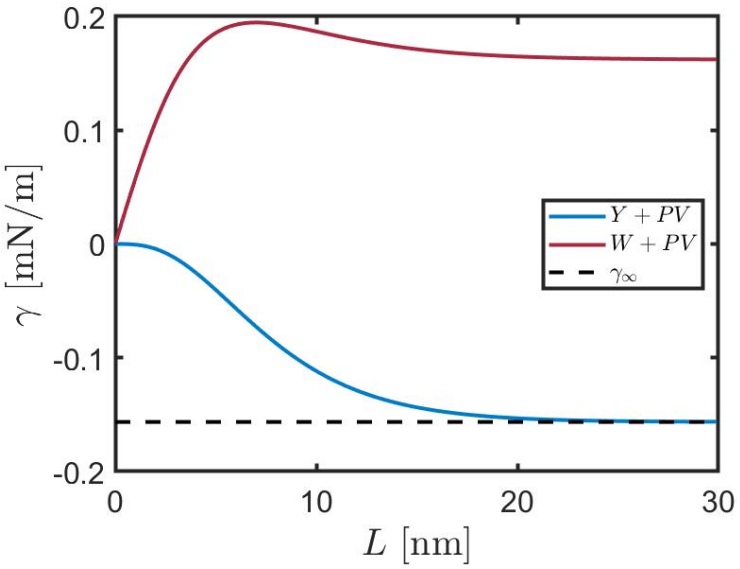

Figure 2.5: Surface tension of a confined electrolyte solution for varying plate separation calculated using Eq. (2.43) (blue) and $\gamma A = W + PV$ (red). The surface tension at infinite separation γ_∞ is calculated using Eq. (2.47). The surfaces have fixed surface potential $\mathscr{V} = 1\ kT/e$. The solution conditions are $c_\mathrm{B} = 0.01\ M$, $T = 300$ K, and $l_\mathrm{B} = 0.7$ nm.

Fig. 2.6a shows the disjoining pressure as a function of plate separation with mixed boundary conditions. From Fig. 2.6a, we see that the profiles saturate at zero separation. As discussed earlier, this is best interpreted in terms of the solvation energy of two plates, where one plate is at fixed surface charge density and the other is at fixed surface potential. Furthermore, from Fig. 2.6b, the surface charge density on the right plate at zero separation is simply equal and opposite the surface charge density of the left plate to satisfy charge neutrality. From Fig. 2.6, the most intriguing result is the pressure profile for $\mathscr{V}_2 = -1\ kT/e$. At moderate separation, the constant surface potential plate is negatively charged so the plates are attractive as expected. However, at close separation (< 4 nm), the plates become repulsive despite still being oppositely charged as shown in Fig. 2.6b. Surprisingly, the ion density profiles at a separation $L = 1$ nm in Fig. 2.6c reveal that the ion layer present on the surface of the left plate undergoes charge inversion—that is, the ion layer switches from accumulation of negative ions to accumulation of positive ions on the positively charged left plate, causing "unlike-charge repulsion" at close separation. This phenomenon at the Poisson–Boltzmann level was first reported in Refs. [42, 79]. It is important to emphasize that, while unlike-charged plates can repel, like-charged plates can never attract at the Poisson–Boltzmann level, although like-

charged attraction is possible at the Poisson–Boltzmann level in curved geometries [80].

2.8 Conclusion

In chapter, we presented a pedagogical framework to clarify the subtleties of specified surface charge and specified surface potential conditions using a variational approach and the Legendre transform. For specified surface charge, both the Poisson–Boltzmann equation and fixed surface charge boundary conditions follow naturally from variation of the grand free energy W. For specified surface potential, we demonstrate that the Poisson–Boltzmann equation and constant surface potential boundary conditions are natural consequences of variation of the thermodynamic potential Y—a new thermodynamic potential obtained from the Legendre transform of W. We further verify the thermodynamic consistency of our approach by showing both W and Y result in the same pressure equation of state. The thermodynamic potential Y is shown to be the natural connection to interfacial tension, regardless of whether the surface is characterized by constant surface charge or constant surface potential. Lastly, we provide some illustrative examples to emphasize the importance of properly treating the free energy.

The framework presented can be directly applied to any electrostatic system in parallel plate geometry, even with electrostatic correlations, such as image charge. For example, it can be applied to calculating work in charging-discharging processes for capacitance application, as well as phase equilibrium in electrowetting of surfaces [81, 82]. In the electrowetting of surfaces, an electrolyte solution in contact with a surface at fixed surface potential would require a Y like free energy for determining the transition. In its current form, our framework is limited to slab geometries, as the system size is characterized conveniently by area A and separation L. It would be interesting to extend the framework to curved geometries, where Ref. [80] predicts like-charge attraction between two metal spheres even at the Poisson-Boltzmann level.

2.A Derivation of Interplate Pressure

Here, we present a derivation of Eq. (2.38) by application of the derivative from Eq. (2.37) to Y, given by Eq. (2.35). Although the derivation has been done before [28, 83], we provide it here for completeness. We start with the Poisson–Boltzmann equation, given by

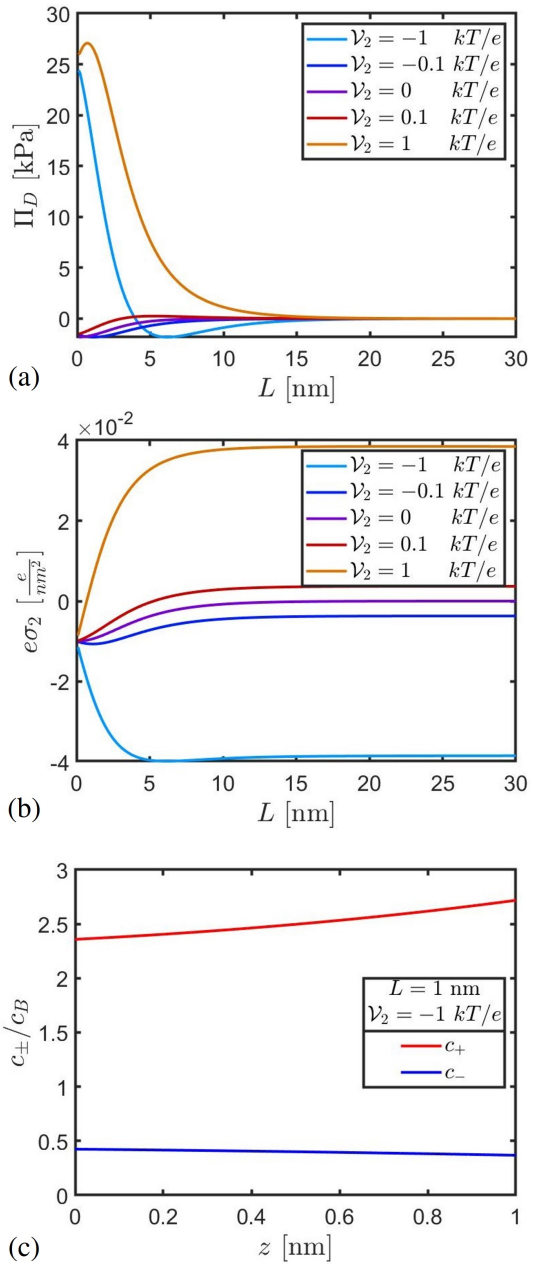

Figure 2.6: Disjoining pressure and surface charge density for an electrolyte solution with the left plate at constant surface charge density $e\sigma_1 = 0.01\, e/\text{nm}^2$ and the right plate at various constant surface potentials. The solution conditions are $c_\text{B} = 0.01M$, $T = 300$ K, and $l_\text{B} = 0.7$ nm. (a) The disjoining pressure was calculated by numerically differentiating X given by Eq. (2.52). (b) Surface charge density on the right plate versus plate separation L. (c) Positive and negative ion density profiles versus distance from the plate at separation $L = 1$ nm and right plate surface potential $\mathcal{V}_2 = -1\ kT/e$.

$$\frac{\mathrm{d}^2\psi}{\mathrm{d}z^2} = 8\pi l_\mathrm{B} c_\mathrm{B} \sinh(\psi). \tag{2.54}$$

Rewriting the left-hand side as $\frac{\mathrm{d}^2\psi}{\mathrm{d}z^2} = \frac{1}{2}\frac{\mathrm{d}}{\mathrm{d}\psi}\left(\frac{\mathrm{d}\psi}{\mathrm{d}z}\right)^2$ and integrating gives

$$-\frac{1}{8\pi l_\mathrm{B}}\left(\frac{\mathrm{d}\psi}{\mathrm{d}z}\right)^2 + 2c_\mathrm{B}\cosh(\psi) = \text{constant}. \tag{2.55}$$

The constant can be found by evaluating Eq. (2.55) at any point in the confined system. We evaluate it at some arbitrary position $z = \xi$ between the two plates, and denote its value as $C(\xi)$; thus

$$C(\xi) = -\frac{1}{8\pi l_\mathrm{B}}\left(\frac{\mathrm{d}\psi}{\mathrm{d}z}\right)^2 + 2c_\mathrm{B}\cosh(\psi). \tag{2.56}$$

It is important to stress that although $C(\xi)$ is constant in position z, it still depends on plate separation L.

Using Eq. (2.56) in Eq. (2.35), we obtain

$$\beta Y/A = -LC(\xi) - \frac{1}{4\pi l_\mathrm{B}}\int_0^L \mathrm{d}z\left(\frac{\mathrm{d}\psi}{\mathrm{d}z}\right)^2. \tag{2.57}$$

Next, we rewrite the last term of Eq. (2.57) as an integral over ψ instead of z by making use of Eq. (2.56)

$$\beta Y/A = -LC(\xi) - \frac{1}{4\pi l_\mathrm{B}}\int_{\psi_0=\mathscr{V}_1}^{\psi_L=\mathscr{V}_2} \mathrm{d}\psi\sqrt{16\pi l_\mathrm{B} c_\mathrm{B}\cosh(\psi) - 8\pi l_\mathrm{B} C(\xi)}. \tag{2.58}$$

Applying the derivative from Eq. (2.37) to Eq. (2.58) yields

$$\begin{aligned}\beta P &= -\left(\frac{\partial \beta Y/A}{\partial L}\right)_{T,A,\mu_\pm,\mathscr{V}_1,\mathscr{V}_2} \\ &= C(\xi) + L\frac{\partial C(\xi)}{\partial L} - \frac{\partial C(\xi)}{\partial L}\int_{\mathscr{V}_1}^{\mathscr{V}_2}\mathrm{d}\psi\frac{1}{\sqrt{16\pi l_\mathrm{B} c_\mathrm{B}\cosh(\psi) - 8\pi l_\mathrm{B} C(\xi)}}.\end{aligned} \tag{2.59}$$

Upon switching the integration in Eq. (2.59) back to z, the integral yields simply L, resulting in exact cancellation of the last two terms. Therefore,

$$\beta P = C(\xi) = -\frac{1}{8\pi l_{\mathrm{B}}}\left(\frac{d\psi}{dz}\right)^2 + 2c_{\mathrm{B}}\cosh(\psi). \tag{2.60}$$

References

(1) Åkesson, T.; Woodward, C.; Jönsson, B. *J. Chem. Phys.* **1989**, *91*, 2461–2469, DOI: 10.1063/1.457006.

(2) Israelachvili, J., *Intermolecular and Surface Forces*, 2nd ed.; Academic Press: 1992.

(3) Honig, B.; Nicholls, A. *Science* **1995**, *268*, 1144–1149, DOI: 10.1126/science.7761829.

(4) Knipping, E. M. *Science* **2000**, *288*, 301–306, DOI: 10.1126/science.288.5464.301.

(5) Attard, P. *Curr. Opin. Colloid Interface Sci.* **2001**, *6*, 366–371, DOI: 10.1016/S1359-0294(01)00102-9.

(6) Levin, Y. *Rep. Prog. Phys.* **2002**, *65*, 1577–1632, DOI: 10.1088/0034-4885/65/11/201.

(7) Pericet-Camara, R.; Papastavrou, G.; Behrens, S. H.; Borkovec, M. *J. Phys. Chem. B* **2004**, *108*, 19467–19475, DOI: 10.1021/jp0473063.

(8) Luo, G. *Science* **2006**, *311*, 216–218, DOI: 10.1126/science.1120392.

(9) Dahirel, V.; Jardat, M. *Curr. Opin. Colloid Interface Sci.* **2010**, *15*, 2–7, DOI: 10.1016/j.cocis.2009.05.006.

(10) Moazzami-Gudarzi, M.; Maroni, P.; Borkovec, M.; Trefalt, G. *Soft Matter* **2017**, *13*, 3284–3295, DOI: 10.1039/C7SM00314E.

(11) Lee, A. A.; Perez-Martinez, C. S.; Smith, A. M.; Perkin, S. *Phys. Rev. Lett.* **2017**, *119*, 026002, DOI: 10.1103/PhysRevLett.119.026002.

(12) Groß, A.; Sakong, S. *Curr. Opin. Electrochem.* **2019**, *14*, 1–6, DOI: 10.1016/j.coelec.2018.09.005.

(13) Budkov, Y. A.; Sergeev, A. V.; Zavarzin, S. V.; Kolesnikov, A. L. *J. Phys. Chem. C* **2020**, *124*, 16308–16314, DOI: 10.1021/acs.jpcc.0c03623.

(14) Helmholtz, H. *Ann. Phys.* **1879**, *243*, 337–382, DOI: 10.1002/andp.18792430702.

(15) Gouy, M. *J. Phys. Theor. Appl.* **1910**, *9*, 457–468, DOI: 10.1051/jphystap:019100090045700.

(16) Chapman, D. L. *Philos. Mag* **1913**, *25*, 475–481, DOI: 10.1080/14786440408634187.

(17) Stern, O. *Z. Elektrochem. Angew. Phys. Chem.* **1924**, *30*, 508–516, DOI: 10.1002/bbpc.192400182.

(18) Naji, A.; Kanduč, M.; Forsman, J.; Podgornik, R. *J. Chem. Phys.* **2013**, *139*, 150901, DOI: 10.1063/1.4824681.

(19) Onsager, L.; Samaras, N. N. T. *J. Chem. Phys.* **1934**, *2*, 528–536, DOI: 10.1063/1.1749522.

(20) Kjellander, R.; Marčelja, S. *Chem. Phys. Lett.* **1984**, *112*, 49–53, DOI: 10.1016/0009-2614(84)87039-6.

(21) Levin, Y. *Phys. Rev. Lett.* **2009**, *102*, 147803, DOI: 10.1103/PhysRevLett.102.147803.

(22) Wang, R.; Wang, Z.-G. *J. Chem. Phys.* **2013**, *139*, 124702, DOI: 10.1063/1.4821636.

(23) Burt, R.; Birkett, G.; Zhao, X. S. *Phys. Chem. Chem. Phys.* **2014**, *16*, 6519, DOI: 10.1039/c3cp55186e.

(24) Derjaguin, B. V.; Churaev, N. V.; Muller, V. M., *Surface Forces*; Springer US: Boston, MA, 1987, DOI: 10.1007/978-1-4757-6639-4.

(25) Hidalgo-Álvarez, R.; Martín, A.; Fernández, A., et al. *Adv. Colloid Interface Sci.* **1996**, *67*, 1–118, DOI: https://doi.org/10.1016/0001-8686(96)00297-7.

(26) Fall, A. B.; Lindström, S. B.; Sundman, O.; Ödberg, L.; Wågberg, L. *Langmuir* **2011**, *27*, 11332–11338, DOI: 10.1021/la201947x.

(27) Wennerström, H.; Vallina Estrada, E.; Danielsson, J.; Oliveberg, M. *Proc. Natl. Acad. Sci. USA* **2020**, *117*, 10113–10121, DOI: 10.1073/pnas.1914599117.

(28) Verwey, E.; Overbeek, J. T. G., *Theory of the Stability of Lyophobic Colloids: The Interaction of Sol Particles Having an Electric Double Layer*; Elsevier Publishing Company Inc.: 1948, pp 51–91, DOI: 10.1021/j150453a001.

(29) Landau, L. D.; Bell, J. S.; Kearsley, M. J., et al., *Electrodynamics of Continuous Media*; Pergamon Press: 1960.

(30) Richard Feynman In *The Feynman Lectures on Physics Vol. II Ch. 8: Electrostatic Energy*; Basic Books: 1964.

(31) Reiner, E. S.; Radke, C. J. *Faraday Trans.* **1990**, *86*, 3901, DOI: 10.1039/ft9908603901.

(32) Trizac, E. *Langmuir* **2001**, *17*, 4793–4798, DOI: 10.1021/la010213h.

(33) Paillusson, F.; Barbi, M.; Victor, J.-M. *Mol. Phys.* **2009**, *107*, 1379–1391, DOI: 10.1080/00268970902893156.

(34) Partenskii, M. B.; Jordan, P. C. *Phys. Rev. E* **2009**, *80*, 011112, DOI: 10.1103/PhysRevE.80.011112.

(35) Limmer, D. T.; Merlet, C.; Salanne, M., et al. *Phys. Rev. Lett.* **2013**, *111*, 106102, DOI: 10.1103/PhysRevLett.111.106102.

(36) Gray, C. G.; Stiles, P. J. *Eur. J. Phys.* **2018**, *39*, 053002, DOI: 10.1088/1361-6404/aaca5a.

(37) Chao, H.; Wang, Z.-G. *J. Phys. Chem. Lett.* **2020**, *11*, 1767–1772, DOI: 10.1021/acs.jpclett.0c00023.

(38) Oshiki, J.; Nakano, H.; Sato, H. *J. Chem. Phys.* **2021**, *154*, 144107, DOI: 10.1063/5.0047992.

(39) Cats, P.; van Roij, R. *J. Chem. Phys.* **2021**, *155*, 104702, DOI: 10.1063/5.0064315.

(40) Borukhov, I.; Andelman, D.; Orland, H. *J. Phys. Chem. B* **1999**, *103*, 5042–5057, DOI: 10.1021/jp990055r.

(41) Huang, H.; Ruckenstein, E. *Langmuir* **2006**, *22*, 3174–3179, DOI: 10.1021/la0527947.

(42) Ben-Yaakov, D.; Andelman, D. *Physica A* **2010**, *389*, 2956–2961, DOI: 10.1016/j.physa.2010.01.022.

(43) Huang, H.; Ruckenstein, E. *Langmuir* **2012**, *28*, 16300–16305, DOI: 10.1021/la303918p.

(44) Nakayama, Y.; Andelman, D. *J. Chem. Phys.* **2015**, *142*, 044706, DOI: 10.1063/1.4906319.

(45) Gavish, N.; Elad, D.; Yochelis, A. *J. Phys. Chem. Lett.* **2018**, *9*, 36–42, DOI: 10.1021/acs.jpclett.7b03048.

(46) Gupta, A.; Govind Rajan, A.; Carter, E. A.; Stone, H. A. *J. Phys. Chem. C* **2020**, *124*, 26830–26842, DOI: 10.1021/acs.jpcc.0c08554.

(47) Borukhov, I.; Andelman, D.; Orland, H. *Electrochim. Acta* **2000**, *46*, 221–229, DOI: 10.1016/S0013-4686(00)00576-4.

(48) Kornyshev, A. A. *J. Phys. Chem. B* **2007**, *111*, 5545–5557, DOI: 10.1021/jp067857o.

(49) Bazant, M. Z.; Storey, B. D.; Kornyshev, A. A. *Phys. Rev. Lett.* **2011**, *106*, 046102, DOI: 10.1103/PhysRevLett.106.046102.

(50) Ben-Yaakov, D.; Andelman, D.; Podgornik, R. *J. Chem. Phys.* **2011**, *134*, 074705, DOI: 10.1063/1.3549915.

(51) Storey, B. D.; Bazant, M. Z. *Phys. Rev. E* **2012**, *86*, 056303, DOI: 10.1103/PhysRevE.86.056303.

(52) Chanda, S.; Das, S. *Phys. Rev. E* **2014**, *89*, 012307, DOI: 10.1103/PhysRevE.89.012307.

(53) Han, Y.; Huang, S.; Yan, T. *J. Phys.: Condens. Matter* **2014**, *26*, 284103, DOI: 10.1088/0953-8984/26/28/284103.

(54) Bier, S.; Gavish, N.; Uecker, H.; Yochelis, A. *Phys. Rev. E* **2017**, *95*, 060201, DOI: 10.1103/PhysRevE.95.060201.

(55) Gupta, A.; Stone, H. A. *Langmuir* **2018**, *34*, 11971–11985, DOI: 10.1021/acs.langmuir.8b02064.

(56) De Souza, J. P.; Bazant, M. Z. *J. Phys. Chem. C* **2020**, *124*, 11414–11421, DOI: 10.1021/acs.jpcc.0c01261.

(57) Wang, Z.-G. In *Variational Methods in Molecular Modeling*, Wu, J., Ed.; Springer Singapore: Singapore, 2017, pp 1–29.

(58) Jin, Z.; Wu, J. *J. Phys. Chem. B* **2011**, *115*, 1450–1460, DOI: 10.1021/jp110066z.

(59) Wang, Z.-G. *J. Theor. Comput. Chem.* **2008**, *07*, 397–419, DOI: 10.1142/S0219633608003824.

(60) Callen, H., *Thermodynamics and an Introduction to Thermostatics*, 2nd ed.; Wiley: 1985.

(61) Griffiths, D. J., *Introduction to electrodynamics*, 3rd ed; Prentice Hall: Upper Saddle River, N.J, 1999.

(62) Moon, H.; Kim, C. J. C., *Electrowetting: Thermodynamic foundation and application to microdevices*; Springer, Boston, MA: 2007, pp 203–239, DOI: 10.1007/978-0-387-68424-6_5.

(63) Gibbs, J. W. *Trans. Connect. Acad. Arts Sci.* **1874**, *3*.

(64) Tolman, R. C. *J. Chem. Phys.* **1948**, *16*, 758–774, DOI: 10.1063/1.1746994.

(65) Kirkwood, J. G.; Buff, F. P. *J. Chem. Phys.* **1949**, *17*, 338–343, DOI: 10.1063/1.1747248.

(66) Koenig, F. O. *J. Chem. Phys.* **1950**, *18*, 449–459, DOI: 10.1063/1.1747660.

(67) Hill, T. L. *J. Chem. Phys.* **1962**, *36*, 3182–3197, DOI: 10.1063/1.1732447.

(68) Gurkov, T. D.; Kralchevsky, P. A. *Colloids and Surfaces* **1990**, *47*, 45–68, DOI: 10.1016/0166-6622(90)80061-8.

(69) Kralchevsky, P. A.; Eriksson, J. C.; Ljunggren, S. *Adv. Colloid Interface Sci.* **1994**, *48*, 19–59, DOI: 10.1016/0001-8686(94)80004-9.

(70) Strøm, B. A.; Simon, J. M.; Schnell, S. K., et al. *Phys. Chem. Chem. Phys.* **2017**, *19*, 9016–9027, DOI: 10.1039/c7cp00874k.

(71) Elliott, J. A. *J. Phys. Chem. B* **2020**, *124*, 10859–10878, DOI: 10.1021/acs.jpcb.0c05946.

(72) De Miguel, R.; Rubí, J. M. *J. Chem. Phys.* **2021**, *155*, 221101, DOI: 10.1063/5.0072533.

(73) Lippmann, G. *Ann. Chim. Phys.* **1875**, *5*, 494–549.

(74) Quilliet, C.; Berge, B. *Curr. Opin. Colloid Interface Sci.* **2001**, *6*, 34–39, DOI: 10.1016/S1359-0294(00)00085-6.

(75) Mugele, F.; Baret, J. C. *J. Phys. Condens. Matter* **2005**, *17*, 705–774, DOI: 10.1088/0953-8984/17/28/R01.

(76) Quinn, A.; Sedev, R.; Ralston, J. *J. Phys. Chem. B* **2005**, *109*, 6268–6275, DOI: 10.1021/jp040478f.

(77) Guangze, H.; Jianjia, M. *Contin. Mech. Thermodyn.* **2018**, *30*, 817–823, DOI: 10.1007/s00161-018-0644-8.

(78) Láng, G. G. *J. Solid State Electrochem.* **2020**, *24*, 3039–3047, DOI: 10.1007/s10008-020-04745-5.

(79) Parsegian, V.; Gingell, D. *Biophys. J.* **1972**, *12*, 1192–1204, DOI: 10.1016/S0006-3495(72)86155-1.

(80) Santos, A.; Levin, Y. *Phys. Rev. Lett.* **2019**, *122*, 248005.

(81) Denesyuk, N. A.; Hansen, J.-P. *J. Chem. Phys.* **2004**, *121*, 3613–3624, DOI: 10.1063/1.1772360.

(82) Ibagon, I.; Bier, M.; Dietrich, S. *J. Chem. Phys.* **2013**, *138*, 214703, DOI: 10.1063/1.4807760.

(83) Corkill, A. J.; Rosenhead, L. *Proc. R. Soc. London. Ser. A. Math. Phys. Sci.* **1939**, *172*, 410–431, DOI: 10.1098/rspa.1939.0111.

Chapter 3

A MODEL FOR ZWITTERIONIC POLYMERS AND THEIR CAPACITANCE APPLICATIONS

Zwitterions have been shown experimentally to enhance the dielectric constant of ionic media, owing to their large molecular dipole. Many studies since explored the enhancement of ionic conductivity with zwitterion additives as well as bulk behavior of zwitterions. Here, we examine the capacitance behavior of zwitterions between charged parallel plates using a mean-field theory. Employing only chain connectivity of a cation and anion with neutral monomers in between with mean-field electrostatics, we show that our model captures the high-dielectric behavior of zwitterions. We also predict an optimum in the capacitance of zwitterionic media as a function of chain length. To address the issue of zwitterion screening near charged surfaces, we demonstrate that zwitterions simultaneously partially screen charged walls and act as a pure dielectric that propagate the electric field far from the surface. Moreover, we show that salt solutions with zwitterionic additives outperform the energy density of both salt-only and zwitterion-only capacitors. We find that salt-only capacitors perform better at low applied potential, whereas salt capacitors with zwitterionic additives perform better at high applied potential.

This chapter includes content from our soon-to-be published article:

(1) Bruch, D.; Wang, Z.-G. A Model for Zwitterionic Polymers and Their Capacitance Applications, Under Review, 2024.

I am thankful to Dr. Alejandro Gallegos for his insight on the charge neutrality issue. I would also like to thank Dr. Chris Balzer and Sam Varner for helpful discussions on numerical methods.

3.1 Introduction

High-dielectric materials are essential to improve the performance of energy storage devices. These materials improve devices such as batteries and capacitors by increasing the dielectric constant of the ionic medium, enhancing ion conductivity and stored energy density [1–8]. Typically, in Li-ion technologies, polar organic additives are used to enhance the dielectric constant. However, these additives are flammable and weaken mechanical strength, making them unsafe for widespread use [9–12]. Polymer dielectric additives have superior mechanical strength and are less flammable, mitigating these concerns, but conventionally-used polymers such as biaxially-oriented polypropylene (BOPP) have low energy densities [2, 3]. One promising class of high-dielectric materials are zwitterions. Zwitterions are molecules with an anionic and cationic group separated by covalent bonds. This structure gives zwitterions an enormous molecular dipole moment, making them useful, nonvolatile additives that enhance the dielectric constant and ion conductivity of ionic media. Studies have shown that zwitterionic additives significantly improve ion conductivity in SCIPEs and polyelectrolyte gels [1, 4, 8]. Furthermore, a recent work on Li transport in polyzwitterionic ionic liquids (PZILs) showed PZILs form ordered subdomains that promote superionic mobility, yielding excellent Li conductivity [13]. Additionally, dielectric enhancement with added zwitterion as a function of temperature and the effect of cationic chemical substituents on the zwitterion dielectric constant were recently studied [6, 7]. The self-coacervation of semi-dilute and concentrated zwitterionic polymers has also been examined [14]. However, there are no studies on the capacitance of neat zwitterion and zwitterionic additives, nor predictions on their energy density in parallel plate geometry. In order to develop zwitterions into effective additives for energy storage devices, it is imperative to understand the capacitance and energy density zwitterions as a function of key design parameters such as added zwitterion concentration and the covalent-bond spacing between cationic and anionic substituent. Furthermore, a theoretical model of zwitterions that explores their energy storage applications would be beneficial.

On the theoretical description of zwitterions, a few models have been explored [14–18]. Ref. [16] modeled polar, explicit solvent as zwitterionic dimers using density-functional theory to capture solvent-ion structuring near a charged interface. Later, Ref. [17] developed a statistical field theory for ion-molecular solutions. They derived analytical expressions for the electrostatic potential around a test ion in a solution of zwitterion dimers using a Debye–Hučkel approximation. Further, it was shown that zwitterion dimers behave like unbound ions by screening electrostatic

interactions when the zwitterion dipole length greatly exceeds the Debye length. However, both studies were limited to zwitterionic dimers and neither explored the energy storage applications of zwitterions. In order to improve our understanding of zwitterions as additives to energy storage devices, theoretical studies are warranted.

Further clarification of zwitterion screening is needed as well. As stated previously, Ref. [17] concluded that zwitterion dimers screen test ions when the zwitterion dipole length exceeds the Debye length, [17] and Ref. [19] showed experimentally that zwitterions modify electrostatic interactions at surfaces. However, Ref. [20] showed that zwitterions layer at but do not screen charged surfaces. To properly understand zwitterion behavior in electric double-layer capacitors, this discrepancy requires clarification.

For these reasons, we study the capacitance applications of zwitterion additives in charged parallel plate geometry. In order to capture the effect of spacers between cationic and anionic substituents, we model zwitterions as a polymer—a cation and anion separated by neutral monomers. Zwitterions are not free-ions nor dipoles, but are something in between. The interplay of free-ion behavior dipole, controlled by the degree of anion-cation spacing, should manifest interesting consequences in electric double-layer structure near charged surfaces. We believe this to be an essential physics not yet explored in the context of energy storage. For example, as chain length between cation and anion increases, the net dipole of the molecule increases. However, the cations and anions should act more like unbound ions as chain length increases, screening a charged surface. It is unclear how the interplay of molecular dipole and screening as a function of chain length will affect capacitance and energy density. We explore this effect later and show that the competition between zwitterion dipole and screening yields an optimum capacitance as a function of chain length in neat zwitterions. Additionally, we address the screening issue by demonstrating zwitterions simultaneously partially screen charged surfaces and act as a dielectric medium by propagating the electric field through the bulk. Further, we show that pure-dipole and pure free-ion regimes can be observed depending on the anion-cation spacing.

The rest of the paper is organized as follows: first, we develop a mean-field theory for zwitterions in a salt solution between charged plates, taking into account discrete chain connectivity, incompressibility, and electrostatics. Second, we briefly describe the numerical scheme used to solve the mean-field equations. In our numerical scheme, we adopted an algorithm not yet used in the field-theory community

that evaluates discrete chain propagators with FFT to arbitrary algebraic accuracy, as opposed to the standard $\mathcal{O}(\Delta z^2)$ implementation [21]. Next, we examine the screening behavior of zwitterions as a function of chain length and statistical segment length. We also provide a brief analytical calculation of the dielectric constant of a zwitterionic melt under small applied potential. Then, we show the capacitance of a neat zwitterion exhibits a maximum as a function of chain length and demonstrate this maximum arises from a competition of bulk and surface effects. We conclude our work by showing that zwitterionic additives outperform salt-only and zwitterion-only solutions, and they enhance the energy density of traditional electric double-layer capacitors by up to 8.2% at high applied potential relative to salt-only solutions. We also map the stored energy density of a zwitterion-salt solution capacitor as a function of zwitterion concentration and zwitterion chain length. We believe these predictions will be helpful for the design of energy storage devices with zwitterionic additives.

3.2 Model

We develop our model using a standard field-theoretic approach, starting with the Hamiltonian for an incompressible solution of zwitterionic polymers in neutral monomeric solvent with added salt between parallel electrodes [22]. Our goal is to obtain the grand canonical partition function, from which we can obtain mean-field equations using a saddle-point approximation.

Consider a system of of n zwitterionic polymers, n_+ free salt cations, n_- free salt anions, and n_s neutral solvent molecules contained in a volume V. The zwitterionic polymer consists of $N+1$ beads with a positively charged bead on one end, and a negatively charged bead on the other, separated by $N-1$ neutral beads. The beads are connected through a harmonic-spring bonding potential. Both charged beads have a valency $Z = 1$, so the zwitterion satisfies electroneutrality by construct. Since we are not concerned with valency effects in this chapter, we assume the added salt to have valency $Z = 1$. We assign the zwitterion positive end as bead $j = 0$ and the negative end as bead $j = N$ without loss of generality. The solution is incompressible and between anti-symmetric parallel electrodes with applied potentials $+V$ and $-V$. A diagram of the system is depicted in Fig. 3.1. We note that several recent studies deal with polyzwitterions–zwitterionic systems having oppositely charged groups on each monomer [13, 23, 24]. However, since we are interested in clarifying the screening behavior of zwitterions and examining their capacitance, we choose the model where the charges are on the two ends of the polymer as it is more

representative of the zwitterions studied in the screening experiments of Ref. [20] and the dielectric measurements of Ref. [7].

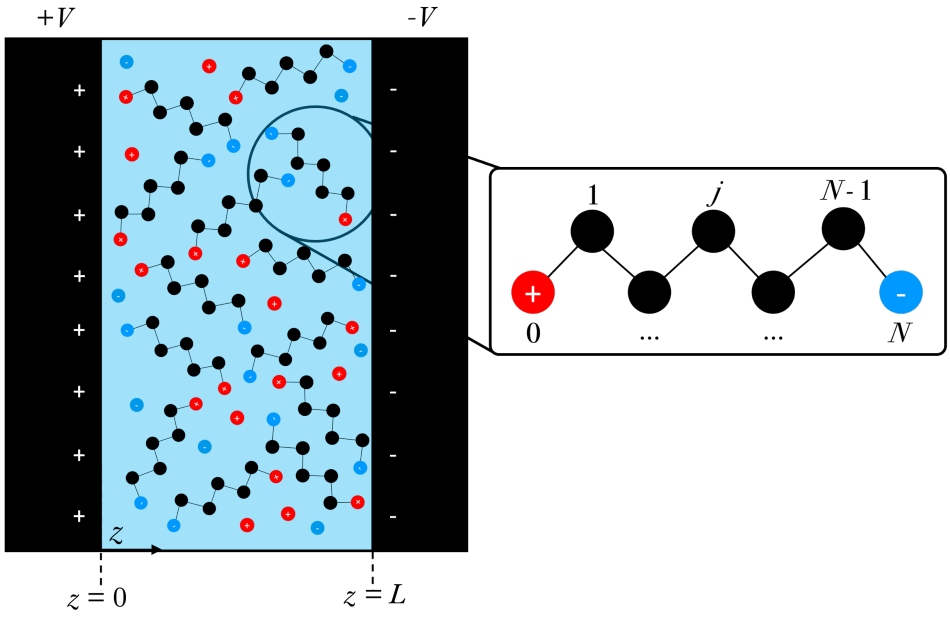

Figure 3.1: A solution of zwitterionic polymers of chain length N and added salt in neutral, monomeric solvent. The total solution density is ρ_0. The zwitterion and added salt have bulk concentrations $c_{\mathrm{B,zw}}$ and $c_{\mathrm{B,f}}$, respectively. The solution is between two charged plates located at $z = 0$ and $z = L$ with applied potentials $+V$ and $-V$, respectively.

Our system Hamiltonian consists of contributions from bead connectivity and electrostatic contributions from all charged species, as shown in Eq. (3.1).

$$\beta H = \sum_{\alpha=1}^{n} \sum_{j=1}^{N} \frac{3}{2b^2} (\mathbf{r}_{\alpha,j} - \mathbf{r}_{\alpha,j-1})^2 + \frac{l_{\mathrm{B}}}{2} \int \mathrm{d}\mathbf{r} \int \mathrm{d}\mathbf{r}' \frac{\hat{\rho}_e(\mathbf{r}) \hat{\rho}_e(\mathbf{r}')}{|\mathbf{r} - \mathbf{r}'|} \tag{3.1}$$

where the first term is the entropic spring energy for n chains each with $N+1$ beads, $\beta = 1/kT$ and k is the Boltzmann constant, and b is the statistical segment length. We use the terms *monomer* and *bead* interchangeably, and we adopt this convention for the remainder of the article. The second term is the total Coulomb energy where l_{B} is the Bjerrum length defined as $l_{\mathrm{B}} = \beta e^2 / 4\pi\epsilon\varepsilon_0$. Here, e is the elementary charge, ε_0 is the dielectric permittivity of vacuum, and ϵ is the dielectric constant of the medium, assumed to be spatially uniform. The microscopic charge density operator $\hat{\rho}_{\mathrm{e}}(\mathbf{r})$ is defined as

$$e\hat{\rho}_{\mathrm{e}}(\mathbf{r}) = e\left[\rho_{\mathrm{ex}}(\mathbf{r}) + \hat{c}_{+}(\mathbf{r}) - \hat{c}_{-}(\mathbf{r})\right] \tag{3.2}$$

where $\rho_{\mathrm{ex}}(\mathbf{r})$ is an externally imposed charge distribution, i.e., the parallel electrodes. Note that, in our definition of charge densities above, we explicitly factored out the charge e, so all charge densities have units length^{-3}. The positive and negative ion density operators $\hat{c}_{\pm}(\mathbf{r})$ are given by

$$\hat{c}_{+}(\mathbf{r}) = \hat{c}_{\mathrm{zw},+}(\mathbf{r}) + \hat{c}_{\mathrm{f},+}(\mathbf{r}) = \sum_{\alpha=1}^{n}\delta(\mathbf{r}-\mathbf{r}_{\alpha,0}) + \sum_{j=1}^{n_{+}}\delta(\mathbf{r}-\mathbf{r}_{j}^{+}) \tag{3.3a}$$

$$\hat{c}_{-}(\mathbf{r}) = \hat{c}_{\mathrm{zw},-}(\mathbf{r}) + \hat{c}_{\mathrm{f},-}(\mathbf{r}) = \sum_{\alpha=1}^{n}\delta(\mathbf{r}-\mathbf{r}_{\alpha,N}) + \sum_{j=1}^{n_{-}}\delta(\mathbf{r}-\mathbf{r}_{j}^{-}) \tag{3.3b}$$

where the first and second terms correspond to the zwitterion and free-salt contributions, respectively. Note that in our definitions of $\hat{c}_{\mathrm{zw},\pm}(\mathbf{r})$, the positive and negative ions are the 0^{th} and N^{th} bead, respectively, so their bead coordinates are $\mathbf{r}_{\alpha,0}$ and $\mathbf{r}_{\alpha,N}$.

The grand canonical partition function is given by

$$\begin{aligned}\Xi = \sum_{n=0}^{\infty}\sum_{n_{+}=0}^{\infty}\sum_{n_{-}=0}^{\infty}\sum_{n_{s}=0}^{\infty} Z_{\mathrm{C}}(n,n_{+},n_{-},n_{s}) \\ \times \exp\left[\beta\mu_{\mathrm{zw}}n + \beta\mu_{+}n_{+} + \beta\mu_{-}n_{-} + \beta\mu_{s}n_{s}\right]\end{aligned} \tag{3.4}$$

where μ_{γ} is the chemical potential of species γ and Z_{C} is the canonical partition function, written using the Boltzmann weight of the Hamiltonian

$$\begin{aligned}Z_{\mathrm{C}} =& \frac{1}{n!n_{+}!n_{-}!n_{s}!\nu^{n(N+1)}\nu_{+}^{n_{+}}\nu_{-}^{n_{-}}\nu_{s}^{n_{s}}} \\ &\times \prod_{\alpha=1}^{n}\prod_{k=1}^{n_{+}}\prod_{l=1}^{n_{-}}\prod_{m=1}^{n_{s}}\int \mathrm{d}\mathbf{r}_{\alpha}^{N+1}\int \mathrm{d}\mathbf{r}_{k}^{+}\int \mathrm{d}\mathbf{r}_{l}^{-}\int \mathrm{d}\mathbf{r}_{m}^{s} \\ &\times \exp\left[-\sum_{\alpha=1}^{n}\sum_{j=1}^{N}\frac{3}{2b^{2}}(\mathbf{r}_{\alpha,j}-\mathbf{r}_{\alpha,j-1})^{2}\right] \\ &\times \exp\left[-\frac{l_{\mathrm{B}}}{2}\int \mathrm{d}\mathbf{r}\int \mathrm{d}\mathbf{r}'\,\frac{\hat{\rho}_{e}(\mathbf{r})\hat{\rho}_{e}(\mathbf{r}')}{|\mathbf{r}-\mathbf{r}'|}\right] \\ &\times \delta[\hat{\rho}(\mathbf{r}) + \hat{c}_{\mathrm{f},+}(\mathbf{r}) + \hat{c}_{\mathrm{f},-}(\mathbf{r}) + \hat{c}_{s}(\mathbf{r}) - \rho_{0}]\end{aligned} \tag{3.5}$$

where ν_γ is the characteristic volume of species γ. Since we are only concerned with extracting the essential physics of our model, we assume neutral and charged monomers in the zwitterion have the same characteristic volume. We note that some authors use the thermal wavelength cubed as the volume scale. The choice of volume scale is inconsequential—it merely results in a concentration-independent shift in the chemical potential [25]. Here, we use the shorthand notation $\int \mathrm{d}\mathbf{r}_\alpha^{N+1}$ to denote the $N+1$ volume integrals over the individual monomer coordinates for chain α. The delta functional at the end of Eq. (3.5) enforces local incompressibility at all points in space, where ρ_0 is the density of the solution, $\hat{\rho}(\mathbf{r})$ is the microscopic total monomer density defined as

$$\hat{\rho}(\mathbf{r}) = \sum_{\alpha=1}^{n} \sum_{j=0}^{N} \delta(\mathbf{r} - \mathbf{r}_{\alpha,j}) \tag{3.6}$$

and $\hat{c}_s$ is the microscopic total solvent density given by

$$\hat{c}_s(\mathbf{r}) = \sum_{i=1}^{n_s} \delta(\mathbf{r} - \mathbf{r}_i^s). \tag{3.7}$$

Next, we use the Hubbard–Stratonovich (HS) transformation to decouple the quadratic interactions of the electrostatic term in Eq. (3.5) at the expense of a new coupling to the field variable ξ. Upon using the HS transformation, applying the definitions of microscopic density operators, and redefining $\psi = i\xi$ and $\eta = i\eta$ (since we anticipate the saddle-point lies purely on the imaginary axis) we arrive at the final following form of the grand canonical partition function

$$\Xi = \frac{1}{Z} \int \mathscr{D}\eta \int \mathscr{D}\psi \, \exp\{-L[\eta(\mathbf{r}), \psi(\mathbf{r})]\} \tag{3.8a}$$

$$\begin{aligned} L[\eta(\mathbf{r}), \psi(\mathbf{r})] = &-\lambda_{\mathrm{zw}} Q - \lambda_+ q_+ - \lambda_- q_- - \lambda_s q_s \\ &+ \int \mathrm{d}\mathbf{r} \left\{ - \frac{1}{8\pi l_{\mathrm{B}}} \left[\nabla\psi(\mathbf{r})\right]^2 + \rho_{\mathrm{ex}}\psi + \eta(\mathbf{r})\rho_0 \right\} \end{aligned} \tag{3.8b}$$

where we assumed $\nu = b^3$ for the zwitterion, $\lambda_{\mathrm{zw}} = \left(\frac{2\pi}{3}\right)^{3N/2} e^{\beta\mu_{\mathrm{zw}}}$, $\lambda_\pm = e^{\beta\mu_\pm}$, and $\lambda_s = e^{\beta\mu_s}$ are the fugacities of the zwitterionic polymer, positive and negative free ions, and solvent, respectively. Additionally, $q_\pm = \frac{1}{\nu_\pm} \int \mathrm{d}\mathbf{r} \, \exp\left[\eta(\mathbf{r}) \mp \psi(\mathbf{r})\right]$ and $q_s = \frac{1}{\nu_s} \int \mathrm{d}\mathbf{r} \, \exp\left[\eta(\mathbf{r})\right]$ are the single-particles partition function for the positive

and negative free ions and solvent, respectively, and Q is the single-chain partition function, given by

$$Q[\eta,\psi] = \frac{1}{b^3}\int \mathrm{d}\mathbf{r}\, q(\mathbf{r}, N; [\eta,\psi]) \tag{3.9}$$

where $q(\mathbf{r}, N; [\eta,\psi])$ is the chain propagator. Due to the asymmetry of the zwitterion, there are two chain propagators: $q(\mathbf{r}, N; [\eta,\psi])$, which propagates from the positive to negative end, and $q^\dagger(\mathbf{r}, N; [\eta,\psi])$, which propagates from the negative to positive end. The chain propagators are defined as

$$q(\mathbf{r}, N; [\eta,\psi]) = \exp\left[\eta(\mathbf{r}) - \psi(\mathbf{r})\right] \tag{3.10a}$$

$$q(\mathbf{r}, j+1; [\eta,\psi]) = \exp\left[\eta(\mathbf{r})\right]\int \mathrm{d}\mathbf{r}'\, \Phi(\mathbf{r}-\mathbf{r}')q(\mathbf{r}', j; [\eta,\psi]) \quad \text{for } j = 0, 1, ..., N-2 \tag{3.10b}$$

$$q(\mathbf{r}, N; [\eta,\psi]) = \exp\left[\eta(\mathbf{r}) + \psi(\mathbf{r})\right]\int \mathrm{d}\mathbf{r}'\, \Phi(\mathbf{r}-\mathbf{r}')q(\mathbf{r}', N-1; [\eta,\psi]) \tag{3.10c}$$

and

$$q^\dagger(\mathbf{r}, N; [\eta,\psi]) = \exp\left[\eta(\mathbf{r}) + \psi(\mathbf{r})\right] \tag{3.11a}$$

$$q^\dagger(\mathbf{r}, j+1; [\eta,\psi]) = \exp\left[\eta(\mathbf{r})\right]\int \mathrm{d}\mathbf{r}'\, \Phi(\mathbf{r}-\mathbf{r}')q^\dagger(\mathbf{r}', j; [\eta,\psi]) \quad \text{for } j = 0, 1, ..., N-2 \tag{3.11b}$$

$$q^\dagger(\mathbf{r}, N; [\eta,\psi]) = \exp\left[\eta(\mathbf{r}) - \psi(\mathbf{r})\right]\int \mathrm{d}\mathbf{r}'\, \Phi(\mathbf{r}-\mathbf{r}')q^\dagger(\mathbf{r}', N-1; [\eta,\psi]) \tag{3.11c}$$

where $\Phi(\mathbf{r}-\mathbf{r}')$ is the normalized bond transition probability

$$\Phi(\mathbf{r}) = \left(\frac{3}{2\pi b^2}\right)^{3/2}\exp\left(-\frac{3}{2b^2}\mathbf{r}^2\right). \tag{3.12}$$

From here, we apply the saddle-point approximation $\delta L/\delta\psi = 0$ and $\delta L/\delta\eta = 0$ to obtain a set of self-consistent, mean-field equations that describe the incompressible zwitterionic polymer solution. The saddle-point condition in ψ yields the Poisson equation

$$\nabla^2\psi = -4\pi l_{\mathrm{B}}(\rho_{\mathrm{ex}} + c_{\mathrm{zw},+} + c_{\mathrm{f},+} - c_{\mathrm{zw},-} - c_{\mathrm{f},-}) \tag{3.13}$$

where the ion concentrations are obtained from the integrand of chemical potential derivatives of the grand free energy, given by

$$c_{\mathrm{f},\pm} = c_{\mathrm{B,f}} \exp\left[\eta(\mathbf{r}) \mp \psi(\mathbf{r})\right] \tag{3.14a}$$

$$c_{\mathrm{zw},+} = c_{\mathrm{B,zw}}\, q^{\dagger}(\mathbf{r}, N) \tag{3.14b}$$

$$c_{\mathrm{zw},-} = c_{\mathrm{B,zw}}\, q(\mathbf{r}, N) \tag{3.14c}$$

with q as the forward chain propagator (positive to negative bead) and $q^{\dagger}$ as the backward chain propagator (negative to positive bead). Note that the factors $c_{\mathrm{B,f}}$ and $c_{\mathrm{B,zw}}$ came from setting the reference potential in the bulk to be $\psi = 0$, which gave relationships between the fugacities and bulk concentrations.

Similarly, the saddle-point condition in η yields

$$\rho_0 = c_{\mathrm{zw},+} + c_{\mathrm{f},+} + c_{\mathrm{zw},-} + c_{\mathrm{f},-} + c_s + c_{\mathrm{B,zw}} \sum_{j=1}^{N-1} q(\mathbf{r}, N-j) q^{\dagger}(\mathbf{r}, j) \tag{3.15}$$

where $c_s = c_{\mathrm{B,s}} \exp\left[\eta(\mathbf{r})\right]$, and $c_{\mathrm{B,s}}$ is the bulk solvent density, related to the other bulk densities through $c_{\mathrm{B,s}} = \rho_0 - c_{\mathrm{B,zw}}(N+1) - 2c_{\mathrm{B,f}}$. Eq. (3.15) is simply a statement of local incompressibility of all species in solution.

3.3 Numerical Methods

Eqs. (3.13)–(3.15) form the set of self-consistent equations of our system at a mean-field level. However, they are unable to be solved analytically. Solving these equations numerically requires two major steps: field updating and chain propagation. We update the η and ψ fields using the well-known Anderson acceleration algorithm, giving rapid saddle-point convergence [26, 27]. Evaluating the chain propagator requires numerically integrating a series of $N + 1$ convolutions. It is already known that these convolutions can be integrated on a uniform grid of M grid points using a cyclic summation on a doubled computational domain with $\mathcal{O}(M \log M)$ speed using fast Fourier transforms (FFTs) [28, 29]. However,

this method amounts to a trapezoidal rule approximation that has low accuracy of $\mathcal{O}(\Delta z^2)$. A method that achieves higher accuracy is desirable, as it would save computational time by reducing the number of grid points. As far as we know, there have been no methods implemented for discrete Gaussian-chains in non-periodic, finite domains that achieve a higher accuracy [29]. For this reason, we implemented the algorithm developed by Qiang [21], which gives arbitrary algebraic accuracy for evaluating convolutions on uniform grids in non-periodic, finite domains.

Consider a general form for the discrete-chain propagator of the $k+1^{\text{th}}$ monomer

$$q(z, k+1) = \exp[-w(z)] \int \mathrm{d}z' \, \Phi(z - z') q(z', k) \tag{3.16}$$

where $w(z)$ is the field weight for the monomer, and Φ is the bonding potential. Qiang's algorithm works by embedding the discretized convolution with a higher-order quadrature rule. For example, using Simpson's rule, Eq. (3.16) is discretized as

$$q(z_i, k+1) = \frac{1}{3}\Delta z \exp[-w(z_i)] \sum_{j=0}^{M+1} \Phi(z_i - z_j) \bar{q}(z_j, k) \tag{3.17}$$

where $\bar{q}$ contains the embedding of Simpson's quadrature rule, given by

$$\bar{q}(z_j, k) = \begin{cases} q(z_j, k), & j = 1 \\ 4q(z_j, k), & j = 2l \\ 2q(z_j, k), & j = 2l - 1 \\ q(z_j, k), & j = M. \end{cases} \tag{3.18}$$

In order to use FFT, Eq. (3.17) can be rewritten as a cyclic summation on a doubled computational grid according to Hockney [28]. Then, the cyclic summation can be calculated using FFT, and the integral in Eq. (3.16) is given in the original domain of the cyclic summation. These details are thoroughly described in Refs. [28] and [21], and we defer the reader to these references for implementation.

With Simpson's quadrature rule, this algorithm achieves $\mathcal{O}(\Delta z^4)$ accuracy. Moreover, higher-order accuracy can be obtained with higher-order quadrature rules (e.g., Boole's rule), up to arbitrarily high algebraic accuracy with a suitable quadrature rule. In this chapter, we use Qiang's algorithm with Simpson's quadrature

rule, allowing us to evaluate discrete-chain propagators with $\mathcal{O}(\Delta z^4)$ accuracy and $\mathcal{O}(NM \log M)$ speed.

3.4 Screening

In this section, we address the previously-discussed discrepancy on zwitterion screening by examining zwitterion density and potential profiles for various chain lengths N and statistical segment lengths b. Here, we focus on a zwitterionic polymer melt, where a melt is the limiting case of Eqs. (3.13)–(3.15) for no added salt ($c_{\mathrm{B,f}} = 0$) nor solvent ($c_{\mathrm{B,s}} = 0$; consequently, the bulk ion concentration from zwitterions is given by $c_{\mathrm{B,zw}} = \rho_0/(N+1)$). Although we consider a melt in this section, we explore zwitterion solutions in later sections.

We start by examining the density and potential profiles for a zwitterionic polymer melt with chain length $N = 10$ between two anti-symmetric charged plates with spacing $L = 5$ nm and potential drop $\Delta V = 2.0\ kT/e$ in Fig. 3.2a. Here, the left and right plates are positively and negatively charged, respectively. From Fig. 3.2a, we see the anion and cation accumulate at the positively and negatively charged plates, respectively. Although cations are depleted at the left plate, their density has a maximum just before the anion surface layer due to the anion-cation connectivity. The same is true for the right plate except with the charges reversed. The neutral monomer enriches just outside of the electric double-layer due to connectivity with the adsorbed ion as well as to satisfy the incompressibility constraint. All species reach bulk concentrations sufficiently far from the plates. Since a zwitterion is neither free ion nor pure dipole, we expect it to behave as a free ion on length scales smaller than the end-to-end distance and as a dipole on length scales larger than the end-to-end distance. This behavior is verified by the electrostatic potential profile in Fig. 3.2b. From Fig. 3.2b, the electrostatic potential partially decays near the surfaces, similarly to screening by unbound ions in traditional electric double-layer systems. This result suggests zwitterions can at least partially screen the electric field from the electrodes. Far from the surface, the electrostatic potential propagates linearly through the bulk region of the melt. In other words, the bulk of the melt is propagating a constant electric field, which is analogous to parallel plate capacitors with a static dielectric medium. Therefore, the zwitterion acts as a dielectric medium in the bulk.

Further, we examine to the two-body density functions between the zwitterion cation and anion. For a dimer, the two-body densities are given by

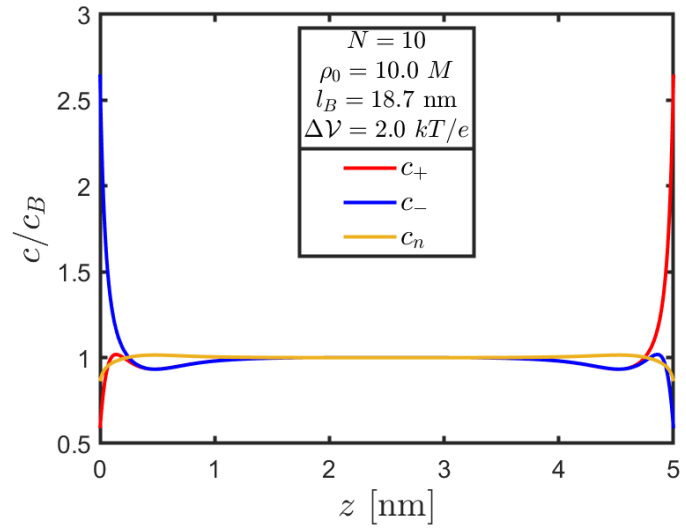

(a)

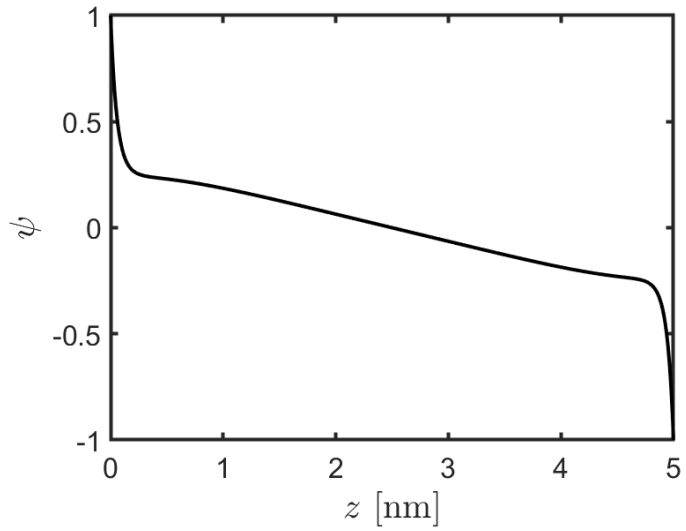

(b)

Figure 3.2: Density and electrostatic potential profiles for an incompressible zwitterionic polymer melt. (a) Positive (red), negative (blue), and neutral (yellow) monomer density profiles and (b) electrostatic potential for an incompressible zwitterionic polymer melt as a function of distance from parallel electrodes. The left and right plate are positively and negatively charged, respectively, with a potential drop of $2.0\,kT/e$ and plate separation $L = 5$ nm. The polymers have $N = 10$ bonds and statistical segment length $b = 0.5$ nm, and the melt has an incompressible density $\rho_0 = 10.0\,M$ and a Bjerrum length $l_\mathrm{B} = 18.7$ nm. All densities are scaled by their bulk value.

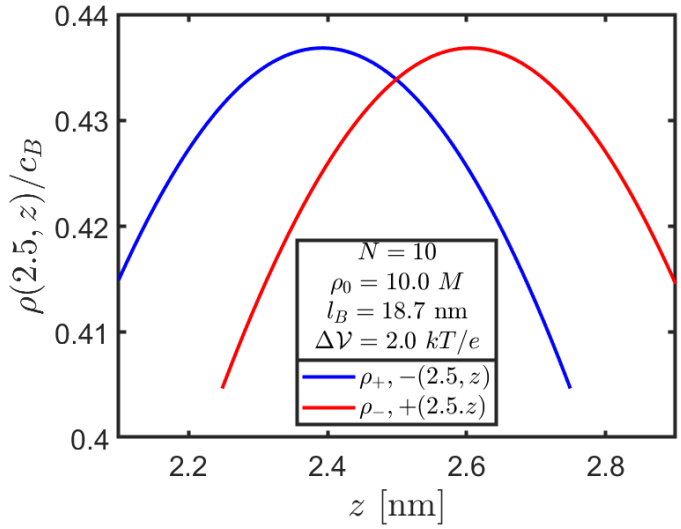

Figure 3.3: Two-body density profiles for an incompressible zwitterionic polymer melt between two electrodes with a potential drop of $2.0\,kT/e$ and plate separation $L = 5$ nm. The polymers have $N = 10$ bonds and statistical segment length $b = 0.5$ nm, and the melt has an incompressible density $\rho_0 = 10.0\,M$ and a Bjerrum length $l_\mathrm{B} = 18.7$ nm. All densities are scaled by their bulk value. The two-body density of the negative ion given a positive ion fixed at $z = 2.5$ nm is blue, and that of the positive ion given a negative ion fixed at $z = 2.5$ nm is red.

$$\rho_{+,-}(\mathbf{r},\mathbf{r}') = \exp\left[\eta(\mathbf{r}) - \psi(\mathbf{r})\right]\Phi(\mathbf{r}-\mathbf{r}')\exp\left[\eta(\mathbf{r}') + \psi(\mathbf{r}')\right] \tag{3.19a}$$

$$\rho_{-,+}(\mathbf{r},\mathbf{r}') = \exp\left[\eta(\mathbf{r}) + \psi(\mathbf{r})\right]\Phi(\mathbf{r}-\mathbf{r}')\exp\left[\eta(\mathbf{r}') - \psi(\mathbf{r}')\right] \tag{3.19b}$$

where $\rho_{+,-}(\mathbf{r},\mathbf{r}')$ is the density of the negative ion given a positive ion at position $\mathbf{r}$, and $\rho_{-,+}(\mathbf{r},\mathbf{r}')$ is the reverse. For chains larger than a dimer, we constrain the propagators to account for the explicit positions of the positive and negative beads. Both two-body density functions are plotted in Fig. 3.3 for a zwitterionic polymer with $N = 10$ bonds, with the tagged ion located at the center (bulk) between the plates. From Fig. 3.3, we see that the two-body densities are asymmetric about the center point—that is, the dipole of the zwitterionic polymers have a net alignment with the electric field. This dipole alignment in the bulk is similar to the behavior of a static dielectric medium, and the alignment allows the zwitterion to propagate the constant electric field. Therefore, for our model, we have shown that zwitterions simultaneously partially screen and propagate electric fields—that is, they exhibit partial unbound-ion and partial dipole characteristics. Ref. [17] showed this for zwitterion dimers ($N = 1$) around a test ion, and here we showed it

for zwitterionic polymers with charged electrodes. Now, we examine the conditions where zwitterionic polymers behave as pure unbound ions or pure dipoles.

To understand the screening behavior of zwitterions, we isolate the effects of the statistical segment length b and the polymer chain length N. We examine the electrostatic potential profiles of a zwitterion dimer ($N = 1$) melt for various b in Fig. 3.4a at a nominal Debye length of $l_D = 0.027$ nm. From Fig. 3.4a, we see the zwitterion dimer does little to no screening for sufficiently small b of $b = 0.1$ nm relative to the Debye length, exhibiting nearly pure dipole character. For moderate b, the dimer incompletely screens—a mix of dipole and unbound-ion character. At a sufficiently large b of $b = 10$ nm, the dimer completely screens the electric field, acting as unbound ions. In the inset plot of Fig. 3.4a, we see from the plot of $\log \psi$ versus distance that the inverse slope close to the surface coincides with the Debye screening length only for large b. Moreover, the screening length coincides with the Debye length only close to the surface. We argue that after sufficient screening of the electric field close to the surface, the bonding potential of the zwitterion dimer dominates, altering the screening length. However, for infinite b, the screening length should persist as the Debye screening length indefinitely.

Turning to the chain length N, the electrostatic potential profiles of a zwitterionic polymer melt for various N at fixed $b = 0.5$ nm are shown in Fig. 3.4b. Note that since the bulk ion concentration for a zwitterionic polymer melt is $c_{B,zw} = \rho_0/(N + 1)$), increasing the chain length dilutes the ions and changes the Debye length. From Fig. 3.4b, we see that the zwitterion screens more as the chain length increases. Moreover, from the inset plot of Fig. 3.4b, we see that the screening length coincides more with the Debye length as the chain length increases. Thus, the zwitterion ions gains more unbound-ion characteristic as the chain length increases, and we expect the zwitterion ions would behave as purely unbound ions in the infinite chain limit. Additionally, the screening length coincides with the Debye screening length only close to the surface for the same reasons discussed for the statistical segment length. Aside from the dilution effect, changing N is equivalent to changing b^2.

Therefore, we have shown that with our model we recover regimes of no screening (pure dipole), partial screening, and complete screening (unbound ion), depending on chain length and statistical segment length. This is in agreement with the idea that as the dipole length (distance between ions) increases, the charged ends become less bound and screen similarly to Debye–Hückel electrolytes, as pointed out in Ref.

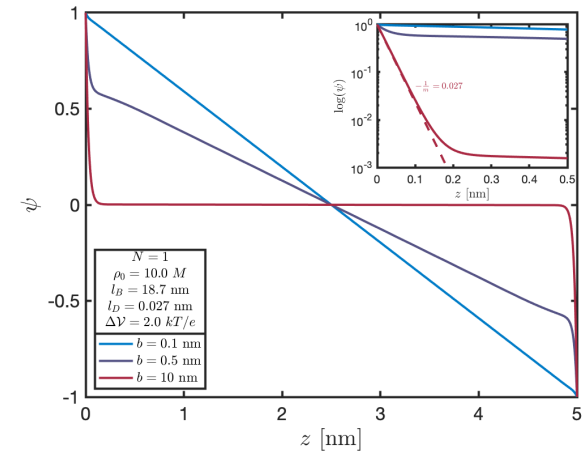

(a)

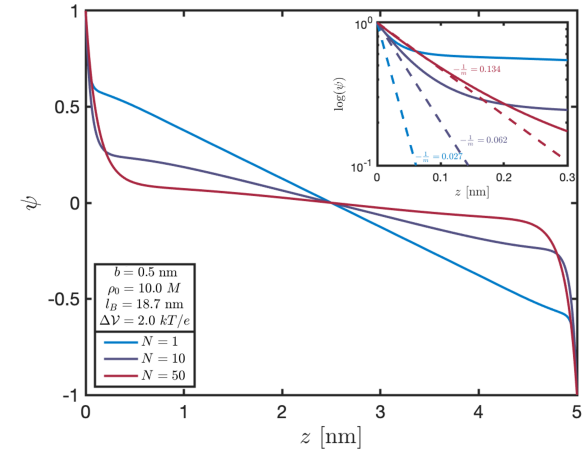

(b)

Figure 3.4: Electrostatic potential profiles for an incompressible zwitterionic polymer melt as a function of distance between parallel electrodes for various statistical segment lengths b and chain lengths N. The left and right plates are positively and negatively charged, respectively, with a potential drop of $2.0\,kT/e$ and plate separation $L = 5$ nm. (a) $b = 0.1$ nm (blue), $b = 0.5$ nm (purple), and $b = 10$ nm (red). The zwitterion is a dimer $N = 1$. (b) $N = 1$ (blue), $N = 10$ (purple), and $N = 50$ (red). The zwitterionic polymer has statistical segment length $b = 0.5$ nm. Insets: Semilog y of the electrostatic potential vs. distance from plate, where m is the slope of the line passing through the curve close to the surface.

[30]. This effect was later substantiated in Ref. [31] for a microscopic model of dipolar molecules with point-like charged groups. The results for statistical segment length are in agreement with the conclusions in Ref. [17] for zwitterion dimers near a test ion at the Debye–Hückel level, although we demonstrated this with the presence of a charged surface. In light of these conclusions, we can now clarify the

discrepancy on zwitterion screening between Ref. [17], Ref. [19], and Ref. [20]. Ref. [17] concluded that zwitterion dimers screen test ions when the zwitterion dipole length exceeds the Debye length, and Ref. [19] showed experimentally that zwitterions modify electrostatic interactions at surfaces, which suggests screening effects. However, Ref. [20] showed that glycine zwitterions in water layer at but do not screen charged surfaces. The reason for this observation is the statistical segment length of their zwitterion, glycine, is about 3 Å [32, 33], which is much smaller than their reported screening lengths of $\sim$ 46–48 nm for their systems of only glycine in water. Consequently, the zwitterions are expected to act as point dipoles. We believe that if a system had been chosen at Debye length much smaller than the zwitterion statistical segment length, one would observe screening.

3.5 Dielectric Constant

Here, we provide a brief analytical calculation of the dielectric constant for a zwitterionic polymer melt for small applied potential. By twice integrating the Poisson equation (Eq. (3.13)), the following expression for the surface charge is obtained [34]

$$\sigma = \frac{\varepsilon_0 \epsilon \Delta V}{\beta e^2 L} - \frac{1}{L} \int_0^L \mathrm{d}z'\, z' \left[c_+(z') - c_-(z') \right] \tag{3.20}$$

where σ has units nm^{-2}, ΔV is nondimensional, and the second term is the polarization of the medium. By applying the definition of differential capacitance $C = \beta e^2 \partial Q / \partial \Delta V$ (Q = σ A), and comparing with the capacitance of parallel plates $C = \varepsilon_0 \epsilon A / L$, a general expression for the "effective" dielectric constant of a polarizable medium between charged parallel plates can be derived, given by

$$\epsilon_{\mathrm{eff}} = \epsilon - \frac{\beta e^2}{\varepsilon_0} \frac{\partial}{\partial \Delta V} \int_0^L \mathrm{d}z'\, z' \left[c_+(z') - c_-(z') \right] . \tag{3.21}$$

We assume the applied potential ΔV is sufficiently small to evaluate the integrand $c_+ - c_-$ in Eq. (3.21) by expanding the propagator for small electrostatic potential ψ to first order. Additionally, note that the incompressibility field $\eta \sim \psi^2$ by virtue of incompressibility, and thus can be neglected to first order. Performing this expansion to first order yields

$$c_+ - c_- = \frac{2\rho_0}{N+1} \int_0^L \mathrm{d}z'\, \Phi_N(z - z') \left[\psi(z') - \psi(z) \right] \tag{3.22}$$

where Φ_N is the full chain end-to-end bond transition probability

$$\Phi_N(z) = \left(\frac{3}{2\pi N b^2}\right)^{1/2} \exp\left(-\frac{3}{2Nb^2}z^2\right). \tag{3.23}$$

To evaluate the integrals in Eqs. (3.22) and (3.21), we note that, as discussed from Fig. 3.4, the electrostatic potential is linear when $N^{1/2}b \ll l_\mathrm{d}$. Under this assumption, the electrostatic potential is given by $\psi(z) = -\frac{\Delta V}{L}\left(z - \frac{L}{2}\right)$. Upon substituting this expression into Eq. (3.22), the equation evaluates to

$$\begin{aligned} c_+(z) - c_-(z) = \frac{\rho_0}{N+1}\left(\frac{2Nb^2}{3\pi}\right)^{1/2}\left(\frac{\Delta V}{L}\right) \\ \times\left\{\exp\left[-\frac{3}{2Nb^2}z^2\right] - \exp\left[-\frac{3}{2Nb^2}(z-L)^2\right]\right\} \end{aligned} \tag{3.24}$$

where the Gaussian terms originate from translational entropy loss of the zwitterion near the walls. Upon substituting Eq. (3.24) in Eq. (3.21), taking the limit $N^{1/2}b \ll L$ (large plate separation) since we are not interested in confinement effects, we arrive at the result for the effective dielectric constant

$$\epsilon_\mathrm{eff} = \epsilon + \frac{\beta e^2 \rho_0}{3\varepsilon_0}\frac{Nb^2}{N+1}. \tag{3.25}$$

Note that this result for the dielectric constant holds in the bulk region outside the limit $N^{1/2}b \ll l_\mathrm{d}$, which we demonstrate later. This result for ϵ_eff is simply the Debye result for dipolar molecules, and it matches the expression for the dimer limit ($N = 1$) derived by Ref. [17]. Similar behavior was shown for long dipoles in Ref. [35]. Most notably, the effective dielectric constant scales as $\frac{N}{N+1}$. The dipole strength grows as N, but the ions are simultaneously diluted in a melt as $\frac{1}{N+1}$. Therefore, the bulk dielectric constant will plateau for large N. Lastly, a straightforward substitution for ρ_0, N, and b into Eq. (3.25) using the same values from the previous section recovers effective dielectric constants on the order of hundreds, in agreement with experimental observations from Ref. [6].

3.6 Capacitance

Because of the unusual screening behavior of zwitterions, we expect interesting behavior in their capacitance. In this section, we examine the differential capacitance

of a zwitterionic polymer melt as a function of chain length (covalent bond spacing) and applied potential, given by $C/A = \partial\sigma/\partial\Delta V$. We first show the capacitance versus applied potential undergoes a bell-to-camel transition as chain length increases. Then, we find that the capacitance exhibits a maximum as a function of chain length. We further demonstrate that this maximum arises from a competition of bulk and surface effects.

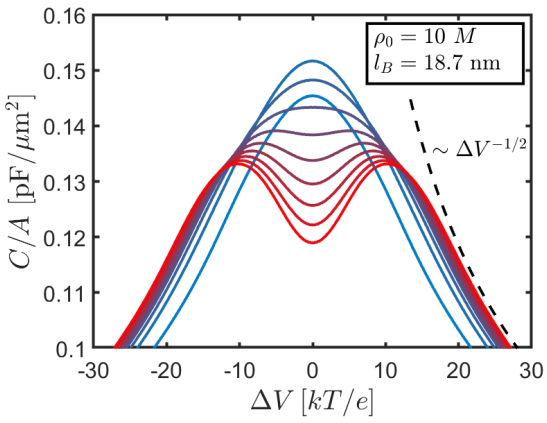

(a)

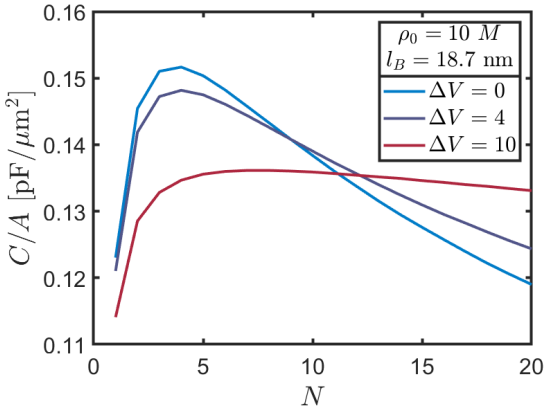

(b)

Figure 3.5: Differential capacitance per unit area for an incompressible zwitterionic polymer melt. The left and right plate are positively and negatively charged, respectively, with plate separation $L = 10$ nm. The polymer melt has statistical segment length $b = 0.5$ nm, incompressible density $\rho_0 = 10.0\,M$, and Bjerrum length $l_B = 18.7$ nm. (a) Differential capacitance as a function of applied voltage for various N increasing from 2 (blue) to 20 (red) bonds in steps of 2 through a color gradient. The dashed, black line denotes $\Delta V^{-1/2}$ scaling, characteristic of electric-double layer saturation. (b) Differential capacitance as a function of applied N for various applied voltages.

Fig. 3.5a shows the capacitance of a zwitterionic polymer melt as a function of

applied voltage for increasing chain lengths from $N = 2$ to $N = 20$ (blue to red) in steps of 2 through a color gradient. From Fig. 3.5a, the curves exhibit a bell-to-camel transition as chain length increases [36], simply due to the ion concentration diluting as $\frac{1}{N+1}$ as chain length increases. Additionally, there are contributions from chain stretching. At low applied voltage, the longer chains readily stretch in the applied field with increasing voltage, increasing their dipole moment and thus increasing the capacitance, whereas smaller chain cannot stretch appreciably and the capacitance only decreases. At high applied voltage, the electric double layer saturates so the capacitance decreases for both small and large chains. Additionally, the capacitance for all chain lengths scales as $\Delta V^{-1/2}$ at high applied potential due to electric-double layer saturation, denoted by the dashed, black line. Moreover, from Fig. 3.5b, we see that the capacitance has a maximum as a function of chain length for various applied voltages. The maximum in the capacitance versus chain length is nontrivial–it cannot be explained simply by the bulk effect, which we saw is monotonically increasing from the expressions for ϵ_{bulk} in the previous section. Therefore, the nonmonotonicity of the capacitance in chain length must have surface contributions, which we explore next.

In order to characterize the surface contribution to the capacitance, we draw analogy with serial capacitors. The contributions to the capacitance can be separated into three capacitors connected in series—a bulk capacitor between two surface capacitors. The total capacitance is given by their inverse sum $\frac{1}{C} = \frac{1}{C_{\text{ex}}} + \frac{1}{C_{\text{bulk}}}$, where the term "exces" lumps both surface capacitors into a net surface-excess contribution. To obtain the bulk contribution, C_{bulk}, we note that serial capacitors all have the same surface charge, but have different applied voltage drops. Thus, the surface charge on all three capacitors is just the surface charge of the plates. On the other hand, the bulk capacitor voltage drop can be obtained by extrapolating the line in the bulk region of the electrostatic potential curves to the plates. Then, the bulk contribution to capacitance is given by the derivative of the surface charge with respect to the voltage drop in the bulk region. From this procedure, we obtain the bulk contribution to the capacitance as a function of chain length for various applied voltages, shown in Fig. 3.6a. From Fig. 3.6a, we see that the bulk capacitance increases monotonically in chain. Moreover, we see that the curves match $C_{\text{bulk}}/A = \varepsilon_0 \epsilon_{\text{bulk}}/L$ for small applied voltages (plotted as the black dashed line), where ϵ_{bulk} is the expression derived in previous section. This is an expected but satisfying result.

The surface-excess capacitance is calculated from $C_{\text{ex}} = 1/[\frac{1}{C} - \frac{1}{C_{\text{bulk}}}]$, and the result is shown in Fig. 3.6b. From Fig. 3.6b, we see that the surface-excess capacitance is monotonically decreasing in N. Therefore, the bulk and surface-excess contributions compete to give a nonmonotonic capacitance in chain length. Furthermore, increasing the chain length effectively increases the "free-ion characteristic" of the zwitterionic polymer—that is, the positive and negative ions feel less bound at large chain length. Consequently, this increases the width of the screening region/the surface region, and decreasing the surface excess capacitance. Therefore, the maximum of capacitance in chain length arises from a competition between the surface screening and bulk dielectric effects of the zwitterionic polymer.

3.7 Energy Density

We end our paper with a quantitative comparison of the energy density between systems with zwitterionic additives to model electric double-layer (EDL) systems. We also present a contour map for the energy density of a zwitterion-salt solution as a function of added zwitterion concentration $c_{\text{B,zw}}$ and zwitterion chain length N. Note that in this section, we focus on zwitterion-salt solutions, not melts. Given the possibility of zwitterions being used as high dielectric additives to increase capacitance, it is necessary to verify if adding zwitterion to an electrolyte solution actually gives a noticeable change in the energy density compared to the electrolyte alone.

First, we compare the energy density of a salt solution with added zwitterion to that of a salt-only and zwitterion-only solution at the same nominal ionic strength of $I = 1.0\,M$. All ions are monovalent and solvated in the same dielectric background (an arbitrary small molecule solvent), and the solution is incompressible. The chain length of the zwitterionic polymer is $N = 4$. The two solutions are compared on their energy density, defined by the reversible work of charging

$$W = \int_0^{\Delta V} \mathrm{d}v\, Cv. \tag{3.26}$$

Fig. 3.7a shows the the energy density of a zwitterion-only, salt-only, and zwitterion + salt solution as a function of applied voltage for three different ratios of bulk zwitterion ion concentration to bulk free salt concentration ($c_{\text{B,zw}} : c_{\text{B,f}}$). We see that the zwitterion-only solution performs worse than all cases for the range of applied voltage explored. The zwitterion + salt solution performs worse than salt alone for all three ratios at low applied voltage, but outperforms salt alone at high

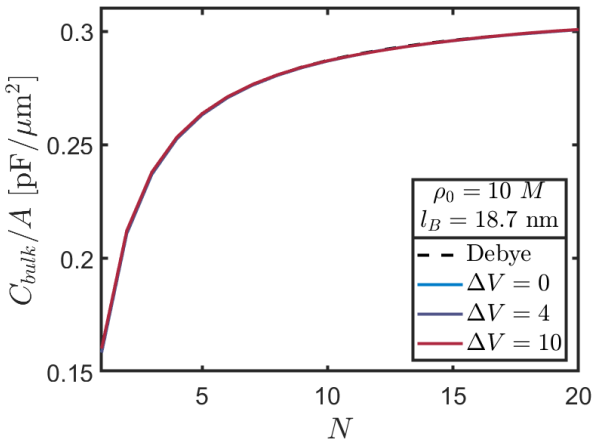

(a)

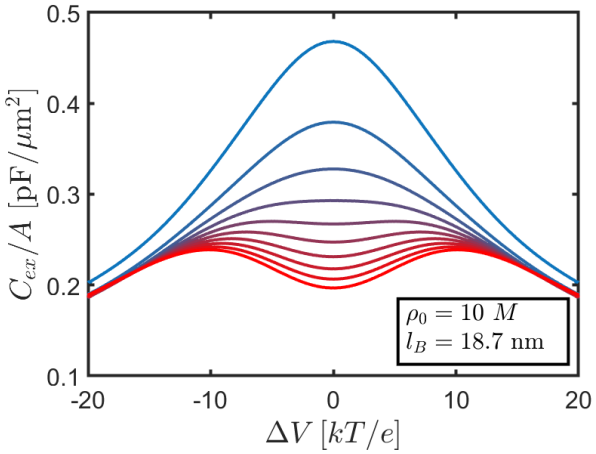

(b)

Figure 3.6: Bulk and excess differential capacitance for an incompressible zwitterionic polymer melt. The left and right plate are positively and negatively charged, respectively, with plate separation $L = 10$ nm. The polymer melt has statistical segment length $b = 0.5$ nm, incompressible density $\rho_0 = 10.0\,M$, and Bjerrum length $l_B = 18.7$ nm. (a) Bulk differential capacitance as a function of N for various applied voltages. The dashed black line is the Debye prediction from ϵ_{eff} in Eq. (3.25). (b) Excess differential capacitance as a function of applied voltage for various N increasing from 2 (blue) to 20 (red) bonds in steps of 2 through a color gradient.

applied voltage. This performance increase at higher applied voltage is more clearly seen from the ratio of the energy density to that of salt-only, shown in Fig. 3.7b. The zwitterion + salt solution outperforms salt-only solution more as the ratio of zwitterion to salt is increased, achieving a maximum percent increase of 8.2% at 49:1, compared to a 5.5% and 1.1% increase at 9:1 and 1:1, respectively. The reason for the increase in performance is due to the zwitterion stretching and becoming highly aligned with the electric field at high voltage, effectively raising the dielectric constant of the solution. This effect becomes more pronounced with greater excess of zwitterion because there is less free salt to screen the applied electric field, yielding a higher maximum in the energy density ratio. Note that the maximum for the 49:1 curve occurs around 50.4 kT/e, or 1.30 V, which is well within the operating range for supercapacitors [37]. Moreover, although the zwitterions become highly aligned at high applied voltage, the zwitterion-only solution performs worse than all other cases because there is insufficient accumulation of ions at the plates due to the lack of free-ions. These results are encouraging and show that zwitterions used as additives to salt solutions outperform their zwitterion-only and salt-only counterparts. Additionally, the results suggest zwitterions are most useful when added in great excess, giving significant enhancement in the energy density of a capacitor within its operating voltage.

Fig. 3.7c shows a contour map of the energy density W as a function of zwitterion chain length N and added zwitterion concentration $c_{\mathrm{B,zw}}$ for a lower applied voltage of $\Delta V = 2.0\ kT/e$ and salt concentration $c_{\mathrm{B,f}} = 0.1\ M$. We also note that all ion concentrations explored are within the operating conditions of supercapacitors [37]. From Fig. 3.7c, we see that stored energy density maximizes as both chain length and added zwitterion concentration increases. We believe these predictions will be useful in the design of supercapacitors with zwitterionic additives.

3.8 Conclusion

In this chapter, we studied the behavior of solutions of zwitterionic polymer with and without added salt. Employing only chain connectivity and mean-field electrostatics, we recovered bulk dielectric constants on the order of hundreds, in agreement with Ref. [6]. Additionally, we recovered the same expression as Ref. [17] for the effective dielectric constant of a zwitterion dimer. We then characterized the screening regimes of a zwitterionic polymer melt near a surface, demonstrating that the zwitterions have both as unbound-ion and dipole character—they partially screen near a surface but propagate a constant electric field through the bulk. Increasing

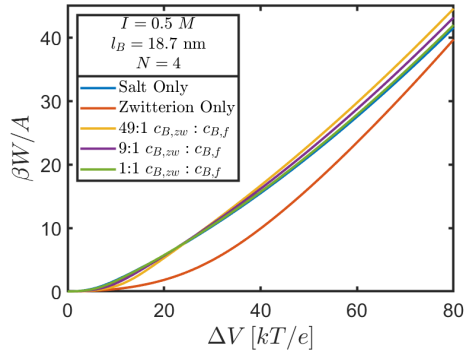

(a)

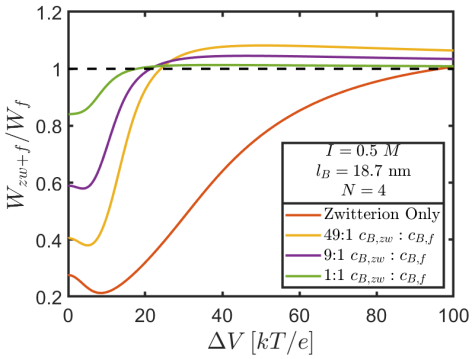

(b)

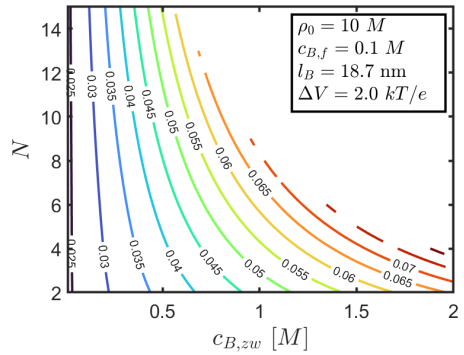

(c)

Figure 3.7: Energy densities for solutions of zwitterionic polymer and salt under various conditions. (a) Stored energy density for zwitterion-only, salt-only, and zwitterion + salt solution. Zwitterion + salt solution is shown for three different ratios of bulk zwitterion ion concentration to free salt concentration $c_{\mathrm{B,zw}} : c_{\mathrm{B,f}}$ of 49:1, 9:1, and 1:1. (b) Ratio of stored energy density for a zwitterion + salt solution to that of a salt-only solution. The solvent has Bjerrum length of $l_{\mathrm{B}} = 18.7$ nm. All solutions have same ionic strength $I = 1.0\,M$ and incompressible density $\rho_0 = 10\,M$. The zwitterionic polymer has $N = 4$ bonds. The plate separation is $L = 10$ nm. (c) Stored energy density $\beta W/A$ as a function of zwitterion chain length N and added zwitterion concentration $c_{\mathrm{B,zw}}$ at an applied voltage of $\Delta V = 2.0\ kT/e$ and salt concentration $c_{\mathrm{B,f}} = 0.1\ M$. The added zwitterion concentration cannot exceed the total density, giving an empty region on the upper-right section of the plot.

statistical segment length and chain length increases the unbound-ion character, whereas decreasing these parameters increases the dipole character. Next, we found the differential capacitance of a zwitterionic polymer melt has nonmonotonic behavior versus chain length, and we determined this behavior is a competition between bulk and surface effects. Then, we demonstrated that zwitterionic additives perform on par with salt-only capacitors for the same ionic strength. Most importantly, we found that zwitterions used as additives to salt solutions outperform the energy density of salt-only and zwitterion-only solutions at high applied potential. Additionally, zwitterions are best used in great excess of the free salt, giving an 8.2% increase in energy density compared to salt alone at the same nominal ionic strength. Lastly, we presented a contour map of the stored energy density for a zwitterion-salt capacitor as a function of added zwitterion concentration and zwitterion chain length and showed that energy density increases with increasing zwitterion concentration and chain length, although the energy density becomes sub optimal in the pure-zwitterion limit.

We note that our model does not account for enthalpic solvent-polymer interactions. Such interactions would lead to bulk and/or surface phase transitions that would affect operating conditions of zwitterionic-additive-based batteries and capacitors. Additionally, image charge effects introduced by the surface will modify zwitterion screening behavior which necessitates including electrostatic correlations. Lastly, we believe our model has other potential applications. One area is to explicitly represent dipolar solvents. Dipoles are cumbersome to treat in a theory even at a mean-field level, so using zwitterionic representations circumvents this issue. This route is advantageous because it captures solvent structure to a degree and modifications can be made to the architecture to better represent polar solvents, such as the multipolar model by Ref. [17], and in the electrostatic collapse of dipolar polymer gels [18]. This application is similar to the work of Ref. [16], although their work does not consider image charge effects which have been shown to significantly alter ion-solvation structure [38]. Lastly, since zwitterions have been demonstrated to have anti-fouling, anti-microbial, and drug-delivery applications [23, 39–44], it would be beneficial to develop theoretical models to capture these properties as well.

References

(1) Tiyapiboonchaiya, C.; Pringle, J. M.; Sun, J., et al. *Nat. Mater.* **2004**, *3*, 29–32, DOI: 10.1038/nmat1044.

(2) Zhu, L. *J. Phys. Chem. Lett.* **2014**, *5*, 3677–3687, DOI: 10.1021/jz501831q.

(3) Chen, Q.; Shen, Y.; Zhang, S.; Zhang, Q. *Annu. Rev. Mater. Res.* **2015**, *45*, 433–458, DOI: 10.1146/annurev-matsci-070214-021017.

(4) Kim, O.; Kim, H.; Choi, U. H.; Park, M. J. *Nat. Commun.* **2016**, *7*, 13576, DOI: 10.1038/ncomms13576.

(5) Zhao, Q.; Stalin, S.; Zhao, C.-Z.; Archer, L. A. *Nat. Rev. Mater.* **2020**, *5*, 229–252, DOI: 10.1038/s41578-019-0165-5.

(6) Mei, W.; Rothenberger, A. J.; Bostwick, J. E., et al. *Phys. Rev. Lett.* **2021**, *127*, 228001, DOI: 10.1103/PhysRevLett.127.228001.

(7) Mei, W.; Han, A.; Hickey, R. J.; Colby, R. H. *J. Chem. Phys.* **2021**, *155*, 244505, DOI: 10.1063/5.0074100.

(8) Xu, H.; Li, W.; Huang, L., et al. *Sci. China Mater.* **2023**, *66*, 3799–3809, DOI: 10.1007/s40843-023-2547-y.

(9) Hammami, A.; Raymond, N.; Armand, M. *Nature* **2003**, *424*, 635–636, DOI: 10.1038/424635b.

(10) Mandal, B. K.; Padhi, A. K.; Shi, Z.; Chakraborty, S.; Filler, R. *J. Power Sources* **2006**, *161*, 1341–1345, DOI: 10.1016/j.jpowsour.2006.06.008.

(11) Bandhauer, T. M.; Garimella, S.; Fuller, T. F. *J. Electrochem. Soc.* **2011**, *158*, R1, DOI: 10.1149/1.3515880.

(12) Bouchet, R.; Phan, T. N. T.; Beaudoin, E., et al. *Macromolecules* **2014**, *47*, 2659–2665, DOI: 10.1021/ma500420w.

(13) Jones, S. D.; Nguyen, H.; Richardson, P. M., et al. *ACS Cent. Sci.* **2022**, *8*, 169–175, DOI: 10.1021/acscentsci.1c01260.

(14) Budkov, Y. A.; Brandyshev, P. E.; Kalikin, N. N. *Soft Matter* **2023**, *19*, 3281–3289, DOI: 10.1039/D3SM00140G.

(15) Kumar, R.; Fredrickson, G. H. *J. Chem. Phys.* **2009**, *131*, 104901, DOI: 10.1063/1.3216107.

(16) Henderson, D.; Jiang, D.-e.; Jin, Z.; Wu, J. *J. Phys. Chem. B* **2012**, *116*, 11356–11361, DOI: 10.1021/jp305400z.

(17) Budkov, Y. A. *Phys. Chem. Chem. Phys.* **2020**, *22*, 14756–14772, DOI: 10.1039/D0CP02432E.

(18) Budkov, Y. A.; Kalikin, N. N.; Kolesnikov, A. L. *Chem. Commun.* **2021**, *57*, 3983–3986, DOI: 10.1039/D0CC08296A.

(19) Hallett, J. E.; Agg, K. J.; Perkin, S. *Proc. Natl. Acad. Sci. U.S.A.* **2023**, *120*.

(20) Ridwan, M. G.; Shrestha, B. R.; Maharjan, N.; Mishra, H. *J. Phys. Chem. B* **2022**, *126*, 1852–1860, DOI: 10.1021/acs.jpcb.1c10388.

(21) Qiang, J. *Comput. Phys. Commun.* **2010**, *181*, 313–316, DOI: 10.1016/j.cpc.2009.10.005.

(22) Fredrickson, G. H., *The Equilibrium Theory of Inhomogenous Polymers*; Clarendon Press: 2005.

(23) Jiang, S.; Cao, Z. *Adv. Mater.* **2010**, *22*, 920–932, DOI: 10.1002/adma.200901407.

(24) Muthukumar, M. *Gels* **2024**, *10*, 393, DOI: 10.3390/gels10060393.

(25) Jin, Z.; Wu, J. *J. Phys. Chem. B* **2011**, *115*, 1450–1460, DOI: 10.1021/jp110066z.

(26) Anderson, D. G. *J. ACM* **1965**, *12*, 547–560, DOI: 10.1145/321296.321305.

(27) Stasiak, P.; Matsen, M. W. *Eur. Phys. J. E* **2011**, *34*, 110, DOI: 10.1140/epje/i2011-11110-0.

(28) Hockney, R. W. *Methods Comput. Phys.* **1970**, 135–211.

(29) Fredrickson, G. H.; Delaney, K. T., *Field-Theoretic Simulations in Soft Matter and Quantum Fluids*; Oxford University Press: 2023; 399 pp.

(30) Levin, Y. *Phys. Rev. Lett.* **1999**, *83*, 1159–1162, DOI: 10.1103/PhysRevLett.83.1159.

(31) Budkov, Y. A. *J. Phys.: Condens. Matter* **2018**, *30*, 344001, DOI: 10.1088/1361-648X/aad3ee.

(32) Orttung, W. H. *J. Phys. Chem.* **1963**, *67*, 1102–1105, DOI: 10.1021/j100799a040.

(33) White, A.; Jiang, S. *J. Phys. Chem. B* **2011**, *115*, 660–667, DOI: 10.1021/jp1067654.

(34) Qing, L.; Zhao, S.; Wang, Z.-G. *J. Phys. Chem. B* **2021**, *125*, 625–636, DOI: 10.1021/acs.jpcb.0c09332.

(35) Budkov, Y. A. *Journal of Molecular Liquids* **2019**, *276*, 812–818, DOI: 10.1016/j.molliq.2018.12.057.

(36) Kornyshev, A. A. *J. Phys. Chem. B* **2007**, *111*, 5545–5557, DOI: 10.1021/jp067857o.

(37) Yu, M.; Lu, Y.; Zheng, H.; Lu, X. *Chem. Eur. J.* **2018**, *24*, 3639–3649, DOI: 10.1002/chem.201704420.

(38) Son, C. Y.; Wang, Z.-G. *Proc. Natl. Acad. Sci. U.S.A* **2021**, *118*, 8.

(39) Schlenoff, J. B. *Langmuir* **2014**, *30*, 9625–9636, DOI: 10.1021/la500057j.

(40) Zheng, L.; Sundaram, H. S.; Wei, Z.; Li, C.; Yuan, Z. *React. Funct. Polym.* **2017**, *118*, 51–61, DOI: 10.1016/j.reactfunctpolym.2017.07.006.

(41) Blackman, L. D.; Gunatillake, P. A.; Cass, P.; Locock, K. E. S. *Chem. Soc. Rev.* **2019**, *48*, 757–770, DOI: 10.1039/C8CS00508G.

(42) Shao, Q. *Mol. Simul.* **2019**, *45*, 1211–1222, DOI: 10.1080/08927022.2019.1599118.

(43) Asha, A. B.; Chen, Y.; Narain, R. *Chem. Soc. Rev.* **2021**, *50*, 11668–11683, DOI: 10.1039/D1CS00658D.

(44) Chen, P.; Lang, J.; Zhou, Y., et al. *Sci. Adv.* **2022**, *8*.

Chapter 4

IMAGE CHARGE EFFECTS UNDER METAL AND DIELECTRIC BOUNDARY CONDITIONS

Image charge effect is a fundamental problem in electrostatics. However, a proper treatment at the continuum level for many-ion systems, such as electrolyte solutions or ionic liquids, remains an open theoretical question. Here, we demonstrate and systematically compare the image charge effects under metal and dielectric boundary conditions (BCs), based on a renormalized Gaussian-fluctuation theory. Our calculations for a simple 1:1 symmetric electrolyte in the point-charge approximation show that the double-layer structure, capacitance, and interaction forces between like-charged plates depend strongly on the types of boundaries, even in the weak-coupling regime. Like-charge attraction is predicted for both metal and dielectric BCs. Finally, we comment on the effects of a dielectrically-saturated solvent layer on the metal surface. We provide these results to serve as a baseline for comparison with more realistic molecular dynamics simulations and experiments.

This chapter includes content from our previously published article:

(1) Zhou, T.; Bruch, D.; Wang, Z.-G. Image charge effects under metal and dielectric boundary conditions, en, arXiv:2405.13261 [cond-mat], 2024,

I am thankful to Dr. Tingtao Zhou for allowing me to join this project.

Image charge (IC) interaction has wide implications in electrostatics problems with interfaces. A classic example is the study on surface tension of electrolyte solutions pioneered by Wagner [1] and Onsager and Samaras [2], where the IC repulsion at air/water interface was considered responsible for the increase in the surface tension due to added salt ions. Monte Carlo simulations [3, 4] and an integral equation theory based on hypernetted chain approximation [5] have shown ion depletion near a weakly charged dielectric interface, while ion accumulation near a metal interface is expected. Nanoscale supercapacitors have received recent interest for nanoscale device applications [6–8] and may be used to probe material characteristics at the molecular level [9]. These nanoscale devices require proper treatment of IC effects. IC interaction also affects the study of capacitive desalination [10], capillary freezing of ionic liquids [11], surface adsorption of ions [12], ion transport in charged nanoporous materials [13], and may even play a role in planet formation [14].

The Poisson–Boltzmann (PB) theory has been widely accepted as the leading order theory for the weak-coupling regime of electrostatics [3, 15–18], but it does not include ion-correlation or IC effect. Theoretically, a primitive treatment is to explicitly construct the image charge of a single ion and modify the free energy at the interface [2]. In field-theoretic formulations, perturbative loop-expansion treatments have been used to derive corrections to the PB theory [16, 19, 20] to include IC interactions. However, by analysis of a single point charge approaching a bounding interface, one can show that the image charge interaction diverges as the charge approaches the interface [21]. For a dielectric interface, this singular behavior results in a singular boundary layer of the electrolyte close to the interface, eluding regular perturbation methods [15]. Ref. [22] derived a renormalized field-theory framework with implicit solvent. There, the solvent is modeled as a continuum with an effective dielectric constant. Sharp dielectric interfaces have been studied using this framework [23, 24] and lattice Monte Carlo simulations [25] have shown good agreement with the predictions from Ref. [23]. Other field-theoretic treatments including IC interactions usually introduce an arbitrary cutoff to avoid divergence of self-energy [26, 27]. For the metal boundary, several techniques for Molecular Dynamics (MD) simulations have been devised to account for the IC interactions, such as iterative methods [28–31], explicit construction of image charges [32–36], or directly updating polarization charges at interfaces with Car-Parrinello molecular dynamics [37], and ion accumulation on the metal surfaces has been observed [38]. Simulations using the method of periodic Green's functions have also been constructed for both dielectric and metal boundaries [38]. In all of these simulations,

the solvent is treated implicitly where the polarization of the solvent is modeled by a bulk dielectric constant. However, as found in Ref. [39], IC interaction is strongly affected by the polarizability of both solvent molecules and ions — a polarizable solvent even cancels out some effects of the IC, which is neglected in models with implicit solvent background.

IC effects are known to be important for electric double layer capacitors. For example, experimental evidence shows that surface polarizability leads to a much higher differential capacitance than expected [40], and IC interaction may even lead to a phase transition at the electrolyte-metal interface [41, 42] or induce symmetry breaking patterns on the interface [43]. For room-temperature ionic liquids, MD simulations and 1D model analysis [44, 45] showed importance of IC effects on capacitance curves. For lower bulk salt concentrations, recent MD simulations [39] have shown significant enhancement of charge separation in a nano-supercapacitor with conducting electrodes. MD simulations also showed [46] non-trivial properties of double-layer structures of polyelectrolytes due to surface polarization for both dielectric and metal boundaries.

IC effects also influence colloidal interactions [47, 48], which play a critical role in many soft matter systems. The classic DLVO theory [49] predicts only screened repulsive electrostatic interactions. More recent efforts extending the PB theory, such as the renormalized jellium model [50–54], result in a renormalized charge but qualitatively same repulsive tendency. In fact, Trizac has shown that generally local density approximations lead to repulsive pair potentials [55]. Nevertheless, like-charged colloidal attraction have been reported [56–58] and has wide implications. For example, during cement setting, attraction between like-charged surfaces may allow the cohesion strength to increase beyond the order of magnitude of capillary stress [59–61] or van der Waals interaction. Without systematic considerations of IC effects, the like-charge attraction has been mostly attributed to ion-ion correlations and fluctuations [5, 15, 62–68]. These correlation effects are generally thought to become significant at the strong-coupling limit [69–72], typically from high surface charge density or multi-valent ions. In the weak-coupling regime, Refs. [23, 73] have shown like-charge attraction due to IC-induced ion depletion between dielectric plates. For 1:1 electrolyte with metal boundary conditions and fixed surface charge density, dos Santos & Levin [74] concluded that attraction between like-charged particles can happen for spheres even at the level of the PB theory.

In reality, IC interaction can be further complicated by various other factors. These

interfacial effects are often ion-specific [75], such as the famous Hofmeister series [76] for protein salt-in/salt-out. The hydration shell structure of the ions also changes when they are adsorbed onto a metal surface, which affects their hydration energy. In addition, more complex and unexpected behaviors of the differential capacitance have been reported in MD simulations with polyelectrolytes [46]. In the case of a free interface, the IC interaction is also coupled with surface capillary waves [77–79]. These complications are beyond the scope of this work.

In this paper, we provide a simple theoretical picture of the IC effects as a reference for further studies with more realistic molecular models for electrolytes. To this end, we treat all ions as point charges and assume an implicit solvent background. We present a systematic comparison between the metal BC, dielectric BC, and PB theory in terms of the differential capacitance of nano-capacitors and forces between like-charged plates by numerically solving the variational field theory for an incompressible electrolyte. Our calculations show that the differential capacitance depends strongly on the boundary condition (metal or dielectric) as well as the bulk salt concentration. For example, even at low bulk concentration but if the slit width is small, the metal BC leads to a "bird-shaped" capacitance curve [80]. For a simple 1:1 electrolyte, we find the interplate forces change from repulsion to attraction as the separation distance decreases between dielectric plates, and stronger and long-ranged attractions between like-charged metal plates, due to the IC interaction. Moreover, to account for the distance of closest approach of real ions to a surface, we consider a thin layer of polarizable solvent on the metal surface, preventing direct contact of ions with the boundary. We show that even a very thin surface dielectric layer cancels out some IC effects, consistent with the findings in Ref. [39].

4.1 Theory

General Gaussian variational approach

We start by recapitulating the field-theoretic framework as presented in Ref. [22]. Consider a system with cations (of valence z_+) and anions (of valence $-z_-$) in an electrolyte solution, and external charges on the boundary surfaces $e\rho_{ex}$. The solution is connected to a reservoir with bulk cation and anion concentrations $c_{+,0}$ and $c_{-,0}$, respectively. The total microscopic charge density is

$$e\rho(\mathbf{r}) = e\left(\rho_{ex}(\mathbf{r}) + z_+ \sum_{i+} h_+(\mathbf{r}-\mathbf{r}_+^i) - z_- \sum_{j-} h_-(\mathbf{r}-\mathbf{r}_-^j)\right) \tag{4.1}$$

where the salt ions have a charge spread kernel, which is taken to the point charge limit $h_{\pm}(\mathbf{r}-\mathbf{r}_{\pm}^{i}) = \delta(\mathbf{r}-\mathbf{r}_{\pm}^{i})$ throughout this work. The Coulomb energy is

$$H = \frac{e^2}{2}\int d\mathbf{r}d\mathbf{r}'\rho(\mathbf{r})G_0(\mathbf{r},\mathbf{r}')\rho(\mathbf{r}') \tag{4.2}$$

where the Coulomb operator G_0 is defined by

$$-\nabla\cdot\varepsilon(\mathbf{r})\nabla G_0(\mathbf{r},\mathbf{r}') = \delta(\mathbf{r}-\mathbf{r}'). \tag{4.3}$$

The grand canonical partition function is

$$\begin{aligned}\Xi =& \sum_{n_+}\sum_{n_-}\frac{e^{n_+\mu_+}e^{n_-\mu_-}}{n_+!n_-!v_+^{n_+}v_-^{n_-}}\int d\mathbf{r}_{i+}d\mathbf{r}_{j-}e^{-\beta H}\\ =&\frac{1}{\sqrt{\det(G_0)}}\int D[\phi]e^{-\int d\mathbf{r}\mathcal{L}[\phi(\mathbf{r})]}\end{aligned} \tag{4.4}$$

where the action density is

$$\mathcal{L}[\phi] = \frac{1}{8\pi\ell_B}\left(\nabla\phi(\mathbf{r})\right)^2 + i\rho_{ex}(\mathbf{r})\phi(\mathbf{r}) - \lambda_+e^{-iz_+\phi(\mathbf{r})} + \lambda_-e^{iz_-\phi(\mathbf{r})}. \tag{4.5}$$

For convenience Equation. (4.5) and subsequent ones throughout the paper are written in dimensionless variables. The Bjerrum length is $\ell_B = e^2/(4\pi\epsilon k_BT)$. The complex-valued auxiliary field $\phi(\mathbf{r})$ conjugate to the charge density $\rho(\mathbf{r})$ is introduced through the standard Hubbard–Stratonovich transformation [81, 82] and then non-dimensionalized by k_BT/e. $\lambda_{\pm} = \frac{e^{\mu_{\pm}}}{v_{\pm}}$ are the bulk activities of salt ions, where $\mu_{\pm}$ are the chemical potentials and $v_{\pm}$ are the volume scales which have no thermodynamic consequences other than shifting the reference of the chemical potential; therefore, for convenience, we choose $v_{\pm}$ to be simply the volume of the ions. A renormalization of the field theory then can be derived through a variational approach by extremizing [22, 83] the grand free energy

$$W \le W_{ref} + \left\langle L[\phi] - L_{ref}[\phi]\right\rangle_{ref}. \tag{4.6}$$

The auxiliary field is decomposed into

$$\phi(\mathbf{r}) = -i\psi(\mathbf{r}) + \chi(\mathbf{r}) \tag{4.7}$$

where the mean-field part $-i\psi(\mathbf{r})$ and fluctuation parts $\chi(\mathbf{r})$ are purely imaginary and real fields, respectively. The reference action is chosen as a Gaussian form for the fluctuation part for the auxiliary field

$$L_{ref} = \frac{1}{2}\int d\mathbf{r}d\mathbf{r}'\chi(\mathbf{r})G^{-1}(\mathbf{r},\mathbf{r}')\chi(\mathbf{r}'). \tag{4.8}$$

The Green's function $G(\mathbf{r},\mathbf{r}')$ is unknown and will be determined together with the mean-field $\psi(\mathbf{r})$ by the extremization of W, which results in

$$-\nabla\cdot\left[\frac{1}{4\pi\ell_B(\mathbf{r})}\nabla\psi(\mathbf{r})\right] = \rho_{ex}(\mathbf{r}) + z_+c_+(\mathbf{r}) - z_-c_-(\mathbf{r}) \tag{4.9}$$

$$-\nabla\cdot\left[\frac{1}{4\pi\ell_B(\mathbf{r})}\nabla G(\mathbf{r},\mathbf{r}')\right] + 2I(\mathbf{r})G(\mathbf{r},\mathbf{r}') = \delta(\mathbf{r}-\mathbf{r}') \tag{4.10}$$

where the ionic strength is $I(\mathbf{r}) = \frac{1}{2}\left[z_+^2c_+(\mathbf{r}) + z_-^2c_-(\mathbf{r})\right]$, and ion concentrations are

$$c_\pm(\mathbf{r}) = \lambda_\pm \exp\left\{\mp z_\pm\psi(\mathbf{r}) - u_\pm(\mathbf{r})\right\} \tag{4.11}$$

with the self energy

$$u_\pm(\mathbf{r}) = \frac{1}{2}z_\pm^2 G(\mathbf{r},\mathbf{r}'\to\mathbf{r}). \tag{4.12}$$

Here the self-energy appears in the exponential of the Boltzmann factor of the charge distributions and it is the key feature of this framework. It includes a singular part, which is present even in a homogeneous solution without boundaries; this singular part can be regularized by the introduction of a smearing function [22], with a spread chosen to reproduce the Born solvation energy in a bulk electrolyte solution and can be absorbed into the bulk ion chemical potentials. The remaining part of the self-energy comes from spatial variations of charge distribution, correlation energy, and the existence of boundaries and image charges. This part of the self-energy is finite inside a continuum electrolyte, except at dielectric discontinuities and boundaries.

Incompressible electrolyte

Even within the PB framework, ion densities near electrolyte–metal interfaces can be overestimated and exceeds the physically maximum value of close packing [84], due to the unconstrained exponential dependence of ion concentration on the electric potential. The point-charge approximation in the variational field theory presented in the last section still exhibits divergent self energy near an interface [21], resulting in complete ion depletion (divergent accumulation) near a dielectric (metal) wall, necessitating a proper consideration of finite ion sizes, which can be treated at different levels. The first step of improvement is to constrain the total concentration by an incompressibility condition, which prevents the divergence of ion accumulation or self energy, without introducing an explicit length scale for the ions. The next level of improvement is to introduce explicitly a finite ion size by either charge spread (h in Eqn. 4.1) or a hard sphere radius in a primitive model. At the mean-field level, explicit modeling of ion sizes can lead to a generalized Boltzmann distribution [85]. Moreover, incorporation of charge spread [86] or a hard sphere radius [87] leads to oscillations in ion densities, and in concentrated electrolytes, these oscillations become important and lead to effects such as a nonmonotonic dependence of the screening length on ion concentration [87].

As we focus on a proper comparison between the different boundary conditions for IC effects, we adopt the minimum model with incompressibility constraint [88, 89] to regulate ion concentration near the boundary surfaces. This way, the IC interaction is still calculated for point charges that can approach the interface indefinitely close, and hence the IC force may diverge as expected, but the ion concentration is regulated by a saturation value. The incompressibility condition is represented by a product of delta functions that enforces the solution density $\frac{1}{v_0}$ at every point in space, $\prod_{\mathbf{r}} \delta\left(\hat{c}_+(\mathbf{r}) + \hat{c}_-(\mathbf{r}) + \hat{c}_s(\mathbf{r}) - \frac{1}{v_0}\right)$, where the number densities of cation, anion and solvent molecules are

$$\begin{aligned} \hat{c}_+(\mathbf{r}) &= \sum_{i+} \delta(\mathbf{r} - \mathbf{r}_+^i) \\ \hat{c}_-(\mathbf{r}) &= \sum_{i-} \delta(\mathbf{r} - \mathbf{r}_-^i) \\ \hat{c}_s(\mathbf{r}) &= \sum_{s-} \delta(\mathbf{r} - \mathbf{r}_s^i). \end{aligned} \tag{4.13}$$

For simplicity we have assumed that the volumes of all species (cation, anion, and

solvent) are equal $v_+ = v_- = v_s = v_0 = (0.5\text{ nm})^3$, so that the total concentration of all species is $c_0 \approx 13.33$ M everywhere.

To deal with the incompressibility constraint, we represent the product of delta functions as its Fourier transform by introducing an auxiliary field $\eta(\mathbf{r})$

$$\prod_{\mathbf{r}} \delta\left(\hat{c}_+(\mathbf{r}) + \hat{c}_-(\mathbf{r}) + \hat{c}_s(\mathbf{r}) - \frac{1}{v_0}\right) = \int D[\eta(\mathbf{r})] e^{i\int d\mathbf{r}\eta(\hat{c}_+ + \hat{c}_- + \hat{c}_s - \frac{1}{v_0})} \tag{4.14}$$

where the notation $\int D[\eta(\mathbf{r})]$ is the functional integral with respect to the field $\eta(\mathbf{r})$. Now $\hat{c}_{\pm,s}(\mathbf{r})$ still depend on the ion/solvent positions $\{\mathbf{r}^i\}$, which are integrated over in the grand partition function.

With this constraint incorporated into the grand partition function, extremizing the grand free energy with respect to the new auxiliary fields gives modified equations for concentration fields

$$c_\pm(\mathbf{r}) = \lambda_\pm e^{\mp(z_\pm\psi(\mathbf{r})) + \eta(\mathbf{r}) - u_\pm(\mathbf{r})} \tag{4.15}$$

$$c_s(\mathbf{r}) = \frac{e^{\mu_s}}{v_0} e^{\eta(\mathbf{r})} \tag{4.16}$$

$$\frac{1}{v_0} = c_+(\mathbf{r}) + c_-(\mathbf{r}) + c_s(\mathbf{r}) \tag{4.17}$$

where these Equations (4.15) and (4.16) are obtained from the integrand of chemical potential derivatives of the grand free energy. Note that the differential equations (4.9) – (4.10) for the electric potential ψ and Green's function G remain the same. Hence, the treatment for incompressibility is at the mean-field level. For consistency in the comparisons throughout this paper, we impose the incompressibility condition for all cases—PB theory, metal and dielectric BCs, and for a thin dielectric surface layer on a metal wall.

Force and capacitance between two plates

Consider an electrolyte solution confined between two infinite parallel plates. In this work, we focus on comparing four cases of boundary conditions (BCs): (1) both plates are perfect metal; (2) both plates are dielectric medium with a dielectric

constant $\epsilon_p = 2$, lower than that of the solution, assumed to be $\epsilon_r = 80$; (3) PB theory without image charge corrections; and (4) both plates are metal with a thin dielectric surface layer with a dielectric constant ϵ_{L}, lower than that of solution. For simplicity, cases (2) and (4) will be referred to as dielectric and layer BC from now on, respectively. The electrolyte is connected to a bulk 1:1 solution of salt ion concentrations $c_{+,0} = c_{-,0} = c_0$; hence, the calculations are in the grand canonical ensemble.

Due to the translational and rotational symmetry in the directions parallel to the plates, it is convenient to use cylindrical coordinates (ρ, θ, z). The Equations (4.9), (4.10) and (4.15) – (4.17) are simplified to a set of 1D ordinary differential equations (ODEs) along the z-axis perpendicular to the plates

$$-\frac{1}{4\pi\ell_B}\frac{\partial^2}{\partial z^2}\psi(z) = \rho_{ex}(z) + c_+(z) - c_-(z) \tag{4.18}$$

$$\delta(z - z') = \frac{1}{4\pi\ell_B}\left\{\left[k^2 + \kappa(z)^2\right] - \frac{\partial^2}{\partial z^2}\right\} G(k, z, z') \tag{4.19}$$

$$c_\pm(z) = \lambda_\pm e^{\eta(z) - u(z) \mp \psi(z)} \tag{4.20}$$

$$u(z) = u_{Born} + u_{DH} + \frac{1}{4\pi}\int_0^\infty dk\ (kG(k, z, z) - 2\pi\ell_B) \tag{4.21}$$

$$\kappa(z)^2 = 4\pi\ell_B\left[c_+(z) + c_-(z)\right] \tag{4.22}$$

$$c_s(z) = \lambda_s e^{\eta(z)} \tag{4.23}$$

$$\frac{1}{v_0} = c_+(z) + c_-(z) + c_s(z) \tag{4.24}$$

where we use the partial Fourier transform $G(k, z, z')$ of the Green function $G(\mathbf{r}, \mathbf{r}')$: by symmetry of the geometry $G(\mathbf{r}, \mathbf{r}') = G(|\rho - \rho'|, z, z')$. One then only Fourier transforms the separation $s = |\rho - \rho'|$ in the parallel direction

$$G(|\rho - \rho'|, z, z') = \frac{1}{2\pi}\int_0^\infty k dk J_0(ks) G(k, z, z') \tag{4.25}$$

where $J_0(x)$ is the zeroth-order Bessel function. After the partial Fourier transform, Equation (4.10) becomes Equation (4.19). Inverse Fourier transforming $G(k, z, z')$ back and taking the limit of $\rho \to \rho'$, $z \to z'$ according to Equation (4.12) gives Equation (4.21). In Equation (4.21), the singular part of the self-energy is replaced with a constant reference energy, including the Born energy $u_{Born} = z^2\ell_B/(2a)$ and a Debye-Hückel correlation term $u_{DH} = -z^2\ell_B\kappa_B/2$, which is assumed homogeneous

inside the domain and in the reservoir, and hence can be absorbed into the bulk fugacity. $\kappa_B = \sqrt{8\pi c_0 \ell_B}$ is the inverse Debye length in the bulk solution. Only the excess part (second term of RHS in Equation (4.21)) will be relevant for our purpose here. By setting $\eta = 0$ for the reservoir, the chemical potentials are determined by the bulk concentrations

$$\lambda_s = \frac{1}{v_0} - 2c_0 \tag{4.26}$$

$$\lambda_\pm e^{-u_\infty} = c_{\pm,0} = c_0. \tag{4.27}$$

The BCs for the ODE Eq. (4.18) can be set by fixing the surface potential (Dirichlet) or fixing the surface charge density (Neumann), depending on the specific application. We now specify the BCs for the ODE Eq. (4.19) for the Green's function at the surfaces $z = -L/2$ and $z = L/2$. With metal plates, there is no fluctuation inside the metal, so $G(z = -L/2, z') = G(z = L/2, z') = 0$ (noting that $G(\mathbf{r}, \mathbf{r}') = \langle \chi(\mathbf{r})\chi(\mathbf{r}') \rangle$ is the variance of the fluctuation field $\chi(\mathbf{r})$ from its defining Equation. (4.8)). With dielectric plates of relative permitivity ϵ_p, different from the solvent relative permitivity ϵ_r, the equation can be extended to the whole space and the dielectric constant is regarded as having a discontinuity at $z = \pm L/2$ so that $\epsilon(z) = \epsilon_p$ outside $|z| > L/2$ and $\epsilon(z) = \epsilon_r$ inside $|z| < L/2$. Accounting for this jump one arrives at [24] a Robin BC for $G(k, z, z')$

$$\epsilon_r \partial_z G(k, z = \pm L/2, z') = \mp k \epsilon_p G(k, z = \pm L/2, z'). \tag{4.28}$$

For the case of a thin dielectric layer on the metal surface, the metal surface is at fixed potential, and Equations (4.18) and (4.19) have Robin boundary conditions, derived in Appendix C.

The differential capacitance $C_d = d\sigma_s/dV$ can be readily obtained by sweeping the voltage V, which is symmetrically applied on both plates such that $\psi(z = \pm L/2) = V$. σ_s is the surface charge density on a plate. We also examine forces between like-charged plates by continuously varying their separation distance and computing the total grand free energy W. In any case, the free energy per unit area of the system is [24]

$$
\begin{aligned}
W = \frac{1}{2}\int dz\psi(z)\left\{\rho_{ex}(z) - c_+(z) + c_-(z)\right\} \\
+ \int dz(\eta(z)-1)\left\{c_+(z) + c_-(z) + c_s(z)\right\} \\
+ \int dz I(z)\int_0^1 [G(z,z;\xi) - G(z,z)]d\xi
\end{aligned}
\tag{4.29}
$$

for fixed surface charges σ_s, and performing a Legendre transform gives the free energy $Y = W - 2\sigma_s V$ for fixed surface potentials at $\psi(z = \pm L/2) = V$. The "charging" Green's function $G(z, z'; \xi)$ is obtained by solving Eq. (4.19) but with $\kappa(z)^2$ replaced by $\xi\kappa(z)^2$. The force per unit area is

$$
\Pi = -\frac{\partial\left(\mathcal{W}(L) - \mathcal{W}(\infty)\right)}{\partial L} \tag{4.30}
$$

and $\mathcal{W}$ is W or Y depending on whether surface charge or surface potential is specified [90].

4.2 Numerical Results and Discussions

We numerically evaluate the Equations (4.18) – (4.24) iteratively. For the fixed voltage (Dirichlet) boundary conditions, the Poisson equation (4.18) is solved by the Chebyshev spectral method, and we combine the Chebyshev and shooting methods to solve the fixed charge (Neumann) boundary condition. For a given pair of k and z' values, the Green's function is solved by a finite difference method with non-uniform grid size for accuracy. For the inverse Fourier transform, the integration over k in Equation (4.21) is performed with Gauss–Laguerre quadrature. The numerical scheme converges in a few minutes for density profiles and a few hours for capacitance/force curves. A diagram of the systems considered is shown in Fig. 4.1.

Charge accumulation/depletion at the surface

For a single point charge near a planar surface, its image charge is known to be attractive for a metal boundary and repulsive for a dielectric medium with a lower dielectric constant than that of the electrolyte. As the point charge approaches the boundary interface, its distance to the image charge decreases to 0, resulting in a divergent image charge interaction. This is reflected in the self-energy diverging at the domain boundaries as shown in Fig. 4.2(a). The wall surface for both curves in

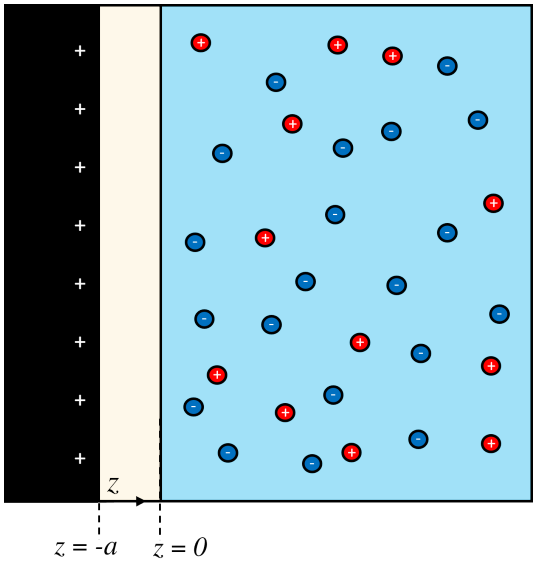

Figure 4.1: A solution of monovalent ions near a charged wall. The ions have bulk concentration c_0 and the solution has dielectric constant $\varepsilon_r = 80$. The charged wall is located at $z = -a$ and has a thin dielectric surface layer of thickness a and dielectric constant ε_L. For slit-pore conditions, there is another charged wall (not shown) at $z = L + a$ that has a dielectric surface layer at $z = L$. For purely metal or dielectric BCs, there are no thin dielectric surface layers ($a = 0$).

Fig. 4.2 are fixed at $V = 0$, and bulk ion concentrations are $c_{+,0} = c_{-,0} = 0.1$ M. The self-energy near the surface has two contributions: (1) there are no other salt ions inside the plate, hence less correlation energy. (2) the dielectric property of the plate differs from the solution, leading to IC interactions. For dielectric BC, salt ions are completely depleted from the surface; for metal BC, the ion density saturates at the surface as shown in Fig. 4.2(b). The cation and anion profiles overlap for either metal or dielectric BC since there is no applied voltage or fixed charges. Although in both cases the electric potential is a constant zero everywhere, the concentration profiles are nontrivial and nonuniform, different from the PB solution that gives trivial constant concentrations equal the bulk value of 0.1 M. Away from the boundary-layer zone, both dielectric and metal BCs show exponentially decaying deviations of ion densities from the bulk with a similar screening length, while the metal curve shows a significantly different screening length for the boundary layer zone, as shown in the inset of Fig. 4.2(b).

For two parallel plates (a slit pore) with $V = 0$ on both, the double layers from the two surfaces start to overlap as the separation between the plates decreases. Hence, the middle-point self-energy and ion concentrations deviate from the bulk values

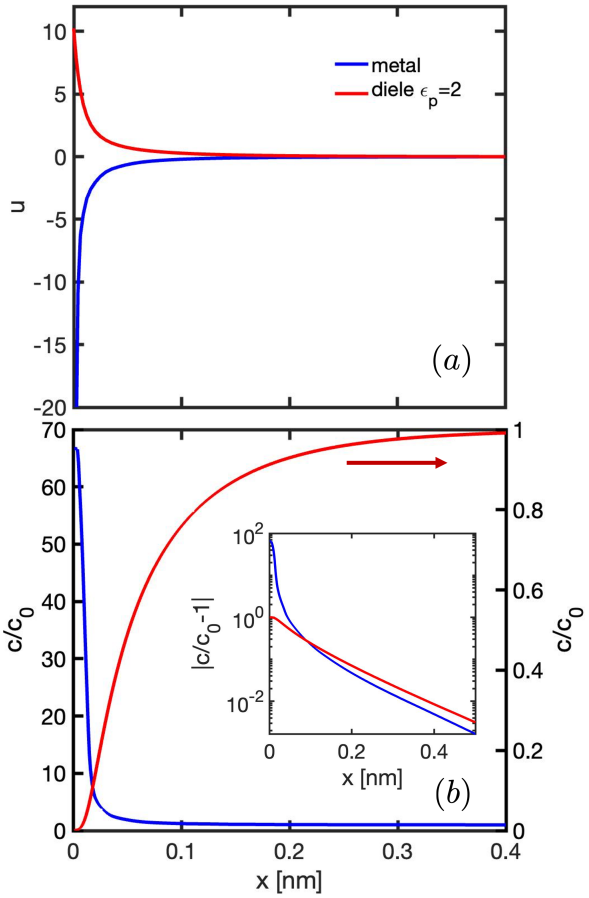

Figure 4.2: Charge accumulation/depletion at the planar boundary due to image charge interactions. No applied voltage or fixed surface charge on the wall. The bulk salt concentration is $c_0 = 0.1$ M for each case. The dielectric constant of the implicit solvent is $\epsilon_r = 80$; for the dielectric plates, $\epsilon_p = 2$. (a) Self-energy profiles corresponding to metal BC (blue) and dielectric BC (red). (b) Concentration profiles: the blue line represents the metal BC, corresponding to the left y-axis. The red line represents the dielectric BC, corresponding to the right y-axis. The inset shows the deviations from bulk concentration c_0 (absolute value $|c/c_0 - 1|$) on the same log-scale y-axis.

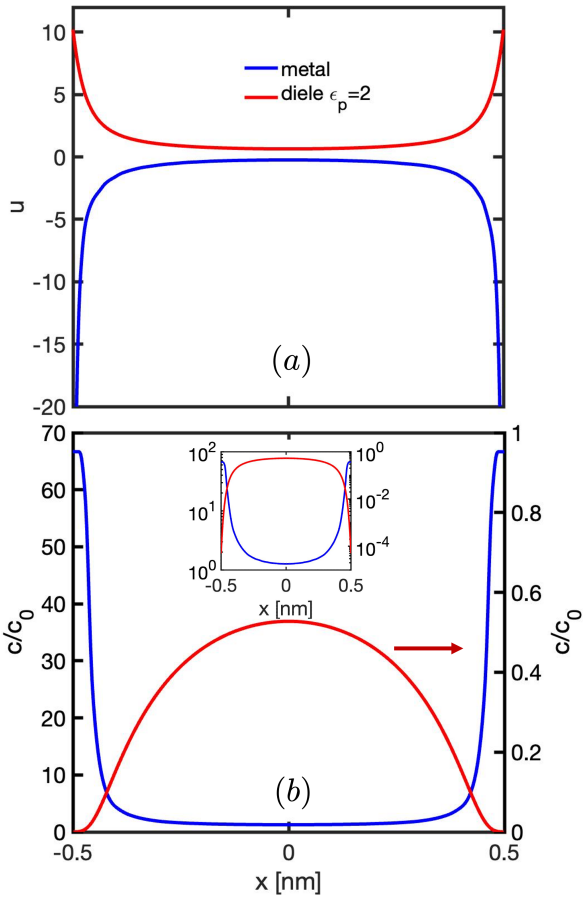

Figure 4.3: Finite-size effect on the charge accumulation/depletion at the boundaries due to image charge interactions without applied voltage or fixed charge. The slit pore width is $L = 1$ nm and the bulk salt concentration is $c_0 = 0.1$ M for each case. The dielectric constant of the implicit solvent is $\epsilon_r = 80$; for the dielectric plates, $\epsilon_p = 2$. (a) Self-energy profiles corresponding to metal BC (blue) and dielectric BC (red). (b) Concentration profiles: the cation and anion profiles overlap for either metal or dielectric BC since there is no voltage applied. The blue line shows the metal BC and red line shows the dielectric BC. The inset shows both profiles in semilog-scale.

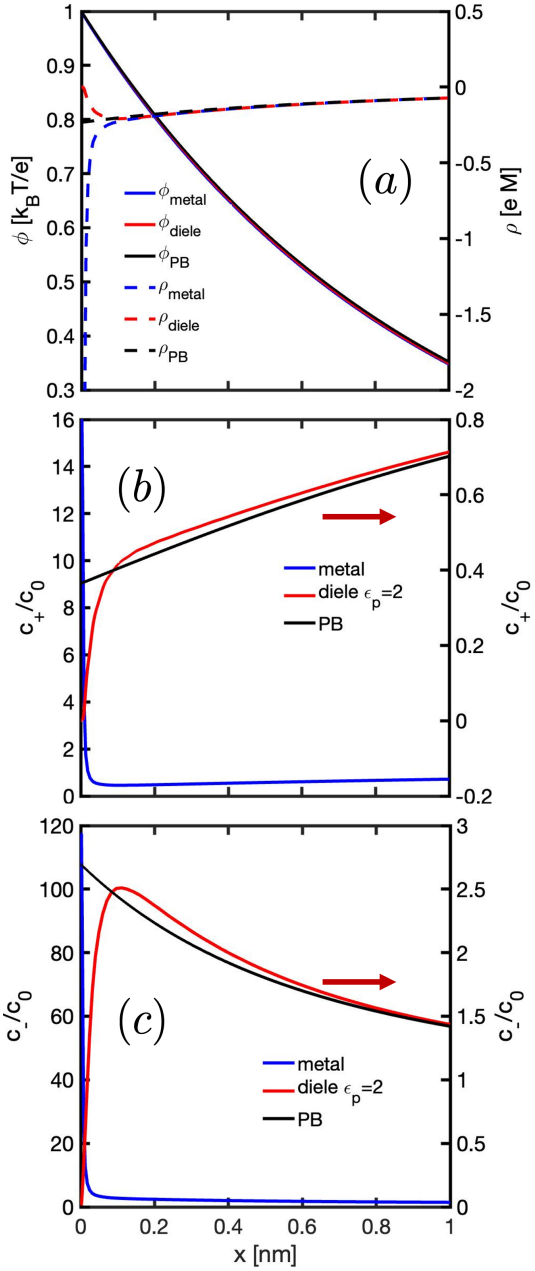

Figure 4.4: Single wall fixed at surface potential $V = 1$. Bulk ion concentrations are $c_{0,+} = c_{0,-} = 0.1$ M. The implicit solvent has dielectric constant $\epsilon_r = 80$. To amplify the boundary layer, we zoom into the region $0 < x < 1$ nm. (a) Electric potential profiles for the metal (blue solid), dielectric (red solid) and PB (black dashed) BCs. (b) Cation profiles with metal BCs (blue, left-y axis), dielectric (red, right y-axis) BCs, and PB theory (black, right y-axis). (c) Anion profiles: legends and axes are the same as in (b).

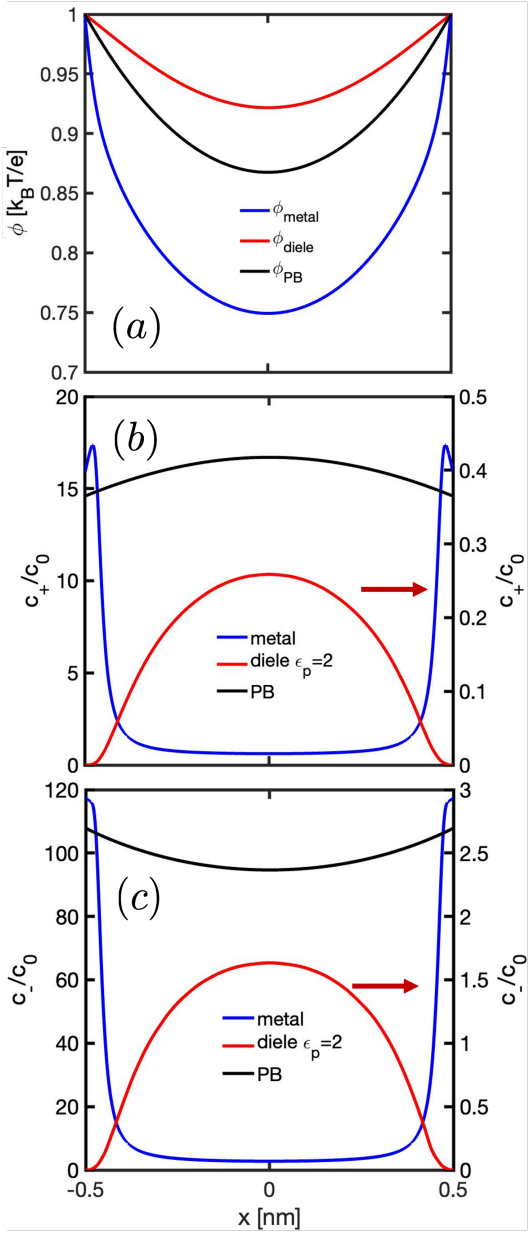

Figure 4.5: Symmetrically charged slit pore of 1 nm with both plates at fixed surface potentials $V_L = V_R = 1$. Bulk ion concentrations are $c_{0,+} = c_{0,-} = 0.1$ M. The implicit solvent has dielectric constant $\epsilon_r = 80$. (a) Electric potential profiles for the metal BCs (blue solid), dielectric (red solid) BCs, and PB theory (black dashed). (b) Cation profiles with metal BCs (blue, left y-axis), dielectric BCs (red, right y-axis) and PB theory (black, right y-axis). (c) Anion profiles: legends and axes are the same as in (b).

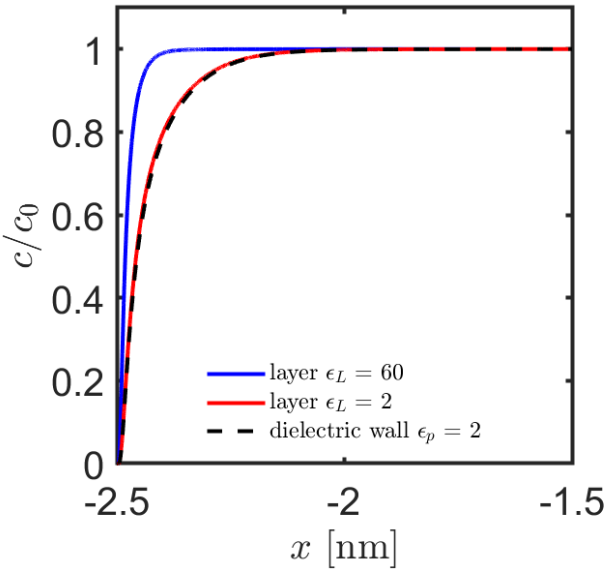

Figure 4.6: Ion concentration versus distance from a single metal wall at fixed surface potential $V = 0$ with a dielectric surface layer. The dielectric layer has size $a = 0.1$ nm and dielectric constant $\epsilon_{\mathrm{L}} = 60$ (blue) or $\epsilon_{\mathrm{L}} = 2$ (red). The bulk ion concentrations are $c_{0,+} = c_{0,-} = 0.1$ M. For comparison, the ion concentration near a dielectric wall ($\epsilon_{\mathrm{p}} = 2$) with no layer is shown in black. The implicit solvent has dielectric constant $\epsilon_{\mathrm{r}} = 80$.

as shown in Fig. 4.3. For metal BC (blue line), the image charge attraction is not fully screened at the middle point so that $c(x = 0)/c_0 \approx 1.27 > 1$. This is more clearly shown in the inset where the blue line does not reach 10^0 and is not flat in the middle. For dielectric BC (red line), the image charge repulsion leads to ion depletion in the entire slit, as shown by the right y-axis of Fig. 4.3(b), and the middle point concentration is significantly reduced from the bulk value. We note that since the image charge is a boundary layer effect, the electric double layer structure will look similar to the single wall case for plate separations > 2 nm.

We now examine the double layer structure when a weak but non-zero electric potential is maintained at the boundary surface(s). Fig. 4.4 shows the ion concentrations and electric potential profiles near a single wall fixed at $V = 1$. The bulk ion concentrations are $c_{+,0} = c_{-,0} = 0.1$ M. The electric potential profiles for all three boundary conditions are deceptively similar everywhere, as shown by the solid lines corresponding to the left y-axis of Fig. 3(a). However, the charge densities are different at a very short distance from the wall due to the drastic differences in self-energy, as shown by the dashed lines corresponding to the right y-axis of Fig. 4.4(a). Beyond the boundary layer, the three charge densities converge to the

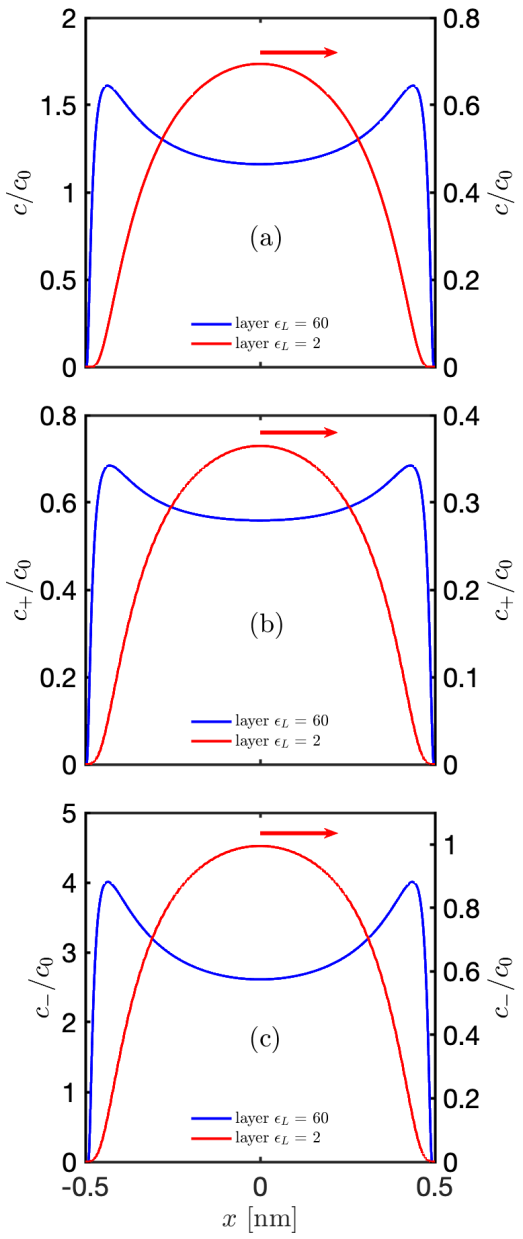

Figure 4.7: Ion concentration versus distance for a symmetrically charged slit pore of $L = 1$ nm. Both walls are metal with a dielectric layer of size $a = 0.1$ nm on each metal surface. The dielectric layer has dielectric constant $\epsilon_{\mathrm{L}} = 60$ (blue) or $\epsilon_{\mathrm{L}} = 2$ (red). The bulk ion concentrations are $c_{0,+} = c_{0,-} = 0.1$ M. The implicit solvent has dielectric constant $\epsilon_{\mathrm{r}} = 80$. (a) Applied potential $V = 0$. (b) Positive ion densities for applied potential $V = 1$. (c) Negative ion densities for applied potential $V = 1$.

same outer solution. The competition between the IC repulsion and attraction of anions to the positively-charged surface also leads to non-monotonic concentrations of anions for dielectric BC near the wall, as shown by the red line in Fig. 4.4(c).

For a slit pore, as its width decreases with the surface potential of both plates fixed at $V = 1$, the double layers from the two surfaces start to overlap. For this case, one can see the difference between the electric potentials of the different BCs as shown in Fig. 4.5(a). Overall, the concentration inside the slit pore is largest for metal BC and weakest for dielectric BC. This leads to a different magnitude of the screening effect, which mostly comes from the boundary layers. Going from the surface into the solution, for metal BC the electrostatic potential drops faster than the PB theory, whereas for dielectric BC, it drops slower than the PB theory. Compared to the single-wall case (Fig. 4.4(b) and (c)), the overlapping double layers and stronger IC effects in the 1 nm pore lead to two main differences: (1) the boundary layers for both the metal and dielectric BCs become thicker; (2) the anion concentration for dielectric BC increases monotonically from the boundary until the middle-point as shown in Fig. 4.5(b) and (c). For metal BC, the stronger IC attraction leads to a peak of cation concentration close to the wall, as shown in Fig. 4.4(b). Moreover, both cations and anions enrich near the surface for metal BC despite the positive applied potential.

Now, we turn to the case of a dielectric layer with dielectric constant ϵ_L on the metal surface that is lower than the dielectric constant of the solution. The dielectric layer generates a repulsive image charge that competes with the attractive image charge of the metal. This repulsive image charge is stronger with greater disparity between the layer and solution dielectric constant, and this effect is shown for a single planar boundary in Fig. 4.6. We see that the ion density completely depletes from the surface, meaning the repulsive IC from the layer overpowers the metal IC at all distances. For a layer with a low dielectric constant $\epsilon_L = 2$, the repulsive IC is so strong that the ion profile nearly matches that of a dielectric wall with the same dielectric constant, shown by the dashed line in Fig. 4.6.

Next, we examine the double-layer structure between two parallel metal plates with a dielectric layer on each surface, shown in Fig. 4.7. For no applied potential and $\epsilon_L = 60$ in Fig. 4.7(a), the ions adsorb in the pore due to the metal's attractive IC. However, the ions deplete close to the wall due to the layer's repulsive IC, giving a peak in the ion density profile. The layer prevents ion saturation at the metal wall previously seen in Fig. 4.3, yielding density profiles that qualitatively resemble

those of Refs. [37] and [39]. If the layer dielectric constant is low ($\epsilon_L = 2$), the ions completely deplete in the pore, similar to the profiles of the dielectric wall in Fig. 4.3, albeit with a higher maximum density due to the metal's attractive IC. For applied potential $V = 1$ in Fig. 4.7(b) and (c) at $\epsilon_L = 60$, the positive and negative ion density profiles are nonmonotonic for the same reasons as the zero-potential case.

Differential capacitance

We next examine the differential capacitance $C_d = d\sigma_s/dV$ for nanometer-sized slit pores. The two plates of the slit pore are at the same surface potential $\psi(z = \pm L/2) = V$ to simulate a nanoscale pore inside a porous electrode that is maintained at a constant potential.

In all three system conditions explored in Fig. 4.8, the initial capacitance (at very low voltage) of the metal BC is higher than the PB theory, dielectric BC, or layer BC. This is consistent with the qualitative understanding that metal BC image charge attraction significantly enhances charge separation, where charge separation refers to the difference in anion and cation densities as a function of position in the pore [39]. On the other hand, at weak electric potentials, the image charge repulsion of dielectric and layer BCs strongly depletes salt ions and reduces charge separation. As a result, the initial C_d is low. Moreover, since ions cannot closely approach the metal surface due to exclusion by the layer, the surface charge on the metal with a dielectric surface layer is less sensitive to the applied potential. This effect, combined with the layer's repulsive image charge, gives a lower capacitance than the other three cases for nearly all conditions. The only exception is at low salt concentration, small separation, and low applied potential in Fig. 4.8(c), where the layer capacitance slightly exceeds dielectric BC and PB theory. The reason is that, for very small separations, the attractive IC from the metal dominates the layer's repulsive IC, causing greater accumulation of ions in the pore compared to dielectric BC and PB theory.

At low bulk salt concentration $c_0 = 0.1$ M, and large separation between the plates ($L = 4$ nm, compared to the double layer thickness < 1 nm), the differential capacitance displays the "camel-shape" for dielectric and layer BCs, as well as PB theory [91], whereas that of the metal BC has a slight "bird shape" [80], as shown in Fig. 4.8(a). We note that the bird and camel shape come from the full-range capacitance, -5 to 5 kT/e, and the negative potential capacitance curve is just a

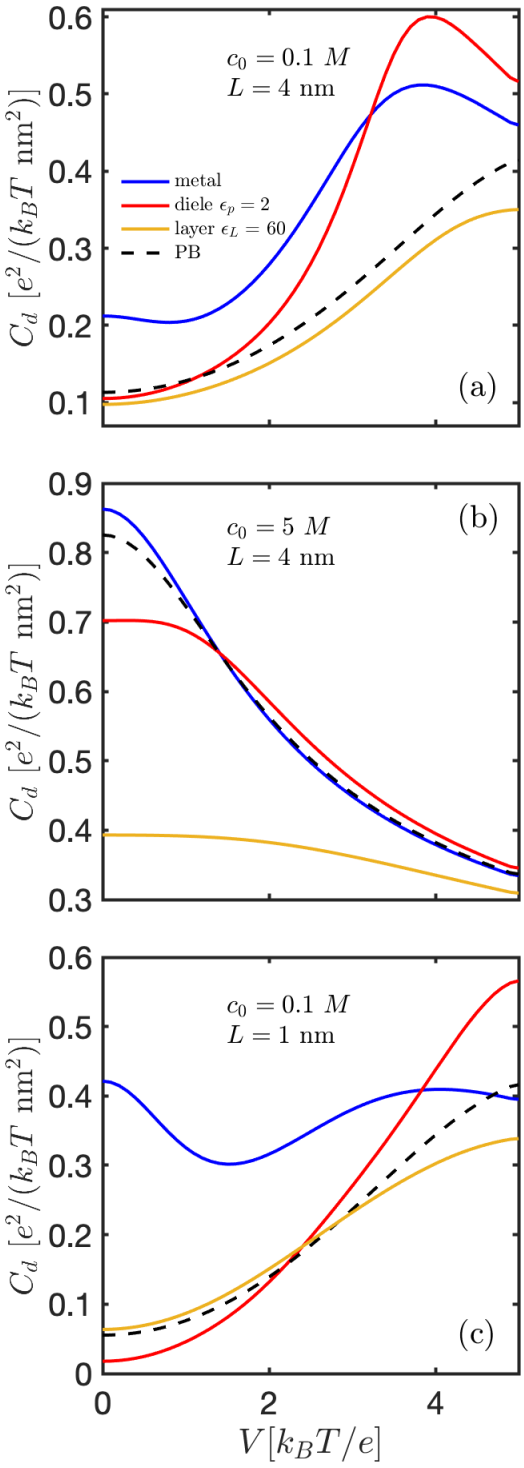

Figure 4.8: Differential capacitance curves for four cases: metal (blue), dielectric (red), and layer BCs (yellow), as well as PB theory (black). The capacitance curves are shown under conditions: (a) c_0 = 0.1 M, L = 4 nm. (b) c_0 = 5 M, L = 4 nm. (c) c_0 = 0.1 M, L = 1 nm.

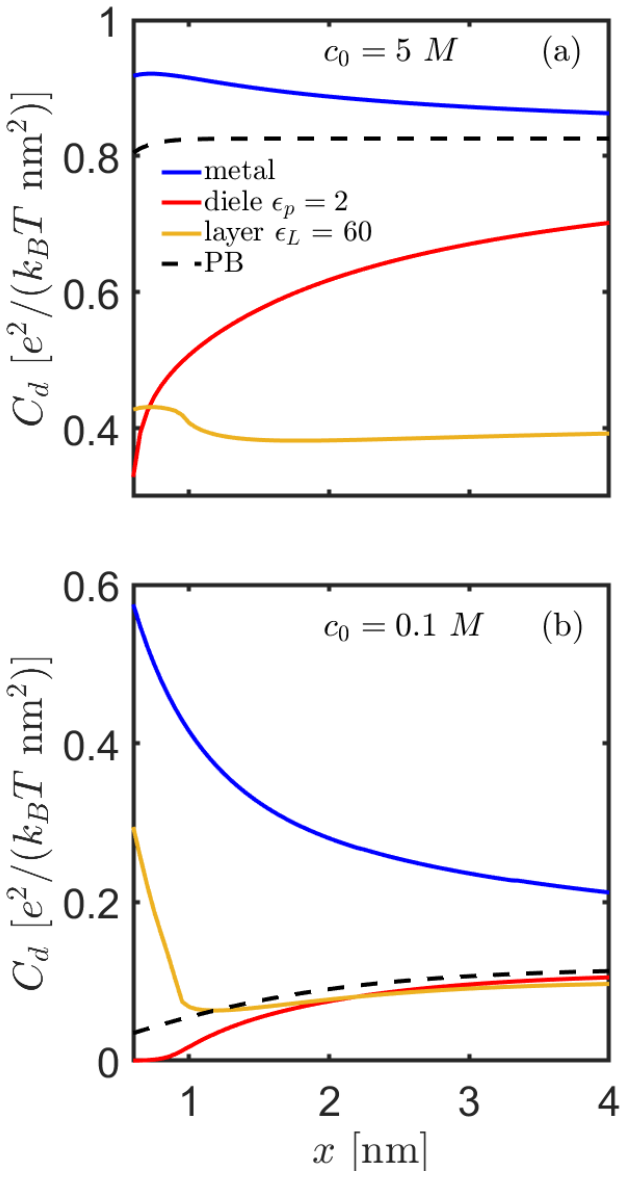

Figure 4.9: Differential capacitance curves for four cases: metal (blue), dielectric (red), and layer BCs (yellow), as well as PB theory (black) as a function of plate separation for $V = 0$. (a) Bulk ion concentration is $c_0 = 5$ M. (b) Bulk ion concentration is $c_0 = 0.1$ M.

reflection across the y axis since our system is symmetric. For the PB theory, this is due to the nonlinear dependence of charge density on the electric potential. For dielectric BC, as surface potential increases, the attraction of counter-ions to the positively-charged surface overcomes the image charge repulsion in the middle of the slit, flooding the pore with ions; therefore, the capacitance is enhanced greater than the metal BC. The same is true for the layer BC; however, since the surface charge on the metal with a dielectric surface layer is less sensitive to the applied voltage for reasons mentioned earlier, the capacitance never exceeds the PB result except for small separations with low applied potential and low bulk concentration.

It is known that the overestimation of surface ion density in the Gouy–Chapman theory leads to a differential capacitance curve that is always "camel-shaped," with a minimum at 0 applied voltage. Kornyshev [91] pointed out that the "lattice saturation" effect [92, 93], which accounts for finite ion sizes, can explain the observed deviations from the Gouy–Chapman theory, i.e., a "bell" shaped capacitance curve for room temperature ionic liquids [94]. Fig. 4.8(b) shows this scenario with a high bulk salt concentration $c_0 = 5$ M, and large separation $L = 4$ nm. The solvent concentration is only $c_s \approx 3.33$ M in the bulk reservoir, lower than the ion concentrations, as in a 'water-in-salt' electrolyte. At small voltage, initial charge separation is enhanced due to the large number of salt ions in the slit, giving a large C_d. Then, as the electric potential increases, the double layer saturates quickly, regardless of the BC. Thus, the overall C_d displays a bell shape for all four cases. These results are consistent with previous studies [91, 95–97]. Moreover, all curves converge at high applied potential due to double-layer saturation. We expect this convergence to occur for sufficiently high potential under the conditions for Fig. 4.8(a) and (c) as well. Similar to the modified PB theory, the ion-saturation effect plays a key role to render the bell shaped curves.

The more interesting regime is at low bulk salt concentration $c_0 = 0.1$ M and very small separation $L = 1.0$ nm. In this case, the boundary accumulation / depletion layers are very strong and dictate the charging behaviors at low surface potentials. Specifically, the IC attraction of metal BC strongly enhances the charge separation, resulting in a high initial capacitance. But, as the voltage increases, the saturated boundary layers screen out the influence of the surface potential in the middle of the slit, as seen in Fig. 4.5. This leads to a small second peak of the blue solid line in Fig. 4.8(c), giving a "bird-shaped" capacitance curve. On the other hand, for the dielectric and layer BCs, the IC repulsion at small distance is too strong at weak

electric potential, so very few counter-ions migrate into the slit when the voltage increases initially. Hence, the low-voltage capacitance is quite low for the dielectric and layer BCs. Additionally, the linear response regime is much smaller for metal BC under low bulk salt and small separation compared to dielectric and layer BCs. The reason for this is that the charge fluctuation in the metal is much higher under these conditions, causing significant deviations from the linear response capacitance even at low applied potentials.

Lastly, we investigate the capacitance as a function of plate separation at $V = 0$ for two bulk ion concentrations $c_0 = 5$ and 0.1 M, shown in Fig. 4.9 (a) and (b), respectively. At both concentrations, we see that the metal capacitance exceeds PB theory due to the attractive metal IC. Moreover, the metal capacitance increases as the pore size decreases, with an anomalously large increase for $c_0 = 0.1$ M compared to PB theory, similar to the results shown in Ref. [44]. For a dielectric boundary, the capacitance is lower than PB theory for both concentrations due to ion depletion in the pore caused by the dielectric wall's repulsive IC. For the layer BC in both cases, the capacitance is initially high due to the metal's attractive IC dominating at strong confinement. However, as the plates move apart, the capacitance decreases due to the layer's repulsive IC overtaking the attractive IC from the metal, causing ions to deplete in the pore. This effect creates a minimum in the capacitance. For large separations (> 1.5) nm, the layer's repulsive IC has a weaker effect since it is a boundary layer effect, so the capacitance gradually increases.

Force between like-charged plates

Finally, we investigate the forces between two symmetrically charged plates. In reality, it is more natural to control surface charge density for dielectric plates, or to maintain constant surface electric potential for metal plates, especially if the surface geometry is not simple. For ease of conceptual comparison, we also present results for dielectric BC with fixed surface potentials. In Fig. 4.10 (a), we investigate three surface charges $\sigma = 0.01, 0.02, 0.05$ /nm^2 at bulk concentration $c_0 = 0.1$ M (blue, black, and red curves, respectively). For lower surface charge $\sigma = 0.01$ /nm^2, the image charge contribution to the free energy for dielectric BC results in an attractive potential well. There is also a small but noticeable repulsive regime for plate separations between 1∼2 nm, which is consistent with the findings of Ref. [23], although there it was computed using a WKB approximation. At higher surface charge $\sigma = 0.05$ /nm^2, the same-charge repulsion overcomes the IC effect. Moreover, for $c_0 = 0.1$ M, the attractive well gradually disappears and completely

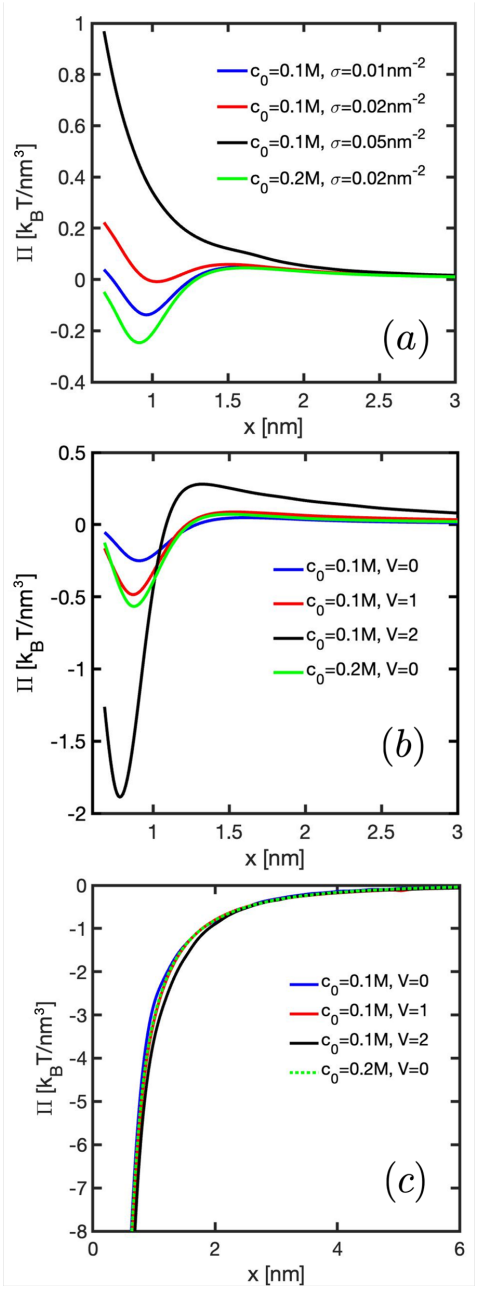

Figure 4.10: Force between neutral and like-charged plates with different material boundaries. In all plots the bulk concentrations are colored by: $c_0 = 0.1$ M (blue, red and black) and $c_0 = 0.2$ M (green). (a) Two dielectric plates with same surface charge densities. Surface charge densities are $\sigma = 0.01, 0.02, 0.05$ /nm^2 for the blue, red, and black line, respectively, and $\sigma = 0.02$ /nm^2 for the green line. (b) Two dielectric plates with the same fixed surface potentials. The surface potentials are $V = 0, 1, 2\ kT/e$ for the blue, red, and black line, respectively, and $V = 0\ kT/e$ for the green line. (c) Two metal plates with the same fixed surface potentials. The surface potentials are $V = 0, 1, 2\ kT/e$ for the blue, red, and black line, respectively, and $V = 0\ kT/e$ for the green line.

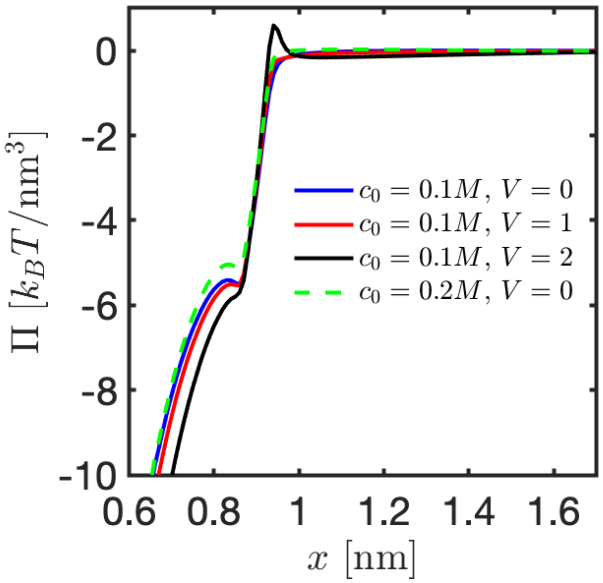

Figure 4.11: Force between neutral and like-charged metal plates with a 0.1 nm thick dielectric layer with dielectric constant $\epsilon_{\mathrm{L}} = 60$ on each plate. The metal plates have fixed surface potentials of either $V = 0, 1, 2\ kT/e$. The blue, red, and black curves have bulk ion concentration $c_0 = 0.1$ M, and the green curve has bulk ion concentration $c_0 = 0.2$ M.

vanishes when increasing the surface charge from 0.01 to 0.05 /nm^2 in Fig. 4.10 (a). Moving to the effect of bulk concentration, the green curve is for a fixed surface charge $\sigma = 0.02$ /nm^2 with bulk concentration $c_0 = 0.2$ M. Comparing the green curve to the red curve, it is obvious that the higher bulk concentration leads to a attraction at the same surface charge density. This is also qualitatively consistent with Ref. [23, 73]. However, when the boundary condition is changed to fixed surface potentials, the purely repulsive regime is no longer observed for reasonably weak applied potentials, as shown in Fig. 4.10(b). Even for neutral surfaces ($V = 0$ kT/e), there is attraction between plates, consistent with findings from a previous calculation from liquid-state theory [98]. The repulsion at short distance in Fig. 4.10(a) comes from the strong repulsion between the fixed surface charges, while in Fig. 4.10(b) the surface charges adjust to avoid strong repulsion and to lower the total free energy. At fixed surface potential, both higher surface potential (black line) and higher bulk salt concentration (green line) amplify the variation in the force, as the IC contribution to the free energy is enhanced.

In the case of metal BC, the IC attraction is very strong and dominates the interplate force. This is shown by Fig. 4.10(c), where the magnitude of the attraction is much

larger than in Fig. 4.10(b). In addition, no repulsive regime is observed and the attractive force decays over a longer length scale. Recall that we use point-charge model throughout the calculations here for consistency and fair comparisons. This means that ions can approach the boundaries infinitely close. For dielectric BC, the IC repulsion self-regulates this effect by suppressing the ion distributions at the surface. However, for metal BC, the IC attraction results in high concentration of counter-ions at the surface close to the saturation concentration, with a very large self-energy. As a result the attraction force computed here at short separations between the two electrodes may be overestimated compared with experimental or simulation results with finite ion sizes. For this reason, we introduce the thin dielectric layer to the metal surfaces to account for the distance of closest approach for ions, which we discuss next.

To finish, we investigate the effect of a 0.1 nm thick dielectric layer (dielectric constant $\epsilon_L = 60$) on metal plates, where the metal plates are at the same fixed potential. In Fig. 4.11, we see that the layer's repulsive IC cancels the metal's attractive IC for separations > 1 nm, preventing the plates from interacting until close separation (< 1) nm for all conditions considered. Consequently, the length scale of interaction between plates with layer BC is much smaller than that of metal and dielectric BCs. Moreover, at separations of 1 nm and above, the ions are depleted from the walls. As the plates move from 1 nm to 0.9 nm spacing, the metal's attractive IC overcomes the repulsive IC from the layer, causing ions to flood into the pore that generates an attractive force between the plates. Furthermore, the peak in the $V = 2$ curve stems from a stronger flooding of ions into the pore compared to the lower potentials. The slight bump in the force curves near 0.85 nm separation is due to the ions saturating the pore walls.

4.3 Conclusions

In this work, we discuss the image charge effect and its consequences in nano-capacitors and forces between like-charged plates. We treat the IC effects non-perturbatively for a point-charge model, based on a renormalized Gaussian fluctuation theory. We apply the incompressibility condition to account for the excluded volume interactions between the ions and solvent and to prevent the ion density from diverging at the interfaces. We obtain full numerical solutions to the renormalized field theory subject to different boundary conditions. We focus on a comparison of these calculations under the (1) perfectly conducting metal plates, (2) dielectric plates, (3) metal plates with a thin dielectric layer, and (4) the PB theory. We

demonstrate these comparisons using a simple 1:1 electrolyte with equal volumes of all species. IC effects with asymmetric valences or sizes can be readily incorporated in future works.

We first show that the double-layer structures are significantly affected by the IC interaction. For a single surface without applied voltage or externally-imposed surface charge, IC leads to saturation of ions at the surface for the metal BC, and strong ion depletion for the dielectric and layer BCs. For the layer BC, the depletion strengthens with lower dielectric constant relative to the solvent. For a narrow slit pore, the middle-point concentrations significantly deviate from the bulk values due to IC. When a single surface is fixed at a weak applied potential, the electrostatic potential profiles are not sensitive to the BCs. However, ion densities near the surface depends strongly on the type of BC applied. For a narrow slit pore with both surfaces at a weak fixed potential, both the ion density and the electrostatic potential profiles are strongly affected by the BCs. Moreover, the layer BC gives nonmonotonic ion density profiles that are qualitatively similar to those observed in MD simulations [39].

Based on the understanding about the double-layer structures, our calculations further show that the boundary layers due to IC interaction lead to significant differences in the differential capacitance of a nano-pore under different boundary conditions. The dielectric and layer BCs show a qualitatively similar trend with the PB theory, where the capacitance curve changes from a camel shape to a bell shape as bulk salt concentration increases. Moreover, the metal BC gives a "bird-shaped" capacitance at low bulk ion concentrations and small pore width due to IC-induced boundary layer accumulation and ion saturation. The layer BC shows that the ion exclusion near the metal surface combined with the repulsive IC yields a lower capacitance than PB, metal, or dielectric BCs at nearly all conditions. Notice that modified PB treatment [44] only accounts for the IC from the mean-charge density $\rho = c_+ - c_-$ in the Poisson equation, while our treatment captures the IC effect even at $\rho = 0$, and the ion density profiles c_+ and c_- are non-uniform. As a result, our predictions of the capacitance are different from the modified PB treatment, especially at weak applied potential.

The differences between the BCs are also manifested in the forces between like-charged planar walls. For dielectric BC, at fixed surface charge density, the attraction well gradually diminishes as surface charge increases; at fixed surface potential, the attraction well is stronger at higher potential values. For metal BC with fixed

surface potentials on both plates, which is more directly relevant to nano-pores inside porous electrodes, the attraction is much stronger than the dielectric BC and decays slower; no repulsion is observed in this ensemble in the weak-coupling regime. Increasing either surface potential or bulk concentration slightly enhances the attraction force. The prediction of pure attraction for planar metal plates is different from the nonlinear PB theory, which only gives repulsion between like-charged metal plates—Ref. [74] showed that in the PB theory, one has to invoke curvature effects to induce like-charge attraction with metal BC. For layer BC at fixed surface potentials, the interaction length scale is much smaller than that of metal or dielectric BCs due to the layer's repulsive IC canceling the metal's attractive IC at separations > 1 nm. For separations < 1 nm, the plates are strongly attractive, similar to the metal BC, due to ions flooding the pore at close separation when the metal IC overcomes the layer's repulsive IC. Further modifications of the boundary conditions such as surface charge regulation [99, 100] or multi-layered interfaces [101] are expected to mediate the above results and can be readily incorporated into the same framework.

Our work presents a fundamental perspective on the IC interaction, highlighting its non-negligible influence on double layer structures, and consequently, nanoscale capacitors and forces between like-charged plates. These effects are often omitted or treated in a mean-field fashion. However, we show that even at zero mean-charge density, where mean-field predictions will neglect IC, it still has a strong effect. Our results provide a starting point to include IC in various realistic applications.

4.A Brief Summary of the Key Equations

Most of the derivations were already presented in Ref. [22] and earlier references cited there. Here we sketch the outline of the derivations, including the incompressibility constraint, for the reader's convenience. We start with the Hamiltonian in SI unit

$$H = \int d\mathbf{r} d\mathbf{r}' \frac{e^2}{2} \rho(\mathbf{r}) G_0(\mathbf{r}, \mathbf{r}') \rho(\mathbf{r}') \tag{4.31}$$

where the Coulomb operator is defined by

$$-\nabla \cdot \varepsilon \nabla' G_0(\mathbf{r}, \mathbf{r}') = \delta(\mathbf{r} - \mathbf{r}'). \tag{4.32}$$

The total charge density can be decomposed into external charge, cations and anions

$$\rho(\mathbf{r}) = \rho_{ex}(\mathbf{r}) + z_+ \sum_{i+} h_+(\mathbf{r} - \mathbf{r}_+^i) - z_- \sum_{j-} h_-(\mathbf{r} - \mathbf{r}_-^j) \tag{4.33}$$

where $h_\pm$ represents the spread shape of ion charge. The incompressibility of the liquid requires

$$\hat{c}_{tot} = \hat{c}_+(\mathbf{r}) + \hat{c}_-(\mathbf{r}) + \hat{c}_s(\mathbf{r}) = 1/v_0 \tag{4.34}$$

where the density of species

$$\begin{aligned} \hat{c}_+(\mathbf{r}) &= \sum_{i+} h_+(\mathbf{r} - \mathbf{r}_+^i) \\ \hat{c}_-(\mathbf{r}) &= \sum_{i-} h_-(\mathbf{r} - \mathbf{r}_-^i) \\ \hat{c}_s(\mathbf{r}) &= \sum_{s-} h_s(\mathbf{r} - \mathbf{r}_s^i) \end{aligned} \tag{4.35}$$

subscript s stands for solvent.

The canonical partition function is

$$\begin{aligned} Q =& \frac{1}{n_+!n_-!n_s!v_+^{n_+}v_-^{n_-}v_s^{n_s}} \int d\mathbf{r}_{i+}d\mathbf{r}_{j-}d\mathbf{r}_s e^{-\beta H} \prod_r \delta\left(\hat{c}_{tot} - 1/v_0\right) \\ =& \frac{1}{n_+!n_-!n_s!v_+^{n_+}v_-^{n_-}v_s^{n_s}} \int d\mathbf{r}_{i+}d\mathbf{r}_{j-}d\mathbf{r}_s \\ & \times e^{-\beta\frac{e^2}{2}\int d\mathbf{r}d\mathbf{r}'(\rho_{ex}+\rho_{ion})(\mathbf{r})G_0(\mathbf{r},\mathbf{r}')(\rho_{ex}+\rho_{ion})(\mathbf{r}')} \\ & \times \int dc_{\pm,s} \int D[\eta] e^{i\int d\mathbf{r}\eta(\mathbf{r})(c_++c_-+c_s-1/v_0)(\mathbf{r})} \\ & \times \int dw_{\pm,s} e^{i\int d\mathbf{r}[w_+(\hat{c}_+-c_+)+w_-(\hat{c}_--c_-)+w_s(\hat{c}_s-c_s)]} \end{aligned} \tag{4.36}$$

where auxiliary fields $w_{\pm,s}$ are also introduced. In general, if there are other quadratic or higher-order interaction terms involving the concentrations, it will be useful to deal with the w fields instead of directly manipulating the concentration operators. Using the Hubbard-Stratonovich transform

$$\int dx \exp\left(-\frac{1}{2}x^T A^{-1} x \pm ixy\right) = \sqrt{\det(A)} \exp\left(-\frac{1}{2}y^T A y\right) \tag{4.37}$$

the exponential factor is

$$
\begin{aligned}
&e^{-\beta\frac{e^2}{2}\int d\mathbf{r}d\mathbf{r}'\rho(\mathbf{r})G_0(\mathbf{r},\mathbf{r}')\rho(\mathbf{r}')} \\
&= \frac{1}{\sqrt{\det(G_0)}}\int D[\phi]e^{-\int d\mathbf{r}d\mathbf{r}'\left(\frac{1}{8\pi\ell_B}\nabla\phi(\mathbf{r})\cdot\nabla'\phi(\mathbf{r}')+i\rho(\mathbf{r})\phi(\mathbf{r}')\right)\delta(\mathbf{r}-\mathbf{r}')}
\end{aligned}
\tag{4.38}
$$

here $\ell_B = e^2/(4\pi\epsilon k_B T)$ is the Bjerrum length and ϕ is the dimensionless potential scaled by $\frac{k_B T}{e}$.

Now the grand partition function is

$$
\Xi = \sum_{n_+}\sum_{n_-}\sum_{n_s}\frac{Qe^{n_+\mu_+}e^{n_-\mu_-}e^{n_s\mu_s}}{\sqrt{\det(G_0)}}\int D[\phi]D[\eta]dw_{\pm,s}dc_{\pm,s}e^{-\mathcal{L}} \tag{4.39}
$$

where the action is

$$
\begin{aligned}
\mathcal{L} = &\int d\mathbf{r}d\mathbf{r}'\left[\frac{1}{8\pi\ell_B}\nabla\phi(\mathbf{r})\cdot\nabla'\phi(\mathbf{r}')+i\rho_{ex}(\mathbf{r})\phi\mathbf{r}')\right]\delta(\mathbf{r}-\mathbf{r}') \\
&-\int d\mathbf{r}\left(\lambda_+e^{-i(h_+*[z_+\phi+iw_+])(\mathbf{r})}+\lambda_-e^{i(h_-*[z_-\phi-iw_-])(\mathbf{r})}\right) \\
&+\int d\mathbf{r}\left(w_+c_++w_-c_-+w_sc_s-\eta(c_++c_-+c_s-1/v_0)\right) \\
&-\int d\mathbf{r}\lambda_se^{h_s*w_s}
\end{aligned}
\tag{4.40}
$$

$*$ stands for the convolution operator

$$
(h*\phi)(\mathbf{r}) = \int d\mathbf{r}'h(\mathbf{r}'-\mathbf{r})\phi(\mathbf{r}') \tag{4.41}
$$

and $\lambda_\pm = \frac{e^{\mu_\pm}}{v_\pm}$ is the fugacity.

The variational approach decomposes the field $\phi = -i\psi+\chi$, and the action becomes

$$
\begin{aligned}
\mathcal{L}[\phi] = &\int d\mathbf{r} \left\{ \frac{1}{8\pi\ell_B} \left(\nabla\left(-i\psi(\mathbf{r}) + \chi(\mathbf{r})\right)\right)^2 + \rho_{ex}(\mathbf{r})(-i\psi(\mathbf{r}) + \chi(\mathbf{r})) \right\} \\
&- \int d\mathbf{r} \lambda_+ e^{-z_+(h_+ * \psi)(\mathbf{r}) + (h_+ * w_+)(\mathbf{r}) - i z_+ (h_+ * \chi)(\mathbf{r})} \\
&- \int d\mathbf{r} \lambda_- e^{z_-(h_- * \psi)(\mathbf{r}) + (h_- * w_-)(\mathbf{r}) + i z_- (h_- * \chi)(\mathbf{r})} \\
&+ \int d\mathbf{r} \left(w_+ c_+ + w_- c_- + w_s c_s - \eta(c_+ + c_- + c_s - 1/v_0)\right) \\
&- \int d\mathbf{r} \lambda_s e^{h_s * w_s}.
\end{aligned}
\tag{4.42}
$$

The average number (density) of ions is

$$
\begin{aligned}
\langle n_\pm \rangle = \frac{\partial \ln \Xi}{\partial \mu_\pm} = \int d\mathbf{r} \lambda_\pm \left\langle e^{\mp z_\pm (h_\pm * (\psi + i\chi))(\mathbf{r}) + (h_\pm * w_\pm)(\mathbf{r})} \right\rangle \\
c_\pm(\mathbf{r}) = \lambda_\pm \left\langle e^{\mp z_\pm (h_\pm * (\psi + i\chi))(\mathbf{r}) + (h_\pm * w_\pm)(\mathbf{r})} \right\rangle .
\end{aligned}
\tag{4.43}
$$

For the variational renormalization, a Gaussian reference action is chosen

$$
\mathcal{L}_{ref} = \int d\mathbf{r} d\mathbf{r}' \frac{1}{2} \chi(\mathbf{r}) G^{-1}(\mathbf{r}, \mathbf{r}') \chi(\mathbf{r}')
\tag{4.44}
$$

and the extremized free energy is

$$
\begin{aligned}
W =& W_{ref} + \left\langle \mathcal{L}[\phi] - \mathcal{L}_{ref}[\phi] \right\rangle_{ref} \\
=& -\frac{1}{2} \ln \left(\frac{\det(G)}{\det(G_0)} \right) + \langle L[\phi] \rangle_{ref} - \frac{1}{2}.
\end{aligned}
\tag{4.45}
$$

To evaluate $\langle \mathcal{L}[\phi] \rangle_{ref}$, we note that

$$
\begin{aligned}
&\left\langle \int d\mathbf{r} d\mathbf{r}' \frac{1}{4\pi\ell_B(\mathbf{r})} \delta(\mathbf{r} - \mathbf{r}') \nabla\chi(\mathbf{r}) \cdot \nabla'\chi(\mathbf{r}') \right\rangle_{ref} \\
&= \int d\mathbf{r} d\mathbf{r}' \left\{ \langle \chi(\mathbf{r}) \chi(\mathbf{r}') \rangle_{ref} \nabla \left[\frac{1}{4\pi\ell_B(\mathbf{r})} \right] \cdot \nabla' \delta(\mathbf{r} - \mathbf{r}') \right\} \\
&= \int d\mathbf{r} d\mathbf{r}' \left\{ G(\mathbf{r}, \mathbf{r}') \nabla \left[\frac{1}{4\pi\ell_B(\mathbf{r})} \right] \cdot \nabla' \delta(\mathbf{r} - \mathbf{r}') \right\}
\end{aligned}
\tag{4.46}
$$

and

$$\left\langle e^{\mp i z_\pm (h_\pm * \chi)(\mathbf{r})} \right\rangle_{ref} = e^{-\frac{1}{2} z_\pm^2 \int d\mathbf{y} d\mathbf{y}' h_\pm(\mathbf{y}-\mathbf{r}) G(\mathbf{y},\mathbf{y}') h_\pm(\mathbf{y}'-\mathbf{r})}. \tag{4.47}$$

Now we can simplify the averaged action as

$$\begin{aligned}\langle \mathcal{L}[\psi] \rangle_{ref} = \int dr \left\{ -\frac{1}{8\pi\ell_B} (\nabla\psi(\mathbf{r}))^2 + \rho_{ex}(\mathbf{r})\psi(\mathbf{r}) - c_\pm(\mathbf{r}) \right\} \\ + \frac{1}{2} \int dr dr' G(\mathbf{r},\mathbf{r}') \nabla \cdot \left[\frac{1}{4\pi\ell_B(\mathbf{r})} \right] \nabla' \delta(\mathbf{r}-\mathbf{r}') \\ + \int d\mathbf{r} \left(w_+ c_+ + w_- c_- + w_s c_s - \eta(c_+ + c_- + c_s - 1/v_0) \right) \\ - \int d\mathbf{r} \lambda_s e^{h_s * w_s}. \end{aligned} \tag{4.48}$$

The Euler-Lagrange equations in the main text for this field theory then result from variational derivatives of W with respect to ψ, G, $w_{\pm,s}$, $c_{\pm,s}$ and η.

4.B Image Charge of a Single Point Charge Near Layered Interfaces

Metal-dielectric interface

Suppose for half space $z < 0$, it is a metal plate. For half space $z > a$, it is a dielectric medium with relative permittivity ϵ_2. In between $0 < z < a$ it is another dielectric with ϵ_1. A point charge q is placed at $(0, 0, a + b)$. We now solve for the potential inside the two dielectric media ϕ_1 and $\phi_2 + \phi_3$. Due to cylindrical symmetry, the Poisson equation can be written as

$$\begin{aligned} \left(\partial_z^2 + \frac{1}{r}\partial_r r \partial_r + \frac{1}{r^2}\partial_\theta^2 \right) \phi_i = 0 \qquad i = 1, 2 \\ \phi_3 = \frac{eq}{4\pi\epsilon_0\epsilon_2 \sqrt{r^2 + [z-(a+b)]^2}}. \end{aligned} \tag{4.49}$$

Nondimensionalize by the Bjerrum length in the liquid

$$\ell_B = \frac{e^2}{4\pi\epsilon_0\epsilon_2 k_B T} \tag{4.50}$$

$$\psi = \frac{e\phi}{k_B T} = \frac{q\ell_B}{\sqrt{r^2 + [z-(a+b)]^2}}. \tag{4.51}$$

For water $\epsilon_2 = 80$, $\ell_B \sim 0.7$ nm.

On the metal-dielectric interface $z = a$, the boundary conditions are

$$\begin{aligned} \epsilon_1 \partial_z \phi_1(r,\theta,a) &= \epsilon_2 \partial_z \left(\phi_2(r,\theta,a) + \phi_3(r,\theta,a)\right) \\ \phi_1(r,\theta,a) &= \phi_2(r,\theta,a) + \phi_3(r,\theta,a). \end{aligned} \tag{4.52}$$

The second condition implies already the continuity of the tangential E field

$$\partial_r \phi_1(r,\theta,a) = \partial_r \left(\phi_2(r,\theta,a) + \phi_3(r,\theta,a)\right). \tag{4.53}$$

At $z = 0$,

$$\phi_1(r,\theta,0) = 0. \tag{4.54}$$

At $z \to \infty$,

$$\phi_2(r,\theta,\infty) = 0. \tag{4.55}$$

The general solution satisfying BCs Eq. 4.54 and Eq. 4.55

$$\begin{aligned} \phi_1 &= \int_0^\infty d\lambda \sinh(\lambda z) J_0(\lambda r) f_1(\lambda) \\ \phi_2 &= \int_0^\infty d\lambda e^{-\lambda z} J_0(\lambda r) f_2(\lambda). \end{aligned} \tag{4.56}$$

Then one uses the fact

$$\frac{1}{\sqrt{r^2 + (z-a-b)^2}} = \int_0^\infty d\lambda J_0(\lambda r) e^{-\lambda |z-a-b|}. \tag{4.57}$$

To match the BC at $z = a$

$$\begin{aligned} q\epsilon_2 e^{-\lambda b} &= f_1(\lambda)\epsilon_1 \cosh(a\lambda) + f_2(\lambda)\epsilon_2 e^{-\lambda a} \\ q e^{-\lambda b} &= f_1(\lambda) \sinh(a\lambda) - f_2(\lambda) e^{-\lambda a}. \end{aligned} \tag{4.58}$$

As a result,

$$
\begin{aligned}
f_1(\lambda) &= \frac{2\epsilon_2 q e^{-\lambda b}}{\epsilon_1 \cosh(\lambda a) + \epsilon_2 \sinh(\lambda a)} \\
f_2(\lambda) &= q \frac{\epsilon_2 \sinh(\lambda a) - \epsilon_1 \cosh(\lambda a)}{\epsilon_1 \cosh(\lambda a) + \epsilon_2 \sinh(\lambda a)} e^{\lambda(a-b)}.
\end{aligned} \tag{4.59}
$$

For the IC force, at $z = a_{+0}$, the excess E field is

$$
\begin{aligned}
E_r &= -\int_0^\infty d\lambda e^{-\lambda a} \lambda J_0'(\lambda r) f_2(\lambda) \\
&= \int_0^\infty d\lambda e^{-\lambda a} \lambda J_1(\lambda r) f_2(\lambda) \\
E_z &= \int_0^\infty d\lambda e^{-\lambda a} \lambda J_0(\lambda r) f_2(\lambda)
\end{aligned} \tag{4.60}
$$

in addition to the E field generated by the point charge potential ϕ_3.

The surface charge density $\sigma(z = a)$ on the interface at $z = a$ can be extracted by the difference of the E field

$$
E_z(z = a + 0) - E_z(z = a - 0) = \sigma(z = a) \left(\frac{1}{\epsilon_1} + \frac{1}{\epsilon_2} \right). \tag{4.61}
$$

Similarly, for the surface charge density $\sigma(z = 0)$, we have

$$
\sigma(z = 0) = \epsilon_1 E_z(z = 0 + 0). \tag{4.62}
$$

4.C IC with a Dielectric Surface Layer

Suppose $z > 0$ half space is filled by the electrolyte solution with dielectric constant ϵ_r, while $-a < z < 0$ is a dielectric layer with ϵ_{L}.

The BC for Poisson equation with fixed surface potentials is a Robin type

$$
\epsilon_{\mathrm{L}} \phi(0) - \epsilon_r a \phi'(0) = \epsilon_{\mathrm{L}} V_1. \tag{4.63}
$$

For another layer at $L < z < L + a$, we have similarly

$$
\epsilon_{\mathrm{L}} \phi(L) + \epsilon_r a \phi'(L) = \epsilon_{\mathrm{L}} V_2. \tag{4.64}
$$

For fixed surface charge $e\sigma_S$ at $z = -a$, the BC at $z = 0$ is still a Neumann BC

$$e\sigma_S = -\epsilon_{\mathrm{L}}\phi'_{\mathrm{L}}(0) = -\epsilon_r\phi'_r(0). \tag{4.65}$$

For the self-energy Green's function, a Robin type BC now applies to both metal and dielectric plates at $z < -a$. For a dielectric plate with ϵ_p

$$G'(0) - k\frac{\epsilon_{\mathrm{L}}}{\epsilon_r}\frac{\epsilon_{\mathrm{L}}\sinh(ka) + \epsilon_p\cosh(ka)}{\epsilon_p\sinh(ka) + \epsilon_{\mathrm{L}}\cosh(ka)}G(0) = 0. \tag{4.66}$$

Taking the limit of $\epsilon_p \to \infty$, we have the BC for the metal plate

$$G'(0) - k\frac{\epsilon_{\mathrm{L}}}{\epsilon_r}\coth(ka)G(0) = 0. \tag{4.67}$$

References

(1) Wagner, C. *Phys. Z.* **1924**, *25*, 474–477.

(2) Onsager, L.; Samaras, N. N. *J. Chem. Phys.* **1934**, *2*, 528–536.

(3) Naji, A.; Jungblut, S.; Moreira, A. G.; Netz, R. R. *Phys. A: Stat. Mech. Appl.* **2005**, *352*, 131–170.

(4) Bakhshandeh, A.; Dos Santos, A. P.; Levin, Y. *Phys. Rev. Lett.* **2011**, *107*, 107801.

(5) Kjellander, R.; Marčelja, S. *Chem. Phys. Lett.* **1984**, *112*, 49–53.

(6) Lemay, S. G.; Kang, S.; Mathwig, K.; Singh, P. S. *Acc. Chem. Res.* **2013**, *46*, 369–377.

(7) Babel, S.; Eikerling, M.; Löwen, H. *J. Chem. Phys. C* **2018**, *122*, 21724–21734.

(8) Han, J.-W.; Seol, M.-L.; Moon, D.-I.; Hunter, G.; Meyyappan, M. *Nat. Electron.* **2019**, *2*, 405–411.

(9) Li, T.; Hu, W.; Zhu, D. *Adv. Mater.* **2010**, *22*, 286–300.

(10) Biesheuvel, P.; Porada, S.; Levi, M.; Bazant, M. Z. *J. Solid State Electrochem.* **2014**, *18*, 1365–1376.

(11) Comtet, J.; Nigués, A.; Kaiser, V., et al. *Nat. Mater.* **2017**, *16*, 634–639.

(12) Chao, H.; Wang, Z.-G. *J. Phys. Chem. Lett.* **2020**, *11*, 1767–1772.

(13) Zhou, T.; Mirzadeh, M.; Pellenq, R. J.-M.; Bazant, M. Z. *Phys. Rev. Fluids* **2020**, *5*, 124201.

(14) Steinpilz, T.; Joeris, K.; Jungmann, F., et al. *Nat. Phys.* **2020**, *16*, 225–229.

(15) Netz, R. R.; Orland, H. *Eur. Phys. J. E* **2000**, *1*, 203–214.

(16) Kanduč, M.; Podgornik, R. *Eur. Phys. J. E* **2007**, *23*, 265–274.

(17) Podgornik, R. *J. Chem. Phys.* **1989**, *91*, 5840–5849.

(18) Naji, A.; Kanduč, M.; Forsman, J.; Podgornik, R. *J. Chem. Phys.* **2013**, *139*, 150901.

(19) Lau, A.; Sokoloff, J. *Phys. Rev. E* **2020**, *102*, 052606.

(20) Solis, F.; de la Cruz, M. O. *J. Chem. Phys.* **2021**, *155*, 104703.

(21) Wang, R.; Wang, Z.-G. *Phys. Rev. Lett.* **2014**, *112*, 136101.

(22) Wang, Z.-G. *Phys. Rev. E* **2010**, *81*, 021501.

(23) Wang, R.; Wang, Z.-G. *J. Chem. Phys.* **2013**, *139*, 124702.

(24) Wang, R.; Wang, Z.-G. *J. Chem. Phys.* **2015**, *142*, 104705.

(25) Jiang, J.; Wang, Z.-G. *J. Chem. Phys.* **2018**, *148*, 114105.

(26) Podgornik, R.; Žekš, B. *J. Chem. Soc., Faraday Trans. 2* **1988**, *84*, 611–631.

(27) Dean, D. S.; Horgan, R. R. *Phys. Rev. E* **2004**, *69*, 061603.

(28) Siepmann, J. I.; Sprik, M. *J. Chem. Phys.* **1998**, *102*, 511.

(29) Reed, S. K.; Lanning, O. J.; Madden, P. A. *J. Chem. Phys.* **2007**, *126*, 084704.

(30) Limmer, D. T.; Merlet, C.; Salanne, M., et al. *Phys. Rev. Lett.* **2013**, *111*, 106102.

(31) Nguyen, T. D.; Li, H.; Bagchi, D.; Solis, F. J.; de la Cruz, M. O. *Comput. Phys. Commun.* **2019**, *241*, 80–91.

(32) Lin, Y.; Baumketner, A.; Deng, S., et al. *J. Chem. Phys.* **2009**, *131*, 10B608.

(33) Gan, Z.; Xu, Z. *Phys. Rev. E* **2011**, *84*, 016705.

(34) Xu, Z. *Phys. Rev. E* **2013**, *87*, 013307.

(35) Dos Santos, A. P.; Girotto, M.; Levin, Y. *J. Chem. Phys.* **2016**, *144*, 144103.

(36) Dwelle, K. A.; Willard, A. P. *J. Phys. Chem. C* **2019**, *123*, 24095–24103.

(37) Jing, Y.; Jadhao, V.; Zwanikken, J. W.; Olvera De La Cruz, M. *J. Chem. Phys.* **2015**, *143*, 194508, DOI: 10.1063/1.4935704.

(38) Dos Santos, A. P.; Girotto, M.; Levin, Y. *J. Chem. Phys.* **2017**, *147*, 184105.

(39) Son, C. Y.; Wang, Z.-G. *Proc. Natl. Acad. Sci. USA* **2021**, *118*.

(40) Mariappan, C.; Heins, T.; Roling, B. *Solid State Ion.* **2010**, *181*, 859–863.

(41) Rotenberg, B.; Salanne, M. *J. Phys. Chem. Lett.* **2015**, *6*, 4978–4985.

(42) Lee, A. A.; Perkin, S. *J. Phys. Chem. Lett.* **2016**, *7*, 2753–2757.

(43) Gao, X.; Gan, Z. *J. Chem Phys.* **2024**, *161*.

(44) Kondrat, S.; Georgi, N.; Fedorov, M. V.; Kornyshev, A. A. *Phys. Chem. Chem. Phys.* **2011**, *13*, 11359–11366.

(45) Kondrat, S.; Kornyshev, A. A., et al. *Phys. Rev. Lett.* **2014**, *113*, 048701.

(46) Bagchi, D.; Nguyen, T. D.; de la Cruz, M. O. *Proc. Natl. Acad. Sci. USA* **2020**, *117*, 19677–19684.

(47) Israelachvili, J. N., *Intermolecular and surface forces*; Academic press: 2015.

(48) Belloni, L. *J. Condens. Matter Phys.* **2000**, *12*, R549.

(49) Verwey, E. J. W.; Overbeek, J. T. G.; Van Nes, K., *Theory of the stability of lyophobic colloids: the interaction of sol particles having an electric double layer*; Elsevier Publishing Company: 1948.

(50) Trizac, E.; Levin, Y. *Phys. Rev. E* **2004**, *69*, 031403.

(51) Pianegonda, S.; Trizac, E.; Levin, Y. *J. Chem. Phys.* **2007**, *126*, 014702.

(52) Colla, T. E.; Levin, Y. *J. Chem. Phys.* **2010**, *133*, 234105.

(53) Colla, T. E.; dos Santos, A. P.; Levin, Y. *J. Chem. Phys.* **2012**, *136*, 194103.

(54) De Soria, M. I. G.; Álvarez, C. E.; Trizac, E. *Phys. Rev. E* **2016**, *94*, 042609.

(55) Trizac, E. *Phys. Rev. E* **2000**, *62*, R1465.

(56) Kjellander, R.; Marčelja, S.; Pashley, R.; Quirk, J. *J. Chem. Phys.* **1990**, *92*, 4399–4407.

(57) Bowen, W. R.; Sharif, A. O. *Nature* **1998**, *393*, 663–665.

(58) Gelbart, W. M.; Bruinsma, R. F.; Pincus, P. A.; Parsegian, V. A. *Phys. Today* **2000**, *53*, 38–45.

(59) Zhou, T.; Ioannidou, K.; Masoero, E., et al. *Langmuir* **2019**, *35*, 4397–4402.

(60) Zhou, T.; Ioannidou, K.; Ulm, F.-J.; Bazant, M. Z.; Pellenq, R.-M. *Proc. Natl. Acad. Sci. USA* **2019**, *116*, 10652–10657.

(61) Monfared, S.; Zhou, T.; Andrade, J. E., et al. *Phys. Rev. Lett.* **2020**, *125*, 255501.

(62) Kjellander, R.; Marcelja, S.; Pashley, R.; Quirk, J. *J. Phys. Chem.* **1988**, *92*, 6489–6492.

(63) Pellenq, R.-M.; Caillol, J.; Delville, A. *J. Phys. Chem. B* **1997**, *101*, 8584–8594.

(64) Pincus, P.; Safran, S. *Europhys. Lett.* **1998**, *42*, 103.

(65) Levin, Y. *Phys. A: Stat. Mech. Appl.* **1999**, *265*, 432–439.

(66) Linse, P.; Lobaskin, V. *Phys. Rev. Lett.* **1999**, *83*, 4208.

(67) Netz, R. R. *Eur. Phys. J. E* **2001**, *5*, 557–574.

(68) Pellenq, R. J.-M.; Van Damme, H. *Mrs Bulletin* **2004**, *29*, 319–323.

(69) Moreira, A. G.; Netz, R. R. *Europhys. Lett.* **2000**, *52*, 705.

(70) Moreira, A. G.; Netz, R. R. *Phys. Rev. Lett.* **2001**, *87*, 078301.

(71) Šamaj, L.; Trizac, E. *Phys. Rev. Lett.* **2011**, *106*, 078301.

(72) Šamaj, L.; Trizac, E. *Phys. Rev. E* **2011**, *84*, 041401.

(73) Liu, P.; Ma, M.; Xu, Z. *Commun. in Comput. Phys.* **2017**, *22*, 95–111.

(74) Dos Santos, A. P.; Levin, Y. *Phys. Rev. Lett.* **2019**, *122*, 248005.

(75) Jungwirth, P.; Tobias, D. J. *Chem. Rev.* **2006**, *106*, 1259–1281.

(76) Hofmeister, F. *Pathol. Pharmakol.* **1888**, *24*, 247–260.

(77) Otten, D. E.; Shaffer, P. R.; Geissler, P. L.; Saykally, R. J. *Proc. Natl. Acad. Sci. USA* **2012**, *109*, 701–705.

(78) Stern, A. C.; Baer, M. D.; Mundy, C. J.; Tobias, D. J. *J. Chem. Phys.* **2013**, *138*, 114709.

(79) Vaikuntanathan, S.; Geissler, P. L. *Phys. Rev. Lett.* **2014**, *112*, 020603.

(80) Cruz, C.; Ciach, A.; Lomba, E.; Kondrat, S. *J. Phys. Chem. C* **2018**, *123*, 1596–1601.

(81) Hubbard, J. *Phys. Rev. Lett.* **1959**, *3*, 77.

(82) Stratonovich, R. In *Soviet Physics Doklady*, 1957; Vol. 2, p 416.

(83) Frydel, D. *Eur. J. Phys.* **2015**, *36*, 065050.

(84) Cuvillier, N.; Bonnier, M.; Rondelez, F., et al. *Trends in Colloid and Interface Science XI* **1997**, 118–125.

(85) Li, B.; Liu, P.; Xu, Z.; Zhou, S. *Nonlinearity* **2013**, *26*, 2899.

(86) Frydel, D.; Levin, Y. *J. Chem. Phys.* **2013**, *138*, 174901, DOI: 10.1063/1.4802994.

(87) Adar, R. M.; Safran, S. A.; Diamant, H.; Andelman, D. *Phys. Rev. E* **2019**, *100*, 042615, DOI: 10.1103/PhysRevE.100.042615.

(88) Borukhov, I.; Andelman, D.; Orland, H. *Phys. Rev. Lett.* **1997**, *79*, 435.

(89) Borukhov, I.; Andelman, D.; Orland, H. *Electrochim. Acta* **2000**, *46*, 221–229.

(90) Bruch, D.; Balzer, C.; Wang, Z.-G. *J. Chem. Phys.* **2022**, *156*.

(91) Kornyshev, A. A. *J. Phys. Chem. B* **2007**, *111*, 5545–5557.

(92) Eigen, M.; Wicke, E. *J. Phys. Chem.* **1954**, *58*, 702–714.

(93) Kornyshev, A. A.; Vorotyntsev, M. A. *Electrochim. Acta* **1981**, *26*, 303–323.

(94) Nanjundiah, C.; McDevitt, S.; Koch, V. *J. Electrochem. Soc.* **1997**, *144*, 3392.

(95) Lockett, V.; Sedev, R.; Ralston, J.; Horne, M.; Rodopoulos, T. *J. Phys. Chem. C* **2008**, *112*, 7486–7495.

(96) Fedorov, M. V.; Kornyshev, A. A. *J. Phys. Chem. B* **2008**, *112*, 11868–11872.

(97) Qing, L.; Zhao, S.; Wang, Z.-G. *J. Phys. Chem. B* **2021**, *125*, 625–636.

(98) Zwanikken, J. W.; Olvera De La Cruz, M. *Proc. Natl. Acad. Sci. U.S.A.* **2013**, *110*, 5301–5308, DOI: 10.1073/pnas.1302406110.

(99) Markovich, T.; Andelman, D.; Podgornik, R. *Europhys. Lett.* **2016**, *113*, 26004.

(100) Besley, E. *Acc. Chem. Res.* **2023**, *56*, 2267–2277.

(101) Ma, M.; Gan, Z.; Xu, Z. *Phys. Rev. Lett.* **2017**, *118*, 076102.

Chapter 5

THE GAUSSIAN-CORE SELF ENERGY

Excluded volume interactions in field theories are often incorporated through an incompressibility condition which lacks packing effects. A typical revision to incompressibility is the introduction of a hard-core radius for the mass of a particles; however, this model overestimates the packing in soft-interacting bulky particles such as ionic liquids. The Gaussian-core model can be used to capture these soft interactions by introducing a smeared mass for each particle. Here, we develop a variational theory for fluctuations in electrolytes with Gaussian-core interactions using a renormalized-Gaussian approach. We derive analytical expressions for electrostatic and Gaussian-core self energies of particles as well as the bulk pressure.

5.1 Introduction

In theoretical modeling of electrolyte solutions, one must constrain the density of species to prevent nonphysical accumulation of ions at surfaces. For field theories, this is commonly achieved through an incompressibility constraint which enforces the local total density to be constant at every point in space. Although incompressibility assigns a volume to each species, there is no length scale associated with this volume. Consequently, finite size effects such as packing are lost. While incompressibility provides a reasonable description for dilute, simple ions, it is inaccurate for concentrated electrolytes where the excluded-volume effects dominate. These excluded-volume effects can be captured by introducing a length scale for ions either by a charge spread [1] or a hard-sphere radius [2], which produce oscillations in ion density profiles due to packing effects.

While a hard-sphere radius captures excluded-volume effects from mass for many fluids, it overestimates the packing effects in bulky species such as ionic liquids. Bulky particles are better described using a soft-core model, and the model we will focus on is the Gaussian-core model. The Gaussian-core model assumes the particles to have a smeared-Gaussian mass. We note that theoretical models for Gaussian-core fluids have been previously studied [3, 4]. However, we are interested in applying this model to charged systems as well as studying fluctuations in the Gaussian-core model using a non-perturbative approach.

In this chapter, we study fluctuations for an electrolyte solution of Gaussian-core ions and solvent using a field-theoretic renormalized-Gaussian fluctuating (RGF) theory, similar to the treatment for fluctuations in electrolyte solutions in Ref. [5]. We also treat the electrostatics using RGF theory with a smeared-Gaussian spread of charge. The key quantity we derive is the Gaussian-core self energy of a particle, which incorporates fluctuation effects through the particle self interaction as well as coupling to the local environment. We proceed by deriving the exact partition function using field-theoretic methods, followed by introducing the Gaussian renormalization with a Gaussian reference action for both the electrostatic and Gaussian-core interactions with the Gibbs–Feynmann–Bogoliubov bound. With the renormalized partition function, we apply variational principles to obtain a set of self-consistent equations, notably the Green's functions for the electrostatic and Gaussian-core parts, and expressions for their corresponding self energies. Then, we obtain analytical expressions for the self energies and pressure in the bulk without point approximations.

5.2 Theory

We develop our theory using field-theoretic approaches and variational principles, starting with the Hamiltonian for a simple electrolyte solution with both electrostatic and Gaussian-core interactions. Our goal is to obtain the grand canonical partition function, from which we can renormalize with the Gaussian reference action and apply variational principles to obtain a set of self-consistent equations.

Partition Function

Consider a solution of n_+ cations, n_- anions, and n_s solvent molecules contained in a volume V. The cations and anions have valency z_+ and z_-, respectively. The ions have a smeared-Gaussian charge

$$h_\pm(\mathbf{r}) = \left(\frac{1}{2a_\pm^2}\right)^{3/2} \exp\left(-\frac{\pi}{2a_\pm^2}\mathbf{r}^2\right) \tag{5.1}$$

where $a_\pm$ are the cation and anion radii. All species have a smeared-Gaussian mass

$$h_m(\mathbf{r}) = \left(\frac{3}{2\pi\sigma^2}\right)^{3/2} \exp\left(-\frac{3}{2\sigma^2}\mathbf{r}^2\right) \tag{5.2}$$

where σ is the soft-core radius, and we have assumed all species to have the same soft-core radius for simplicity. The Hamiltonian H is composed of both electrostatic and Gaussian-core interactions

$$\beta H = \beta U_{\text{ele}} + \beta U_{\text{ex}} \tag{5.3}$$

where the electrostatic interaction is simply the total Coulomb interactions

$$\beta U_{\text{ele}} = \frac{\beta e^2}{2} \int \mathrm{d}\mathbf{r} \int \mathrm{d}\mathbf{r}'\, \hat{\rho}_e(\mathbf{r}) C(\mathbf{r},\mathbf{r}') \hat{\rho}_e(\mathbf{r}') \tag{5.4}$$

where β is the inverse thermal energy $\beta = 1/kT$, e is elementary charge, and $C(\mathbf{r},\mathbf{r}')$ is the Coulomb kernel given by $-\nabla\cdot[\varepsilon\nabla C(\mathbf{r},\mathbf{r}')] = \delta(\mathbf{r}-\mathbf{r}')$. $\hat{\rho}_e(\mathbf{r})$ is the microscopic charge density

$$e\hat{\rho}_e(\mathbf{r}) = e\rho_{\text{ex}}(\mathbf{r}) + z_+ e \int \mathrm{d}\mathbf{r}'\, \hat{c}_+(\mathbf{r}') h_+(\mathbf{r}-\mathbf{r}') - z_- e \int \mathrm{d}\mathbf{r}'\, \hat{c}_-(\mathbf{r}') h_-(\mathbf{r}-\mathbf{r}') \tag{5.5}$$

where ρ_{ex} is a general fixed charge distribution, $\hat{c}_\pm(\mathbf{r}) = \sum_{i=1}^{n_\pm} \delta(\mathbf{r} - \mathbf{r}_i^\pm)$ are the microscopic ion densities, and charge units have been explicitly factored out. The Gaussian-core interaction is given by

$$\beta U_{\text{ex}} = \frac{\beta A}{2} \int \mathrm{d}\mathbf{r} \int \mathrm{d}\mathbf{r}' \, \hat{\rho}(\mathbf{r}) \delta(\mathbf{r} - \mathbf{r}') \hat{\rho}(\mathbf{r}') \tag{5.6}$$

where A is the excluded volume strength parameter, assumed to be the same for all species for simplicity, and $\hat{\rho}(\mathbf{r})$ is the microscopic solution density

$$\hat{\rho}(\mathbf{r}) = \int \mathrm{d}\mathbf{r}' \, h_m(\mathbf{r} - \mathbf{r}') [\hat{c}_+(\mathbf{r}') + \hat{c}_-(\mathbf{r}') + \hat{c}_s(\mathbf{r}')] \tag{5.7}$$

with $\hat{c}_s(\mathbf{r}) = \sum_{i=1}^{n_s} \delta(\mathbf{r} - \mathbf{r}_i^s)$. Thus, the grand canonical partition function is given by

$$\Xi = \sum_{i=1}^{n_+} \sum_{j=1}^{n_-} \sum_{k=1}^{n_s} Q(n_+, n_-, n_s) \exp\left[\beta\mu_+ n_+ + \beta\mu_- n_- + \beta\mu_s n_s\right] \tag{5.8a}$$

$$Q = \frac{1}{n_+! n_-! n_s! \nu_+^{n_+} \nu_-^{n_-} \nu_s^{n_s}} \int_V \prod_{i=1}^{n_+} \mathrm{d}\mathbf{r}_i^+ \int_V \prod_{j=1}^{n_-} \mathrm{d}\mathbf{r}_j^- \int_V \prod_{k=1}^{n_s} \mathrm{d}\mathbf{r}_k^s \exp\left[-\beta H\right] \tag{5.8b}$$

where ν_γ is the characteristic volume of species γ. We note that some authors use the thermal wavelength cubed as the volume scale. The choice of volume scale is inconsequential—it merely results in a concentration-independent shift in the chemical potential [6]. Next, we use the Hubbard–Stratonovich (HS) transformation to decouple the quadratic interactions of the electrostatic and Gaussian-core terms in Eqs. (5.4) and (5.6) at the expense of new couplings to the field variables ξ and w. We also define $\phi = \beta e \xi$ and $\epsilon = \varepsilon / \beta e^2$, and redefine $w = \beta w$ Upon using the HS transformation and applying the definitions of microscopic density operators, we arrive at the fully-simplified grand canonical partition function

$$\Xi = \frac{1}{Z_{\text{D}} Z_{\text{C}}} \int \mathscr{D}w \int \mathscr{D}\phi \, \exp\left\{-L[w(\mathbf{r}), \phi(\mathbf{r})]\right\} \tag{5.9a}$$

$$L = \int \mathrm{d}\mathbf{r} \left[\frac{1}{2\beta A} w^2 + \frac{\epsilon(\mathbf{r})}{2} (\nabla\phi)^2 + i\rho_{\text{ex}}\phi - \lambda_+ q_+ - \lambda_- q_- - \lambda_s q_s \right] \tag{5.9b}$$

$$q_\pm = \frac{1}{\nu_\pm} \int \mathrm{d}\mathbf{r} \exp\left[i\widehat{w h_m}(\mathbf{r}) \mp i z_\pm \widehat{h_\pm \phi}(\mathbf{r}) \right] \tag{5.9c}$$

$$q_s = \frac{1}{\nu_s}\int \mathrm{d}\mathbf{r}\exp\left[i\widehat{wh_m}(\mathbf{r})\right] \tag{5.9d}$$

$$\widehat{wh_m}(\mathbf{r}) = \int \mathrm{d}\mathbf{r}'\, w(\mathbf{r}')h_m(\mathbf{r}-\mathbf{r}') \tag{5.9e}$$

$$\widehat{\phi h_\pm}(\mathbf{r}) = \int \mathrm{d}\mathbf{r}'\, \phi(\mathbf{r}')h_\pm(\mathbf{r}-\mathbf{r}'). \tag{5.9f}$$

Gaussian Renormalization

We introduce the RGF theory by applying the Gibbs–Feynman–Bogoliubov inequality using a Gaussian reference action L_{ref}. Applying the Gibbs–Feynman–Bogoliubov inequality to Eq. (5.9a)

$$\Xi = \Xi_{\mathrm{ref}}\langle\exp\{-L[w,\phi]+L_{\mathrm{ref}}[w,\phi]\}\rangle_{\mathrm{ref}} \geq \Xi_{\mathrm{ref}}\exp\{-\langle L[w,\phi]-L_{\mathrm{ref}}[w,\phi]\rangle_{\mathrm{ref}}\} \tag{5.10}$$

the partition function is approximated by the right-hand side of Eq. (5.10), with reference action

$$\begin{aligned} L_{\mathrm{ref}} = \frac{1}{2}\int \mathrm{d}\mathbf{r}\int \mathrm{d}\mathbf{r}'\,[w(\mathbf{r})+iy(\mathbf{r})]\,G_m^{-1}(\mathbf{r},\mathbf{r}')\,[w(\mathbf{r}')+iy(\mathbf{r}')] \\ +\frac{1}{2}\int \mathrm{d}\mathbf{r}\int \mathrm{d}\mathbf{r}'\,[\phi(\mathbf{r})+i\psi(\mathbf{r})]\,G^{-1}(\mathbf{r},\mathbf{r}')\,[\phi(\mathbf{r}')+i\psi(\mathbf{r}')] \end{aligned} \tag{5.11}$$

where y and ψ are the average excluded volume and electrostatic field, respectively, and G_m^{-1} and G^{-1} are the excluded volume and electrostatic inverse Green's functions, respectively, taken to be variational parameters in the theory. Their functional inverse is defined as

$$\int \mathrm{d}\mathbf{r}'\, G(\mathbf{r},\mathbf{r}')G^{-1}(\mathbf{r}',\mathbf{r}'') = \delta(\mathbf{r}-\mathbf{r}''). \tag{5.12}$$

The reference partition function Ξ_{ref} is given by

$$\Xi_{\mathrm{ref}} = \frac{1}{Z_{\mathrm{D}}Z_{\mathrm{C}}}\int \mathscr{D}w\int \mathscr{D}\phi\,\exp\left[-L_{\mathrm{ref}}\right] = \left[\frac{\det(G_m)}{\det(D)}\right]^{1/2}\left[\frac{\det(G)}{\det(C)}\right]^{1/2} \tag{5.13}$$

where D is the delta function Kernel for the Gaussian-core interaction $D(\mathbf{r}-\mathbf{r}') = \beta A\delta(\mathbf{r}-\mathbf{r}')$. Note that the average $\langle\ldots\rangle$ is taken in the reference ensemble with action L_{ref}. We now seek to minimize the grand free energy given by

$$\beta W = -\log \Xi_{\text{ref}} + \langle L[w,\phi] - L_{\text{ref}}[w,\phi]\rangle_{\text{ref}} \tag{5.14}$$

which first requires evaluating the averages in the action and reference action. Evaluating these averages is rather lengthy and involved. We will make a few notes here, but we defer the reader to Ref. [5] for more detailed evaluation. The averages are taken with respect to the reference ensemble, where the average of some quantity is given by

$$\langle F[w,\phi]\rangle = \int \mathscr{D}w \int \mathscr{D}\phi\, F[w,\phi]P[w,\phi] \tag{5.15}$$

where $P[w,\phi] = Z_{\text{C}}Z_{\text{D}}\Xi_{\text{ref}}\exp(-L_{\text{ref}})$ so that $\int \mathscr{D}w \int \mathscr{D}\phi\, P[w,\phi] = 1$, and we have omitted the subscript *ref* from the angled brackets for notational clarity. Note that since the fields w and ϕ are independent, their probabilities will factorize. We define the variables $\chi = \phi + i\psi$ and $\chi_m = w + iy$, and note that since the distributions of χ and χ_m are Gaussian, their averages can be evaluated exactly using Gaussian functional integral identities. It follows that $\langle\chi\rangle = \langle\chi_m\rangle = 0$, $\langle\chi(\mathbf{r})\chi(\mathbf{r}')\rangle = G(\mathbf{r},\mathbf{r}')$, and $\langle\chi_m(\mathbf{r})\chi_m(\mathbf{r}')\rangle = G_m(\mathbf{r},\mathbf{r}')$. Additionally, the following averages will appear and they evaluate to

$$\int \mathrm{d}\mathbf{r} \int \mathrm{d}\mathbf{r}'\, \delta(\mathbf{r}-\mathbf{r}')\epsilon(\mathbf{r})\langle[\nabla_{\mathbf{r}}\chi(\mathbf{r})\cdot\nabla_{\mathbf{r}'}\chi(\mathbf{r}')]^2\rangle = \int \mathrm{d}\mathbf{r} \int \mathrm{d}\mathbf{r}'\, \nabla_{\mathbf{r}}\cdot[\epsilon(\mathbf{r})\nabla_{\mathbf{r}'}\delta(\mathbf{r}-\mathbf{r}')]G(\mathbf{r},\mathbf{r}') \tag{5.16}$$

and

$$\langle e^{\mp i z_\pm \widehat{\chi h_\pm}(\mathbf{r})}\rangle = \exp\left[-\frac{1}{2}z_\pm^2 \int \mathrm{d}\mathbf{r}' \int \mathrm{d}\mathbf{r}''\, h_\pm(\mathbf{r}-\mathbf{r}')G(\mathbf{r}',\mathbf{r}'')h_\pm(\mathbf{r}''-\mathbf{r})\right] \tag{5.17}$$

and similar identities for χ_m. Applying these definitions and identities to Eq. (5.14), we arrive at the full variational grand free energy

$$\beta W = -\frac{1}{2}\log\left(\frac{\det G_m}{\det D}\right) - \frac{1}{2}\log\left(\frac{\det G}{\det C}\right) + \int \mathrm{d}\mathbf{r}\,\left[-\frac{1}{2\beta A}y^2 - \frac{\epsilon(\mathbf{r})}{2}(\nabla\psi)^2 + \rho_{\mathrm{ex}}\psi\right]$$
$$- \int \mathrm{d}\mathbf{r}\,\left[\frac{\lambda_+}{\nu_+}e^{\widehat{yh_m}(\mathbf{r}) - z_+\widehat{h_+\psi}(\mathbf{r}) - u_+ - u_m} + \frac{\lambda_-}{\nu_-}e^{\widehat{yh_m}(\mathbf{r}) + z_-\widehat{h_-\psi}(\mathbf{r}) - u_- - u_m} + \frac{\lambda_s}{\nu_s}e^{\widehat{yh_m}(\mathbf{r}) - u_m}\right]$$
$$- \frac{1}{2}\int \mathrm{d}\mathbf{r}\int \mathrm{d}\mathbf{r}' G_m(\mathbf{r},\mathbf{r}')\left[G_m^{-1}(\mathbf{r},\mathbf{r}') - \frac{1}{\beta A}\delta(\mathbf{r}-\mathbf{r}')\right]$$
$$- \frac{1}{2}\int \mathrm{d}\mathbf{r}\int \mathrm{d}\mathbf{r}' G(\mathbf{r},\mathbf{r}')\left[G^{-1}(\mathbf{r},\mathbf{r}') - C^{-1}(\mathbf{r},\mathbf{r}')\right] \quad (5.18)$$

where $u_\pm$ and u_m are the ion's electrostatic and Gaussian-core self energies given by

$$u_\pm(\mathbf{r}) = \frac{1}{2}z_\pm^2\int \mathrm{d}\mathbf{r}'\int \mathrm{d}\mathbf{r}''\, h_\pm(\mathbf{r}-\mathbf{r}')G(\mathbf{r}',\mathbf{r}'')h_\pm(\mathbf{r}''-\mathbf{r}) \quad (5.19a)$$

$$u_m(\mathbf{r}) = \frac{1}{2}\int \mathrm{d}\mathbf{r}'\int \mathrm{d}\mathbf{r}''\, h_m(\mathbf{r}-\mathbf{r}')G_m(\mathbf{r}',\mathbf{r}'')h_m(\mathbf{r}''-\mathbf{r}). \quad (5.19b)$$

Applying the variational condition in ψ, y, G, and G_m yields a set of self-consistent equations

$$y(\mathbf{r}) = -\beta A\int \mathrm{d}\mathbf{r}'\, h_m(\mathbf{r}-\mathbf{r}')\left[c_s(\mathbf{r}') + c_+(\mathbf{r}') + c_-(\mathbf{r}')\right] \quad (5.20a)$$

$$-\nabla\cdot\left[\epsilon\nabla\psi(\mathbf{r})\right] = \rho_{\mathrm{ex}} + \int \mathrm{d}\mathbf{r}'\,\left[z_+h_+(\mathbf{r}-\mathbf{r}')c_+(\mathbf{r}') - z_-h_-(\mathbf{r}-\mathbf{r}')c_-(\mathbf{r}')\right] \quad (5.20b)$$

$$\frac{1}{\beta A}G_m(\mathbf{r},\mathbf{r}') + \int \mathrm{d}\mathbf{r}_1\int \mathrm{d}\mathbf{r}_2\, h_m(\mathbf{r}-\mathbf{r}_1)h_m(\mathbf{r}_1-\mathbf{r}_2)G_m(\mathbf{r}_2,\mathbf{r}')\left[c_s(\mathbf{r}_1) + c_+(\mathbf{r}_1) + c_-(\mathbf{r}_1)\right]$$
$$= \delta(\mathbf{r}-\mathbf{r}') \quad (5.20c)$$

$$\int \mathrm{d}\mathbf{r}_1\int \mathrm{d}\mathbf{r}_2\, G(\mathbf{r}_2,\mathbf{r}')\left[z_+^2h_+(\mathbf{r}-\mathbf{r}_1)h_+(\mathbf{r}_1-\mathbf{r}_2)c_+(\mathbf{r}_1) - z_-^2h_-(\mathbf{r}-\mathbf{r}_1)h_-(\mathbf{r}_1-\mathbf{r}_2)c_-(\mathbf{r}_1)\right]$$
$$-\nabla_{\mathbf{r}}\cdot\left[\epsilon(\mathbf{r})\nabla_{\mathbf{r}}G(\mathbf{r},\mathbf{r}')\right] = \delta(\mathbf{r}-\mathbf{r}') \quad (5.20d)$$

where $c_\pm$ and c_s are the ion and solvent concentrations, obtained from the integrand of chemical potential derivatives of the grand free energy

$$c_\pm = \frac{\lambda_\pm}{\nu_\pm}\exp\left[\widehat{yh_m}(\mathbf{r}) \mp z_\pm\widehat{h_\pm\psi}(\mathbf{r}) - u_\pm - u_m\right] \quad (5.21a)$$

$$c_s = \frac{\lambda_s}{\nu_s} \exp\left[\widehat{y h_m}(\mathbf{r}) - u_m\right]. \tag{5.21b}$$

Eqs. (5.20a)–(5.20d) are the key results of this chapter. Eq. (5.20a) and (5.20b) are simply the mean-field conditions in the fields y and ψ. Eq. (5.20a) enforces a penalty on high densities in solution–a consequence of the repulsive Gaussian-core excluded-volume interaction. Eq. (5.20b) is simply the Poisson equation, albeit non local due to the Gaussian smearing of charge. Eqs. (5.20c) and (5.20d) represent Gaussian fluctuations around the saddle-point for the excluded volume interaction and electrostatic potential through the Green's function. Note that these equations are non local due to the convolutions since no point limits were taken. Invoking the point-limit amounts to replacing all smearing functions h with a delta function, and Eqs. (5.20b) and (5.20d) would simply to those derived in Ref. [5]. The point limits for these equations are nondivergent; however, we must retain their general form as we are interested the length scales associated with the ion size and mass spread.

With the equations above, one can simplify the variational grand free energy in Eq. (5.18)

$$\begin{aligned}\beta W = &-\frac{1}{2}\log\left(\frac{\det G_m}{\det D}\right) - \frac{1}{2}\log\left(\frac{\det G}{\det C}\right) - \int \mathrm{d}\mathbf{r}\left[c_+ + c_- + c_s + \frac{y^2}{2\beta A}\right] \\ &+ \frac{1}{2}\int \mathrm{d}\mathbf{r}\,\psi\left[\rho_{\mathrm{ex}} - z_+c_+ + z_-c_-\right] - \frac{1}{2}\int \mathrm{d}\mathbf{r}\int \mathrm{d}\mathbf{r}' G_m(\mathbf{r},\mathbf{r}')\bar{\rho}(\mathbf{r},\mathbf{r}') \\ &- \int \mathrm{d}\mathbf{r}\int \mathrm{d}\mathbf{r}' G(\mathbf{r},\mathbf{r}')\bar{I}(\mathbf{r},\mathbf{r}')\end{aligned} \tag{5.22}$$

where

$$\bar{\rho}(\mathbf{r},\mathbf{r}') = \int \mathrm{d}\mathbf{r}_1\, h_m(\mathbf{r}-\mathbf{r}_1)h_m(\mathbf{r}_1-\mathbf{r}')\left[c_s(\mathbf{r}_1) + c_+(\mathbf{r}_1) + c_-(\mathbf{r}_1)\right] \tag{5.23a}$$

$$\bar{I}(\mathbf{r},\mathbf{r}') = \frac{1}{2}\int \mathrm{d}\mathbf{r}_1\,\left[z_+^2 h_+(\mathbf{r}-\mathbf{r}_1)h_+(\mathbf{r}_1-\mathbf{r}')c_+(\mathbf{r}_1) - z_-^2 h_-(\mathbf{r}-\mathbf{r}_1)h_-(\mathbf{r}_1-\mathbf{r}')c_-(\mathbf{r}_1)\right]. \tag{5.23b}$$

5.3 Bulk Analysis

Here, we analyze the self-consistent Eqs. (5.20a)–(5.20d) and the free energy in Eq. (5.22) in a bulk solution with a uniform dielectric constant. Specifically, we derive analytical expressions for the Gaussian-core and electrostatic self energies without taking a point-limit, as well as an expression for the bulk pressure.

Bulk Self Energy

In the bulk, all species have a constant density and there is no fixed charge ρ_{ex}. Charge neutrality requires that the bulk ion concentrations are $c_{\pm,\text{B}} = z_{\mp} c_{\text{B}}$, where c_{B} is the bulk salt concentration. Moreover, Eq. (5.20b) is automatically satisfied by charge neutrality, giving a constant electrostatic potential that is absorbed into the fugacity for all species. Eq. (5.20a) gives an expression for the bulk excluded volume field $y_{\text{B}} = -\beta A \rho_{\text{B}}$, where $\rho_{\text{B}} = c_{s,\text{B}} + (z_+ + z_-)c_{\text{B}}$ is the total bulk density.

For the correlation expressions in Eqs. (5.20c) and (5.20d), the concentration dependencies become constant and factor out of the integral, leaving double convolutions over the Green's functions. The resulting expressions for the bulk Green's functions can be solved analytically using Fourier transforms and invoking the convolution theorem for the integral terms. Solving for the Green's functions in Fourier space and taking the inverse Fourier transforms gives the following expressions

$$G_m(\mathbf{r}-\mathbf{r}') = \int \mathrm{d}\mathbf{k}\, \frac{\beta A}{1+\beta A \rho_{\text{B}} \widehat{h_m}^2(\mathbf{k})} e^{2\pi i(\mathbf{r}-\mathbf{r}')\cdot\mathbf{k}} \tag{5.24a}$$

$$G(\mathbf{r}-\mathbf{r}') = \int \mathrm{d}\mathbf{k}\, \frac{1}{4\pi^2\epsilon\mathbf{k}^2 + z_+ z_- c_{\text{B}} \left[z_+ \widehat{h_+}^2(\mathbf{k}) + z_- \widehat{h_-}^2(\mathbf{k}) \right]} e^{2\pi i(\mathbf{r}-\mathbf{r}')\cdot\mathbf{k}}. \tag{5.24b}$$

Here, we define the forward and reverse Fourier transforms as $\mathcal{F}[f(\mathbf{r})] = \int \mathrm{d}\mathbf{r}\, f(\mathbf{r}) e^{-2\pi i \mathbf{r}\cdot\mathbf{k}}$ and $\mathcal{F}^{-1}[\hat{f}(\mathbf{k})] = \int \mathrm{d}\mathbf{k}\, \hat{f}(\mathbf{k}) e^{2\pi i \mathbf{r}\cdot\mathbf{k}}$, respectively. Additionally, $\widehat{h_m}^2(\mathbf{k})$ and $\widehat{h_\pm}^2(\mathbf{k})$ are the Fourier transforms of the smearing functions squared. Eqs. (5.24a) and (5.24b) can be further simplified by converting the integrals to spherical coordinates by noting that the integrand depends only on the magnitude of the wave vector and by taking $(\mathbf{r}-\mathbf{r}')\cdot\mathbf{k} = |\mathbf{r}-\mathbf{r}'||\mathbf{k}|\cos\theta$ to give

$$G_m(|\mathbf{r}-\mathbf{r}'|) = \frac{2}{|\mathbf{r}-\mathbf{r}'|} \int_0^\infty \mathrm{d}k\, k \frac{\beta A}{1+\beta A \rho_{\text{B}} \widehat{h_m}^2(k)} \sin(2\pi|\mathbf{r}-\mathbf{r}'|k) \tag{5.25a}$$

$$G(|\mathbf{r}-\mathbf{r}'|) = \frac{2}{\epsilon|\mathbf{r}-\mathbf{r}'|} \int_0^\infty \mathrm{d}k\, k \frac{1}{4\pi^2 k^2 + \kappa^2(k)} \sin(2\pi|\mathbf{r}-\mathbf{r}'|k) \tag{5.25b}$$

where $\kappa^2(k) = \frac{z_+ z_- c_{\text{B}}}{\epsilon} \left[z_+ \widehat{h_+}^2(k) + z_- \widehat{h_-}^2(k) \right]$ is the wave-vector-dependent screening function. Eqs. (5.25a) and (5.25b) are convergent integrals but they cannot be integrated analytically to obtain closed form expressions for G_m and G. However,

we can directly substitute these expressions for the Green's functions into the expressions for the self energies, given by Eqs. (5.19b) and (5.19a). Doing this for the Gaussian-core self energy yields

$$u_m = -\frac{1}{2\rho_{\mathrm{B}}}\left(\frac{3}{4\pi\sigma^2}\right)^{3/2}\mathrm{Li}_{3/2}(-\beta A\rho_{\mathrm{B}}) \tag{5.26}$$

where $\mathrm{Li}_{3/2}(-\beta A\rho_{\mathrm{B}})$ is special function called a polylogarithm of $3/2$ order.

One can also derive a "point-limit" expression to the self-energy where a point limit is taken in the Gaussian-core Green's function expression Eq. (5.20c) by replacing the smearing functions with delta functions. Solving for G_m in this limit yields $G_m(|\mathbf{r}-\mathbf{r}'|) = \beta A\delta(\mathbf{r}-\mathbf{r}')/(1+\beta A\rho_{\mathrm{B}})$. Substituting this expression into the self-energy gives

$$u_m^{\mathrm{pl}} = -\frac{\beta A}{2(1+\beta A\rho_{\mathrm{B}})}\left(\frac{3}{4\pi\sigma^2}\right)^{3/2} \tag{5.27}$$

where the superscript "pl" denotes "point-limit." Note that the point-limit cannot be taken in the self-energy expression, as this returns a divergent same-point Green's function. We can study the limits of the Gaussian-core self energy in βA at fixed ρ_{B}

$$\lim_{\beta A\to 0} u_m = \frac{\beta A}{2}\left(\frac{3}{4\pi\sigma^2}\right)^{3/2} \tag{5.28a}$$

$$\lim_{\beta A\to 0} u_m^{\mathrm{pl}} = \frac{\beta A}{2}\left(\frac{3}{4\pi\sigma^2}\right)^{3/2} \tag{5.28b}$$

$$\lim_{\beta A\to \infty} u_m = \frac{1}{2\rho_{\mathrm{B}}}\left(\frac{3}{4\pi\sigma^2}\right)^{3/2}\frac{[\log(\beta A\rho_{\mathrm{B}})]^{3/2}}{\Gamma(5/2)} \tag{5.28c}$$

$$\lim_{\beta A\to \infty} u_m^{\mathrm{pl}} = \frac{1}{2\rho_{\mathrm{B}}}\left(\frac{3}{4\pi\sigma^2}\right)^{3/2} \tag{5.28d}$$

where $\Gamma(x)$ denotes the gamma function. We see for both point-limit and exact, the Gaussian-core self energy is always positive as expected for a purely repulsive interaction. At low βA, the excluded volume field is weak and both point-limit and exact return the same self energy, meaning the particle structure is unimportant in this limit. For high βA, the point limit and exact differ by a logarithmic factor with dimensionless quantity $\beta A\rho_{\mathrm{B}}$. Thus, the logarithmic factor originates from the

Gaussian structure of the particles, making the self energy more repulsive for strong fields relative to unstructured particles.

For the electrostatic self energy, substituting the electrostatic Green's function (Eq. (5.25b)) into the electrostatic self energy gives

$$u_{\pm} = \frac{2\pi z_{\pm}^2}{\epsilon} \int_0^{\infty} \mathrm{d}k\, k^2 \frac{\widehat{h_{\pm}}^2(k)}{4\pi^2 k^2 + \kappa^2(k)}. \tag{5.29}$$

This integral cannot be evaluated analytically. However, as we are mostly interested in obtaining corrections to the ions' electrostatic self energy due to ion structure, we can expand the screening function $\kappa(k)$ for small wavelengths. This approximation is reasonable, for the exponential factor $\widehat{h_{\pm}}^2(k)$ in the numerator suppresses large wavelength contributions. Noting that $\widehat{h_{\pm}}^2(k) = \exp\left(-4\pi a_{\pm}^2 k^2\right) \approx 1 - 4\pi a_{\pm}^2 k^2 + \mathcal{O}(k a_{\pm})^4$, expanding the screening function for small k gives

$$u_{\pm} = \frac{2\pi z_{\pm}^2}{\epsilon} \int_0^{\infty} \mathrm{d}k\, k^2 \frac{\widehat{h_{\pm}}^2(k)}{4\pi^2 k^2 (1 - c_{\mathrm{B}} l_{\mathrm{B}} \bar{a}^2) + \kappa^2} \tag{5.30}$$

where l_{B} is the Bjerrum length $l_{\mathrm{B}} = 1/4\pi\epsilon$ and $\bar{a}^2 = 4 z_+ z_- (z_+ a_+^2 + z_- a_-^2)$. This expression for the self energy can be integrated analytically, which in the limit of the electrostatic screening length being much larger than the ionic radii $\kappa a_{\pm} \ll 1$ yields

$$u_{\pm} = \frac{z_{\pm}^2 l_{\mathrm{B}}}{2} \left[\frac{1}{a_{\pm}\left(1 - c_{\mathrm{B}} l_{\mathrm{B}} \bar{a}^2\right)} - \frac{\kappa}{\left(1 - c_{\mathrm{B}} l_{\mathrm{B}} \bar{a}^2\right)^{3/2}} \right] + \mathcal{O}(\kappa^2). \tag{5.31}$$

Note that Eq. (5.31) returns the expression derived in Ref. [5] for sufficiently small ionic radii ($\bar{a} \to 0$). The first term of the self energy is the Born solvation energy and the second term is a universal part due to interactions with other ions. The terms in parentheses in the denominators represent small corrections for ion size.

Bulk Pressure

Here, we evaluate the grand free energy (Eq. (5.22) in the bulk without taking point-limit approximations. In the bulk, the third term in Eq. (5.22) simplifies accordingly from the bulk y field derived earlier, $y_{\mathrm{B}} = -\beta A \rho_{\mathrm{B}}$. The fourth term vanishes by electroneutrality. The final two terms are evaluated using the Fourier transform methods outlined in the previous section. The first two terms can be

evaluated by using the functional integral definition for the determinant of a kernel and substituting the Fourier-space kernel of into the determinant definition. The Fourier-space kernel becomes diagonalized, which returns the determinant as a product of the eigenvalues. Noting the explanations above, the bulk free energy becomes

$$\begin{aligned}\frac{\beta W_{\mathrm{B}}}{V} &= -\rho_{\mathrm{B}}(1+\beta A\rho_{\mathrm{B}}) \\ &\quad + 2\pi\int_0^\infty \mathrm{d}k\, k^2\left\{\log\left[1+\beta A\rho_{\mathrm{B}}\widehat{h_m}^2(k)\right] - \frac{\beta A\rho_{\mathrm{B}}\widehat{h_m}^2(k)}{1+\beta A\rho_{\mathrm{B}}\widehat{h_m}^2(k)}\right\} \\ &\quad + 2\pi\int_0^\infty \mathrm{d}k\, k^2\left\{\log\left[1+\frac{\kappa^2(k)}{4\pi^2\, k^2}\right] - \frac{\kappa^2(k)}{4\pi^2 k^2+\kappa^2(k)}\right\} \end{aligned} \tag{5.32}$$

where the first term comes from the bulk osmotic pressure and the mean-field Gaussian-core contribution, the second term is the Gaussian-core correlation, and the last term is the electrostatic correlation. The bulk pressure is then obtained simply from the Euler relationship of the grand free energy to the pressure $-\beta W/V = P$. The Gaussian-core contribution to the bulk pressure is able to be analytically evaluated by performing integration by parts on the logarithmic term. The Gaussian-core contribution is thus given by

$$P_{\mathrm{gc}} = \beta A\rho_{\mathrm{B}}^2 - \frac{1}{2}\left(\frac{3}{4\pi\sigma^2}\right)^{3/2}\left[\mathrm{Li}_{3/2}(-\beta A\rho_{\mathrm{B}}) - \mathrm{Li}_{5/2}(-\beta A\rho_{\mathrm{B}})\right] \tag{5.33}$$

with limiting behavior

$$\lim_{\beta A\rho_{\mathrm{B}}\to 0} P_{\mathrm{gc}} = \beta A\rho_{\mathrm{B}}^2 - \left(\frac{3}{4\pi\sigma^2}\right)^{3/2}\frac{(\beta A\rho_{\mathrm{B}})^2}{8\sqrt{2}} + \mathcal{O}(\beta A\rho_{\mathrm{B}})^3 \tag{5.34a}$$

$$\lim_{\beta A\rho_{\mathrm{B}}\to\infty} P_{\mathrm{gc}} = \beta A\rho_{\mathrm{B}}^2 - \left(\frac{\sqrt{3}}{4\pi^2\sigma^3}\right)\left[\log(\beta A\rho_{\mathrm{B}})\right]^{3/2}\left[1-\frac{2}{5}\log(\beta A\rho_{\mathrm{B}})\right]. \tag{5.34b}$$

Note that $\beta A\rho_{\mathrm{B}} \to 0$ is the ideal gas limit, and the Gaussian-core portion of the bulk pressure returns only quadratic corrections to ideal gas, proving thermodynamic consistency. Additionally, all correlation terms have a σ^{-3} prefactor, meaning the point limit ($\sigma \to 0$) of the correlation terms is divergent as expected from any self-interacting system. Lastly, the high-density/strong-interacting limit ($\beta A\rho_{\mathrm{B}} \to \infty$)

gives only a small logarithmic correction to the quadratic mean-field contribution, since the correlations effectively cancel, similar to excluded volume interactions in a polymer melt.

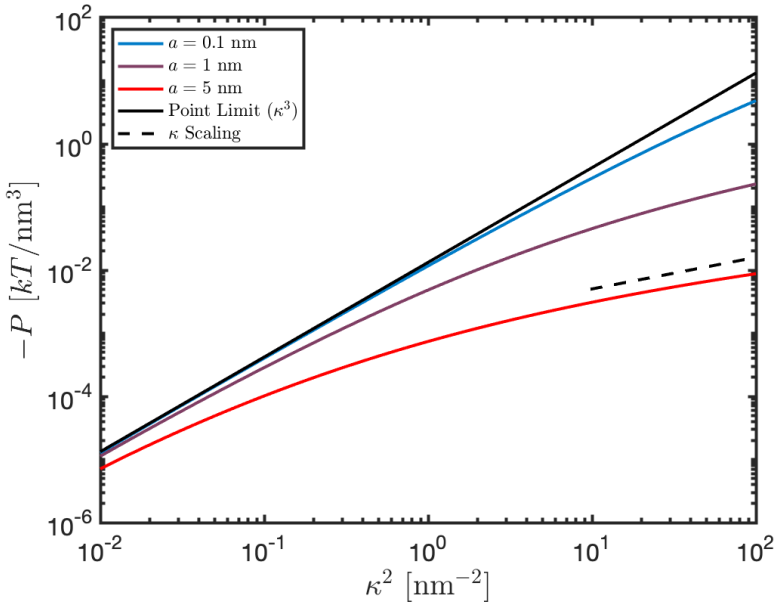

Figure 5.1: Negative of the electrostatic correlation contribution to the pressure as a function of κ^2 for various ionic radii, evaluated from Eq. (5.36). The ions are symmetric ($a_+ = a_-$) and have Gaussian smearing of charge. The solid black line is the point limit result. The dashed black line shows κ scaling for reference.

For the electrostatic correlation contribution to the pressure, the point limit result is

$$P_{\text{ele}} = -2\pi \int_0^\infty \mathrm{d}k\, k^2 \left\{ \log\left[1 + \frac{\kappa^2(k)}{4\pi^2\, k^2}\right] - \frac{\kappa^2(k)}{4\pi^2 k^2 + \kappa^2(k)} \right\} = \frac{\kappa^3}{24\pi}. \tag{5.35}$$

However, the full electrostatic contribution with ion structure in the last term of Eq. (5.32) cannot be integrated analytically, even for symmetric ionic radii ($a_+ = a_-$). We evaluate the pressure contribution numerically for various symmetric ionic radii as a function of κ^2 using a cutoff of 100 for the integral upper bound. For symmetric ionic radii, the integral expression becomes

$$P_{\text{ele}} = -2\pi \int_0^\infty \mathrm{d}k\, k^2 \left\{ \log\left[1 + \frac{\kappa^2 \hat{h}^2(k)}{4\pi^2\, k^2}\right] - \frac{\kappa^2 \hat{h}^2(k)}{4\pi^2 k^2 + \kappa^2 \hat{h}^2(k)} \right\} \tag{5.36}$$

where $\hat{h}^2(k) = \exp\left(-4\pi a^2 k^2\right)$ is the Fourier transform of the Gaussian smearing function squared. Using a cutoff for the upper bound is a reasonable approximation so long as the cutoff is much larger than the ionic radii, as high frequency contributions decay exponentially due to the Gaussian ion structure.

The negative of the bulk electrostatic correlation contribution to the pressure is shown in Fig. 5.1 as a function of the inverse Debye screening length squared κ^2. We see that for sufficiently small ionic radii, the pressure scaling almost coincides with the point limit result since ion structure effects are small. This effect is amplified for weak screening (small κ^2) as electrostatic effects dominate. However, for large ionic radii > 1 nm, there is significant deviation from the point limit result, especially at high screening (large κ^2). Physically, this deviation comes from the size effects of the ions dominating when electrostatics is sufficiently screened, which mathematically originates from the high frequency contributions to the integral in Eq. (5.36) decaying exponentially from the ion structure. Such large ion sizes are representative the delocalization of charge on bulky ions in ionic liquid systems, albeit their charge spread will not be Gaussian. In the limit of large ion size, the pressure appears to scale slightly weaker than κ, suggesting the pressure scales with ion concentration more weakly than $c_{\pm}^{1/2}$.

5.4 Summary/Conclusion

In this chapter, we developed a variational theory for fluctuations in electrolytes with Gaussian-core interactions using a renormalized-Gaussian approach for both excluded-volume and electrostatic interactions. Using Gaussian smearing functions for the charge and mass spread, we derived analytical expressions for the electrostatic and Gaussian-core self energies of particles as well as the bulk pressure without taking point limits. We found that in the high-density limit, excluded-volume fluctuation effects give a logarithmic correction to the bulk pressure in the high-density/strongly-interacting limit. Moreover, accounting for the charge spread of an ion, the electrostatic portion of the bulk pressure transitions from κ^3 to sub K scaling as the ionic radius increases, which is relevant for bulky ions such as ionic liquids.

For inhomogeneous cases, such as ions near a surface, we believe this theory will be useful because it captures packing effects of the ions/solvent, which gives more qualitatively accurate density profiles like in molecular dynamics simulations. Moreover, the theory would be able to capture underscreening behavior to some

degree for highly-concentrated bulky electrolytes [2]. One can also derive an integral equation theory for a Gaussian-core fluid without ions by taking the point limit of Eq. (5.20c) and substituting into the density, which may provide improvements over existing integral equations theories for soft-body excluded volume interactions. These tasks are reserved for future work.

References

(1) Frydel, D.; Levin, Y. *J. Chem. Phys.* **2013**, *138*, 174901, DOI: 10.1063/1.4802994.

(2) Adar, R. M.; Safran, S. A.; Diamant, H.; Andelman, D. *Phys. Rev. E* **2019**, *100*, 042615, DOI: 10.1103/PhysRevE.100.042615.

(3) Berne, B. J.; Pechukas, P. *J. Chem. Phys.* **1972**, *56*, 4213–4216, DOI: 10.1063/1.1677837.

(4) Stillinger, F. H. *J. Chem. Phys.* **1976**, *65*, 3968–3974, DOI: 10.1063/1.432891.

(5) Wang, Z.-G. *Phys. Rev. E* **2010**, *81*, 021501.

(6) Jin, Z.; Wu, J. *J. Phys. Chem. B* **2011**, *115*, 1450–1460, DOI: 10.1021/jp110066z.